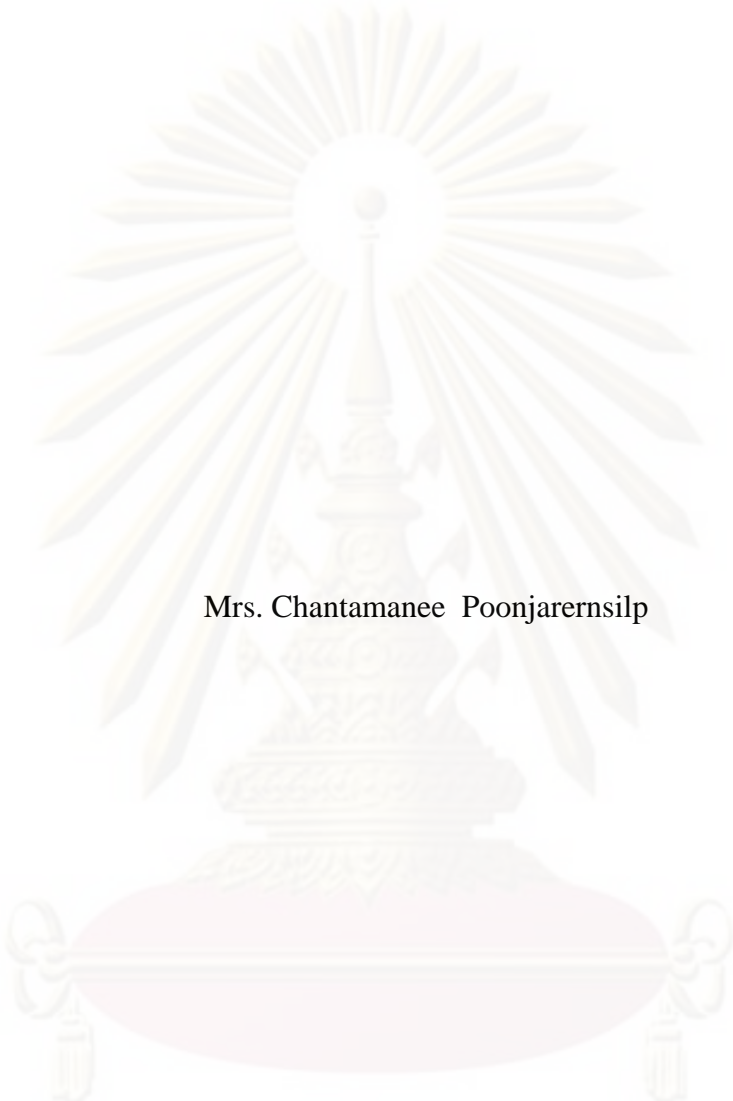


SYNTHESIS OF CARBON NANOHORNS HYBRIDIZED WITH PALLADIUM
NANOPARTICLES BY GAS-INJECTED ARC DISCHARGE TECHNIQUE



Mrs. Chantamane Poonjarernsilp

A Dissertation Submitted in Partial Fulfillment of the Requirements
for the Degree of Doctor of Engineering Program in Chemical Engineering

Department of Chemical Engineering

Faculty of Engineering

Chulalongkorn University

Academic year 2009

Copyright of Chulalongkorn University

Thesis Title SYNTHESIS OF CARBON NANOHORNS HYBRIDIZED WITH PALLADIUM NANOPARTICLES BY GAS-INJECTED ARC DISCHARGE TECHNIQUE

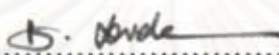
By Mrs. Chantamane Poonjarensilp

Field of Study Chemical Engineering

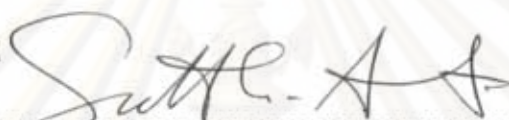
Thesis Advisor Associate Professor Tawatchai Charinpanitkul, D.Eng.

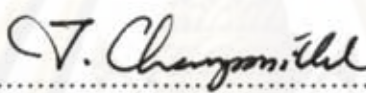
Thesis Co-Advisor Associate Professor Noriaki Sano, Ph.D.

Accepted by the Faculty of Engineering, Chulalongkorn University in Partial Fulfillment of the Requirements for the Doctoral Degree

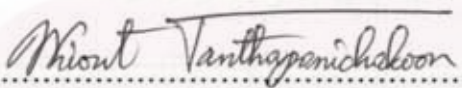

..... Dean of the Faculty of Engineering
(Associate Professor Boonsom Lerdhirunwong, Dr.Ing.)

THESIS COMMITTEE

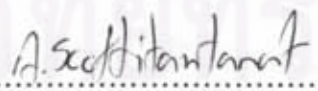

..... Chairman
(Professor Suttichai Assabumrungrat, Ph.D.)

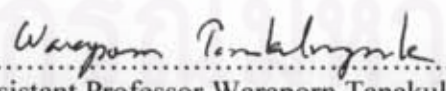

..... Thesis Advisor
(Associate Professor Tawatchai Charinpanitkul, D.Eng.)


..... Thesis Co-Advisor
(Associate Professor Noriaki Sano, Ph.D.)


..... Examiner
(Professor Wiwut Tanthapanichakoon, Ph.D.)


..... Examiner
(Assistant Professor Varong Pavarajan, Ph.D.)


..... Examiner
(Apinan Soottitantawat, D.Eng.)


..... External Examiner
(Assistant Professor Waraporn Tanakulrungsank, D.Eng.)

ฉันทมนี พูลเจริญศิลป์ : การสังเคราะห์คาร์บอนนาโนฮอร์นไฮบริดกับอนุภาค
แพลเลเดียมในระดับนาโนเมตรด้วยเทคนิคการอาร์คในน้ำที่มีการพ่นก๊าซ. (SYNTHESIS OF
CARBON NANOHORNS HYBRIDIZED WITH PALLADIUM NANOPARTICLES
BY GAS-INJECTED ARC DISCHARGE TECHNIQUE) อ. ที่ปรึกษาวิทยานิพนธ์หลัก
: รองศาสตราจารย์ ดร. ชัชชัย ชรินพานิชกุล, อ. ที่ปรึกษาวิทยานิพนธ์ร่วม : Associate
Professor Noriaki Sano, Ph.D., 127 หน้า

งานวิจัยนี้มุ่งเน้นศึกษาวิธีการสังเคราะห์คาร์บอนนาโนฮอร์นไฮบริดกับแพลเลเดียมใน
ระดับนาโนเมตรในชั้นคอนเดนิวด้วยวิธีการอาร์คในน้ำที่มีการพ่นก๊าซ เพื่อให้บรรลุตาม
วัตถุประสงค์ได้ศึกษาปฏิกิริยาภายในระบบการอาร์คในน้ำที่มีการพ่นก๊าซอย่างละเอียด อีกทั้งได้
ศึกษาอิทธิพลของอุณหภูมิที่มีผลต่อการสังเคราะห์คาร์บอนนาโนฮอร์น จากการทดลองพบว่า
ปริมาณของคาร์บอนนาโนฮอร์นที่สังเคราะห์ได้มีปริมาณลดลงเมื่ออุณหภูมิของน้ำสูงขึ้น แต่
ความบริสุทธิ์ของคาร์บอนนาโนฮอร์นไม่เปลี่ยนแปลง นอกจากนี้ได้เสนอโมเดลทางคณิตศาสตร์
เพื่ออธิบายปรากฏการณ์ที่เกิดขึ้นโดยพิจารณาจากปริมาณไอคาร์บอนที่สูงงูเสีย จากการเกิด
คาร์บอนนาโนฮอร์น และจากการแพร่ของไอน้ำภายในขั้วแคโทด ซึ่งแบ่งเป็นสามส่วนคือ ส่วน
อาร์คพลาสมา ส่วนที่เกิดการเย็นตัวอย่างรวดเร็วของไอ และส่วนควาน์สตริม ปริมาณของ
คาร์บอนนาโนฮอร์นที่ลดลงเกิดจากปฏิกิริยาข้างเคียงของการเกิดก๊าซไฮโดรเจนจากไอคาร์บอน
กับไอน้ำ อนึ่งจากการวัดคลื่นแสงของส่วนอาร์คพลาสมาสามารถยืนยันได้ว่าปฏิกิริยาการเกิดก๊าซ
ไฮโดรเจนไม่ได้เกิดที่ส่วนอาร์คพลาสมาเนื่องจากการพ่นก๊าซใน โดรเจนช่วยไล่ไอน้ำออกจาก
ส่วนอาร์คพลาสมา จากการวิเคราะห์โดยใช้โมเดลทางคณิตศาสตร์ที่เสนอสามารถอธิบาย
ความสัมพันธ์ของปริมาณการเกิดก๊าซไฮโดรเจนและอุณหภูมิได้อย่างแม่นยำ จากการ
วิเคราะห์เชิงปริมาณพบว่าอนุภาคแพลเลเดียมที่ถูกห่อหุ้มอยู่ภายในกลุ่มคาร์บอนนาโนฮอร์นมี
ขนาด 3 ถึง 6 นาโนเมตรเมื่อใช้ลวดแพลเลเดียมขนาด 0.1 และ 0.3 มิลลิเมตร แต่เมื่อใช้ลวดขนาด
0.5 และ 0.8 มิลลิเมตร อนุภาคแพลเลเดียมมีแนวโน้มที่มีขนาดใหญ่ขึ้น และมีบางส่วนที่ขึ้น
ออกมาจากกลุ่มคาร์บอนนาโนฮอร์น นอกจากนี้พบว่าพื้นที่ผิวส่วนใหญ่ของสารประกอบดังกล่าว
เป็นพื้นที่ของคาร์บอนนาโนฮอร์น และปริมาณของอนุภาคแพลเลเดียมในสารประกอบจะเพิ่มขึ้น
เมื่อใช้ลวดขนาดใหญ่ขึ้น

ภาควิชา.....วิศวกรรมเคมี.....
สาขาวิชา.....วิศวกรรมเคมี.....
ปีการศึกษา.....2552.....

ลายมือชื่อนิสิต.....*Chontamane*.....
ลายมือชื่ออ.ที่ปรึกษาวิทยานิพนธ์หลัก.....*[Signature]*.....
ลายมือชื่ออ.ที่ปรึกษาวิทยานิพนธ์ร่วม.....*Noriaki Sano*.....

4971806121 : MAJOR CHEMICAL ENGINEERING
 KEYWORDS : SINGLE WALLED CARBON NANOHORNS/ PALLADIUM
 NANOPARTICLES/ ARC DISCHARGE/ NANOSTRUCTURE/ MODEL

CHANTAMANEE POONJARERNSILP : SYNTHESIS OF CARBON
 NANOHORNS HYBRIDIZED WITH PALLADIUM NANOPARTICLES
 BY GAS-INJECTED ARC DISCHARGE TECHNIQUE. THESIS
 ADVISOR : ASSOC. PROF. TAWATCHAI CHARINPANITKUL, D.Eng.,
 THESIS CO-ADVISOR : ASSOC. PROF. NORIAKI SANO, Ph.D., 127 pp.

The objective of this research is to develop a method for synthesizing single-walled carbon nanohorns (SWCNHs) hybridized with palladium nanoparticles (Pd) in a single step by using gas-injected arc-in-water method (GI-AIW). A deep insight into GI-AIW reaction system has been examined. An influence of water temperature on synthesis of SWCNHs has been experimentally studied. It is revealed that the yield of SWCNHs significantly decreases with the increase in water temperature although the purity of SWCNHs is independent on the temperature change. A mathematical model of relevant reactions in GI-AIW system was proposed by accounting the emission of carbon vapor, formation of SWCNHs and diffusion of water vapor in three zones inside cathode hole, which are arc plasma zone, quenching zone and downstream zone. A side reaction between H_2O and C produces H_2 gas and consumes a certain amount of carbon vapor, resulting in the hindered SWCNH formation. Moreover the observation of the optical spectra emitted from the arc plasma zone strongly supports an expected mechanism that the H_2 generating reaction does not occur in the arc plasma zone since N_2 flow can purge H_2O out. The model proposed in this study can precisely explain the correlation between H_2 gas production and water temperature. By using the GI-AIW method, SWCNHs/Pd nanocomposite can be synthesized by using Pd wire inserted inside anode hole as a precursor. Pd nanoparticles with spherical shape are embedded inside SWCNHs aggregates. The diameter of Pd nanoparticles is in the range of 3-6 nm when Pd wire diameters of 0.1 and 0.3 mm are employed. Meanwhile, the mean diameter and the size distribution of Pd nanoparticles tend to increase when Pd wire diameters of 0.5 and 0.8 mm are used. Additionally Pd nanoparticles tend to expose outside SWCNHs aggregates when larger diameter of Pd wire is employed. The total surface area of the composite dominantly depended on the surface area of SWCNHs. Based on thermogravimetric analysis, the amount of Pd nanoparticles in the composite increases with the increase in Pd wire diameter.

Department : Chemical Engineering..... Student's Signature Chantamanee
 Field of Study : Chemical Engineering..... Advisor's Signature V. Chupmittel
 Academic Year : 2009..... Co-Advisor's Signature Nishi Saw.

ACKNOWLEDGEMENTS

Firstly, I would like to express my heartfelt thanks to all those individuals whose wisdom, support, and encouragement made my journey possible. Special thanks extended to Associate Professor Dr. Tawatchai Charinpanitkul, my advisor and Associate Professor Dr. Noriaki Sano, my co-advisor, who guided me through hurdles, and provided constant support that made my journey completed lot easier than it would have been. They always give me on the job training, useful guidance, deep discussion from intriguing experimental results to an issue of surviving in the scientific world and kindness. I am also grateful to thank Professor Dr. Suttichai Assabumrungrat, as a chairman, Professor Dr. Wiwut Tanthapanichakoon, Assistant Professor Dr. Waraporn Tanakulrungsank, Assistant Professor Dr. Varong Pavarajan, and Dr. Apinan Soottitantawat, as the members of thesis committee.

Next, I would like to gratefully thank Professor Hajime Tamon, Department of Chemical Engineering, Kyoto University for his valuable suggestions, allowing me to do the experiment, using the valuable accessories and kindness during my ten months research in Japan. My deepest gratitude also goes to Mrs. Mayumi Uchimura, Mr. Hiroki Mori and Mr. Yoshihiro Akita who have not only kindly supported to the remarkable success achieved in this work but also my wonderful friends.

Many thanks for kind suggestions and useful help to Dr. Kanokwan Ngaosuwan, Miss Siriporn Monchayapisut, Miss Pusanisa Patharachotesawate, Miss Pamornrat Chantam, Mr. Thongchai Glinrun, and many friends in the Center of Excellence in Particle Technology (CEPT) from Chulalongkorn University who always provided the encouragement and co-operate along the thesis study.

Most of all, I would like to express my greatest gratitude to my grandmother and my family who always gave me suggestions, support and encouragement.

This research was supported by grant from under the program Strategic Scholarships for Frontier Research Network for the Joint Ph.D. Program Thai Doctoral degree from the Office of the Higher Education Commission Thailand, Japan Society for the Promotion of Science (JSPS) Grant-in-Aid for Exploratory Research (Contract No. 19656024) and Scientific Research B (Contract No. 21360394), and the Centennial Fund of CU.

CONTENTS

	Page
ABSTRACT (IN THAI)	iv
ABSTRACT (IN ENGLISH)	v
ACKNOWLEDGEMENTS	vi
CONTENTS	vii
LIST OF FIGURES	xi
NOMENCLATURE	xv
 CHAPTER	
I INTRODUCTION	1
1.1 Background.....	1
1.2 Research objectives.....	3
1.3 Research scope.....	3
1.4 Importance of research.....	4
II THEORY AND LITERATURE REVIEW	5
2.1 Carbon nanoparticles.....	5
2.2 Arc discharge technique.....	8
2.2.1 Electric arc.....	8
2.2.2 Production of carbon nanotubes by arc discharge technique..	10
2.2.3 Properties of arc plasma.....	11
2.3 Background of arc-in-water with gas injection for SWCNHs synthesis.....	13
2.3.1 Synthesis of carbon ‘onions’ in water.....	13
2.3.2 Formation mechanism of nanoparticles under arc discharge in water: vapor phase growth.....	13
2.3.3 Synthesis of SWCNT with nanohorns by ‘arc in liquid’ nitrogen.....	16
2.3.4 Synthesis of SWCNHs using the gas-injected arc in water method (GI-AIW).....	17
2.4 Continued literature review on arc discharge model.....	18
2.4.1 Liquid phase growth.....	19

CHAPTER	Page
2.4.2 Solid phase growth.....	19
2.4.3 The crystallization model.....	20
2.5 Carbon nanotube-metal composite.....	21
2.5.1 Preparation by hot-pressing process.....	21
2.5.2 Preparation of metal-catalyst nanoparticles supported by growth of carbon nanotubes.....	23
2.5.2.1 Impregnate with solution of metal catalyst.....	23
2.5.2.2 Thin film deposition.....	25
2.5.2.3 Thick metal catalyst film coating.....	27
2.5.2.4 Colloidal method.....	27
2.5.2.5 So-gel technique.....	28
2.5.2.6 Unsupported/floating catalyst method.....	28
2.5.3 Literature review on preparation of carbon nanoparticles together with metal nano-particles by using arc discharge technique.....	31
2.5.3.1 Arc-discharge in solution method.....	31
2.5.3.2 Arc-discharge between graphitic carbon rod and metal rod in liquid nitrogen.....	33
III EXPERIMENTAL PROCEDURE.....	36
3.1 Synthesis of SWCNHs: Influence of water temperature.....	36
3.1.1 Electrodes.....	36
3.1.2 Experimental method.....	37
3.1.3 Characterization of SWCNHs.....	38
3.1.3.1 The weight of the floating SWCNHs.....	38
3.1.3.2 A transmission electron microscope.....	38
3.1.3.3 Raman spectroscopy.....	39
3.1.4 Characterization of gas emerging from arc zone.....	40
3.1.5 Characterization of optical spectra emitted from arc plasma zone.....	41
3.2 Influence of Pd wire diameter on synthesis of SWCNHs/Pd nanocomposite.....	42

CHAPTER	Page
3.2.1	Materials and procedures..... 42
3.2.2	Characterization of SWCNHs/Pd nanocomposite..... 44
3.2.2.1	Production yield of SWCNHs/Pd..... 44
3.2.2.2	Transmission electron microscopic analysis..... 43
3.2.2.3	X-ray diffractometric analysis..... 44
3.2.2.4	Raman spectroscopic analysis..... 45
3.2.2.5	BET specific surface area analysis..... 45
3.2.2.6	Analysis of Exposed surface area of Pd nanoparticles..... 45
3.2.2.7	Thermogravimetric and differential thermal analysis (TG-DTA)..... 46
IV	RESULTS AND DISCUSSION..... 48
4.1	Influence of water temperature on synthesis of SWCNHs by GI- AIW method..... 48
4.1.1	Influence of water temperature on characteristics of SWCNHs..... 48
4.1.1.1	Transmission electron microscopic analysis..... 48
4.1.1.2	Raman spectroscopic analysis..... 49
4.1.2	Influence of water temperature on production yield of SWCNHs and by-product gases..... 50
4.1.2.1	Yield and production rate of SWCNHs..... 50
4.1.2.2	Production of by-product gases analyzed by gas chromatography analysis..... 52
4.1.2.3	Selectivity of SWCNHs production..... 53
4.2	Development of mathematical model of phenomena in GI-AIW method..... 54
4.2.1	Analysis of optical spectra from arc plasma zone..... 54
4.2.1.1	Phenomena obtained form optical spectra..... 54
4.2.1.2	Conceptual illustration of reaction field in GI-AIW..... 56

CHAPTER	Page
4.2.1.3	Determination of arc plasma temperature by optical spectra analysis..... 57
4.2.2	Model of water vapor diffusion and hydrogen production.. 58
4.2.2.1	Mathematic model of heat transfer..... 59
4.2.2.2	Mathematic model of mass transfer..... 60
4.2.2.3	Phenomena of water vapor diffusion and hydrogen production..... 62
4.2.3	Possible mechanism of SWCNHs formation..... 66
4.3	One-step synthesis of SWCNHs/Pd nanocomposite by GI-AIW method: Influence of Pd wire diameter..... 66
4.3.1	Characterization of SWCNHs/Pd nanocomposite..... 66
4.3.1.1	Transmission electron microscopic analysis..... 66
4.3.1.2	Pd nanoparticles size distribution..... 67
4.3.1.3	X-ray diffraction analysis..... 69
4.3.1.4	Raman spectroscopic analysis..... 70
4.3.1.5	Thermogravimetric analysis..... 72
4.3.2	Yield of SWCNHs and Pd nanoparticles..... 75
4.3.3	Surface area of SWCNHs/Pd nanocomposite..... 77
4.3.3.1	BET specific surface area..... 77
4.3.3.2	Pd nanoparticles exposed surface area..... 78
V	CONCLUSIONS AND RECOMMENDATIONS..... 82
5.1	Conclusions..... 82
5.2	Recommendations..... 83
REFERENCES.....	84
APPENDICES.....	90
APPENDIX A : EXPERIMENTAL DATA FOR SWCNHs SYNTHESIS...	90
APPENDIX B : EXPERIMENTAL DATA FOR SWCNHs/Pd SYNTHESIS	108
APPENDIX C : CALCULATION FOR ARC TEMPERATURE.....	118
APPENDIX D : LIST OF PUBLICATIONS.....	125
VITAE.....	127

LIST OF FIGURES

FIGURE		PAGE
2.1	Structures image of carbon nanoparticles (a) molecular structure of Buckminsterfullerene C ₆₀ , (b) TEM image of carbon nanotubes, (c) TEM images of multishelled nanoparticle, (d) TEM image of single walled carbon nanohorns and (e) TEM image of carbon nano-onion.....	6
2.2	(a) Schematic of an arc discharge chamber (b) A characteristic electric arc, arc current 200A in nitrogen at atmospheric pressure.....	9
2.3	Diagram from article that proposed formation mechanism of onions in a water arc. (a) Relative electric field strength, shown by arrows, between a rod anode (17 V) and a flat cathode (ground) in a gas bubble surrounded by water. (b) Direction of thermal expansion from the plasma to the gas-water interface. (c) Qualitative ion density distribution. (d) Temperature gradient obtained from Eq. (2.2) assuming q_c , Q_R , and $dT/dt = 0$. The formation of elongated nanoparticles in zone I and onions in zone II is also shown schematically.....	14
2.4	Image from articles that showed schematic of reaction system.....	18
2.5	Diagram form article that showed schematic illustration of the solid phase growth model for multiwalled carbon nanotube (MWCNT). (a) Electron bombardment from cathode causes heating of the anode surface, and evaporation of C ₂ and other species. These rapidly coalesce into fullerene soot fragments. (b) Some of the fullerene soot condenses onto the cathode, with the remainder being deposited on the walls of the vessel. (c), (d) and (e) enlarged views of the interior of the cathodic deposit, showing transformation of the fullerene soot into firstly open-ended “seed” structures and then MWCNT and nanoparticles.....	20
2.6	Diagram form article that showed schematic formation of Pd-nano particles-filled CNT during arc-discharge in solution process.....	33

FIGURE	PAGE	
2.7	Typical TEM image from article that showed carbon nanocapsules containing Fe core. The nanocapsules existing in cathode deposit was obtained from arc discharge using carbon-iron electrodes with arc current of 100A in liquid nitrogen.....	34
2.8	Typical TEM image from article that showed (a) MWCNT/ cuprite (Cu ₂ O) composite and (b) MSCNC/cuprite (Cu ₂ O) composite.....	35
3.1	Dimension of cathode and anode which was employed in the synthesis SWCNHs by GI-AIW method.....	36
3.2	Experimental set-up for synthesis SWCNHs by Gas-Injected Arc-in-Water (GI-AIW) method.....	37
3.3	Transmission electron microscope (TEM; JEOL, JEM-1010).....	39
3.4	Green light Raman spectroscopy (Raman Systems, R-3000).....	40
3.5	Gas chromatograph (Shimadzu, GC-14B) with TCD detector.....	41
3.6	Schematic illustration of recording the spectra from arc plasma zone by using fiber optical spectrometer (Ocean Optics, USB2000).	42
3.7	Dimension of electrodes and the structure of apparatus for synthesizing SWCNHs/Pd nanocomposite.....	43
3.8	X-ray diffractometer (XRD; RINT2100).....	45
3.9	Analytical apparatus for N ₂ adsorption (BEL Japan, Belsorp mini) which was used for determining BET specific surface area.....	45
3.10	Analytical apparatus for CO chemisorptions (BEL Japan, BEL-CAT) which was used for determining exposed Pd surface area.....	46
3.11	Thermogravimetric analyzer (TGA-50, Shimadzu).....	47
4.1	Typical TEM images of SWCNHs produced by GI-AIW. (a) Low magnification image. (b) High magnification image.....	48
4.2	A Raman spectrum of as-grown SWCNHs which were synthesized with the water temperature 2°C.....	49
4.3	Influence of water temperature on G/D ratio in Raman spectra from as-grown SWCNHs synthesized by GI-AIW with varied water temperature.....	50

FIGURE	PAGE	
4.4	Influence of water temperature on (a) the yield of SWCNHs, (b) the production rate of SWCNHs.....	51
4.5	A typical GC curve from byproduct gases when synthesized SWCNHs at the water temperature 79°C.....	52
4.6	Influence of water temperature on the production rate of H ₂ gas.....	53
4.7	Influence of water temperature on the selectivity of SWCNHs formation (ψ).....	54
4.8	Optical spectra from arc plasma in conventional arc-in-water (AIW) and GI-AIW: (1) GI-AIW at water temperature 2°C, (2) GI-AIW at water temperature 70°C, (3) AIW at water temperature 25°C.....	55
4.9	Schematic illustration of the reaction field in GI-AIW with three categorized zones and schematic image of the profiles of temperature and water vapor pressure in the reaction field in GI-AIW system.....	56
4.10	Normalized curve from Planck distribution law together with typical optical spectra used for estimating arc temperature.....	58
4.11	Relationship between H ₂ production rate and the water vapor pressure directly estimated from bulk water temperature.....	63
4.12	Influence of water temperature on (a) temperature at liquid-gas interface (T_i), (b) water vapor pressure at liquid-gas interface ($P_{H_2O, i}$) and water vapor pressure at the bulk water temperature ($P_{H_2O, w}$).....	63
4.13	Influence of water temperature on H ₂ production rate (r_{H_2}).....	64
4.14	TEM image of SWCNHs/Pd nanocomposites.....	67
4.15	TEM images of SWCNHs/Pd and their corresponding Pd nanoparticles size distribution histograms which were synthesized by inserting Pd wire of (a) 0.1 mm, (b) 0.3 mm, (c) 0.5 mm and (d) 0.8 mm in diameter inside anode hole.....	68

FIGURE	PAGE	
4.16	XRD pattern of SWCNHs/Pd which were synthesized by arc discharge (a) SWCNHs without Pd nanoparticle, (b) SWCNHs/Pd nanocomposite by inserting Pd wire diameter 0.1 mm, (c) 0.3 mm, (d) 0.5 mm and (e) 0.8 mm, respectively.....	70
4.17	The intensity ratio of G-band over D-band (G/D) in Raman spectra as a function of Pd wire diameter.....	71
4.18	Weight loss versus temperature of as-grown SWCNHs and SWCNHs/Pd with varied size of Pd wire in anode hole.....	72
4.19	Derivative weight loss versus temperature of as-grown SWCNHs and SWCNHs/Pd with varied size of Pd wire in anode hole.....	73
4.20	Weight of Pd in SWCNHs/Pd as a function of Pd wire diameter.....	75
4.21	Yield of SWCNHs and Pd nanoparticles as a function of Pd wire diameter.....	76
4.22	Typical TEM image of Pd nanoparticles in cathode deposit.....	77
4.23	BET specific surface area of SWCNHs/Pd and specific surface area of carbonaceous part as a function of Pd wire diameter.....	78
4.24	Pd nanoparticle exposed specific surface area as a function of Pd wire diameter.....	79
4.25	Percentage of exposed surface area of Pd nanoparticle outside SWCNHs aggregate as a function of Pd wire diameter.....	80

ศูนย์วิทยทรัพยากร

จุฬาลงกรณ์มหาวิทยาลัย

NOMENCLATURE

Chemicals

MSCNCs	Multi-shelled carbon nanocapsules
MWCNTs	Multi-walled carbon nanotubes
LN	Liquid nitrogen
Pd	Palladium
SWCNHs	Single walled carbon nanohorns
SWCNTs	Single walled carbon nanotubes

Method

GI-AIW	Gas-injected arc-in-water
--------	---------------------------

Analytical method

GC	Gas chromatography
TEM	Transmission electron microscope
TG-DTA	Thermogravimetric and differential thermal analysis
XPS	X-ray photoelectron spectroscopy
XRD	X-ray diffraction

Equation

		<i>Unit</i>
A	Area of inter-electrode space	m ²
C_p	Specific heat of the gas	J g ⁻¹ ·K ⁻¹
C_{vg}	Heat capacity of gas phase	J mol ⁻¹ K ⁻¹
C_{vw}	Heat capacity of liquid phase	J mol ⁻¹ K ⁻¹
c	Speed of light (= 2.998 × 10 ⁸ m s ⁻¹)	m s ⁻¹
\bar{D}_N	Mean diameter by number	nm
D_p	Particle diameter	nm
h	Planck's constant (= 6.626 × 10 ⁻³⁴ J·s)	J·s
h_g	Heat transfer coefficient of gas phase	J s ⁻¹ K ⁻¹
h_w	Heat transfer coefficient of liquid phase	J s ⁻¹ K ⁻¹
K_p	Mass transfer coefficient	mol m ⁻² s ⁻¹

	Equation	Unit
M_g	Mole density of gas phase	mol m^{-3}
M_w	Mole density of liquid phase	mol m^{-3}
N	Total particle number	
$N_{\text{H}_2\text{O}}$	H_2O mass transfer rate	mol bar s^{-1}
Δn	Number of particle	
P	Percentage of the exposed surface area of Pd particle in total Pd surface	%
$P_{\text{H}_2\text{O},i}$	H_2O partial pressure at liquid-gas interface	bar
$P_{\text{H}_2\text{O},0}$	H_2O partial pressure at the bottom of quenching zone	bar
Q_g	Heat flux of gas phase	$\text{J m}^{-2} \text{s}^{-1}$
Q_R	Reaction heat	$\text{J m}^{-2} \text{s}^{-1}$
Q_w	Heat flux of liquid phase	$\text{J m}^{-2} \text{s}^{-1}$
q_c	Heat transfer rate by convection	$\text{J m}^{-2} \text{s}^{-1} \text{K}^{-1}$
q_k	Heat transfer rate by thermal conductivity	$\text{J m}^{-2} \text{s}^{-1} \text{K}^{-1}$
R	Gas constant (= $8.31451 \text{ J mol}^{-1} \text{ K}^{-1}$)	$\text{J mol}^{-1} \text{ K}^{-1}$
r	Distance from the arc center	m
r_a	Average radius of Pd nanoparticle	m
r_{CNH}	SWCNHs production rate	mol bar s^{-1}
r_{H_2}	H_2 production rate	mol bar s^{-1}
S_T	The surface area of Pd particles per unit mass	$\text{m}^2 \text{g}^{-1}$
$Pd-S_{\text{expo}}$	Specific surface area of Pd nanoparticle which exposed outside SWCNHs matrix	$\text{m}^2 \text{g}^{-1}$
T	Temperature	K
T_{arc}	Temperature of arc plasma	K
T_i	Temperature of liquid-gas interface	K
T_w	Temperature of liquid phase	K
T_0	Temperature at the bottom of quenching zone	K
v_i	Velocity of gas or water at interface to axial direction	m s^{-1}
v_0	Velocity of gas or water at the bottom of quenching zone	m s^{-1}

	Greek letter	<i>Unit</i>
κ	Boltzman's constant ($= 5.67051 \times 10^{-8} \text{ W m}^{-2} \text{ K}^{-4}$)	$\text{W m}^{-2} \text{ K}^{-4}$
λ	Wave length	cm
λ_{max}	Wave length at a maximum radiation	cm
ρ	Density	g m^{-3}



ศูนย์วิทยทรัพยากร
จุฬาลงกรณ์มหาวิทยาลัย

CHAPTER I

INTRODUCTION

1.1 Background

Since the discovery of the C₆₀ fullerene molecule [1] and the carbon nanotubes (CNTs) [2], the interest in carbon nanomaterials has been grown rapidly and continually. CNTs are considered as new promising materials for a variety of potential applications. As a result of the intense research activity, new types of the carbon nanostructures, such as carbon onions [3] and carbon nanohorns [4, 5] have also been discovered. It should be noted that the carbon nanomaterials structure (fullerene, nanotube, onion, nanohorns, etc) could be synthesized from different harsh environments (electric arc, electron irradiation, plasma torch). Nevertheless, better understanding of possible formation mechanism of carbon nanomaterials would allow the development of their synthesis efficiency.

Among the new carbon nanostructures, single-wall carbon nanohorns (SWCNHs) are attracting much attention because of their large surface area and high gas-adsorption capacity which are ideal for catalyst support [6], gas storage, gas sensor [7, 8] and drug carrier [9]. SWCNHs have been synthesized by the CO₂ laser ablation method [4, 5], the 'arc in liquid' method [10, 11] and some other arc techniques [13, 14]. Currently it is recognized that initial investment for large scale production would be enormous, hence research into lower cost methods are currently undergoing and have been previously researched. The arc-in-water with gas injection

method (GI-AIW) [11, 12] is one of method which used low cost and convenience way for operation. Moreover metal catalyst is not required for their synthesis.

Sano et al. [12] have previously studied the influence of gas flow rate, arc current and gas component on the structure and yield of SWCNHs. It was found that using 80A DC current for generating arc discharge and N₂ gas flow rate of 5 L min⁻¹ is an optimum condition for fabricating SWCNHs. However, water temperature, which is a factor essentially important to optimize this reaction field, has not been well understood yet. It is important to clarify this issue because an increase in synthesis of SWCNHs would provide an impact on the commercial production. Additionally, the formulation of a theoretical model of GI-AIW is currently demanded because none of previous literature has provided a deep insight into this system. Under such circumstance, this research set its aim to reveal the influence of the water temperature on the production of SWCNHs.

Besides the production of pure SWCNHs, manipulation and handling of nano-sized composite materials is becoming important in many applications. For example, to synthesize carbon nanomaterials hybridized with metals [15-17] could provide possibility for an application of H₂ sensor [18], catalyst [19] and magnetism materials [20]. Currently nanotube and activated carbon are actively investigated as supporting materials for palladium nanoparticles [17, 21]. Methods for fabricating palladium carbon nanocomposite (Pd/C) reported in these literatures [17, 21] make use of a wet impregnation method in which ready-made carbon nanomaterials are mixed with Pd precursor in solution. Such method requires many steps of handling leading to an increase in overall production cost. Under such situation, there is a recent technique which can avoid such disadvantages by simultaneously decorating the nanotube with metallic nanoparticles during its synthesis by arc discharge in liquid phase [16].

However, detailed studies on the in situ decoration of metal nanoparticles onto carbon nanomaterials have not been attempted. Therefore, effect of water temperature on synthesis of SWCNHs by GI-AIW method with an incorporation of Pd wire in graphite electrode is employed for synthesizing Pd nanoparticles during synthesis of SWCNHs in a single step.

1.2 Research objectives

The objectives of this research are as follows:

1.2.1. To study the effect of water temperature on the production of single-walled carbon nanohorns (SWCNHs)

1.2.2. To propose an empirical model for explaining heat and mass transfer during an operation of gas-injected arc-in water (GI-AIW) method.

1.2.3. To prepare SWCNHs hybridized with Pd nanoparticles by one-step synthesis using GI-AIW method.

1.3 Research scope

Regarding to the research objectives, the scopes of research presented below are,

1.3.1. Using the arc-in-water with N₂ gas injection to synthesize SWCNHs by varying water temperature within the range of 0-80°C.

1.3.2. Study the influence of water temperature on the characteristics and the production of SWCNHs.

1.3.3. Prepare the empirical model for describing the effect of water temperature on SWCNHs production in GI-AIW method.

1.3.4. Using the arc-in-water with N_2 gas injection in order to synthesize Pd nanoparticles hybridized with SWCNHs by inserting Pd wire in anode hole with various Pd wire diameter of 0.1, 0.3, 0.5 and 0.8 mm. and study the influence of Pd wire diameter on the properties of SWCNHs/ Pd nanocomposite

1.3.5. Characterization of SWCNHs/Pd nanocomposite using X- ray diffraction (XRD), BET surface area (N_2 adsorption), total metal surface area (CO chemisorptions), thermogravimetric analysis (TGA), Raman spectroscopy and transmission electron microscopy (TEM).

1.4 Importance of research

The synthesis of SWCNHs by using GI-AIW method which is the simple and inexpensive method can be developed into larger scale. The study on the parameters which influence on the system will be the essential work in a continuous process. Therefore, this proposed research will provide the comprehensive data for SWCNHs and Pd nanoparticles forming reaction to gain more understanding for development in nanotechnology.

CHAPTER II

THEORY AND LITERATURE REVIEW

2.1 Carbon nanoparticles

It has been well recognized that carbon nanoparticles can be produced via an arc discharge method. These carbon nanoparticles include many structures, which are fullerene (C_{60}), carbon nanocapsules (CNCs), carbon nanohorns (CNHs), carbon nano-onions (or onion like fullerenes OLFs) and carbon nanotubes (CNTs) as shown in Fig. 2.1. The different carbon nanoparticles could be fabricated under different liquid environments. In previous research works, only carbon nanotubes, carbon nano-onions and carbon nanocapsules could be produced in water [22-24], where carbon nanohorns could only be produced by arcing under liquid nitrogen or arc-in-water with nitrogen gas injection [10, 11].

Discovered in 1985, a sketch of the buckminsterfullerene molecule is shown in Fig. 2.1 (a) [1]. It has 12 pentagonal (5 sided) and 20 hexagonal (6 sided) faces symmetrically arrayed to form a molecular ball. Interesting by, a soccer ball has the same geometric configuration as fullerene. These ball-like molecules bind with each other in the solid state to form a crystal lattice having a face centered cubic structure. In the lattice each C_{60} molecule is separated from its nearest neighbor by 1 nm (the distance between their centers is 1 nm), and they are held together by weak forces called van der Waals forces.

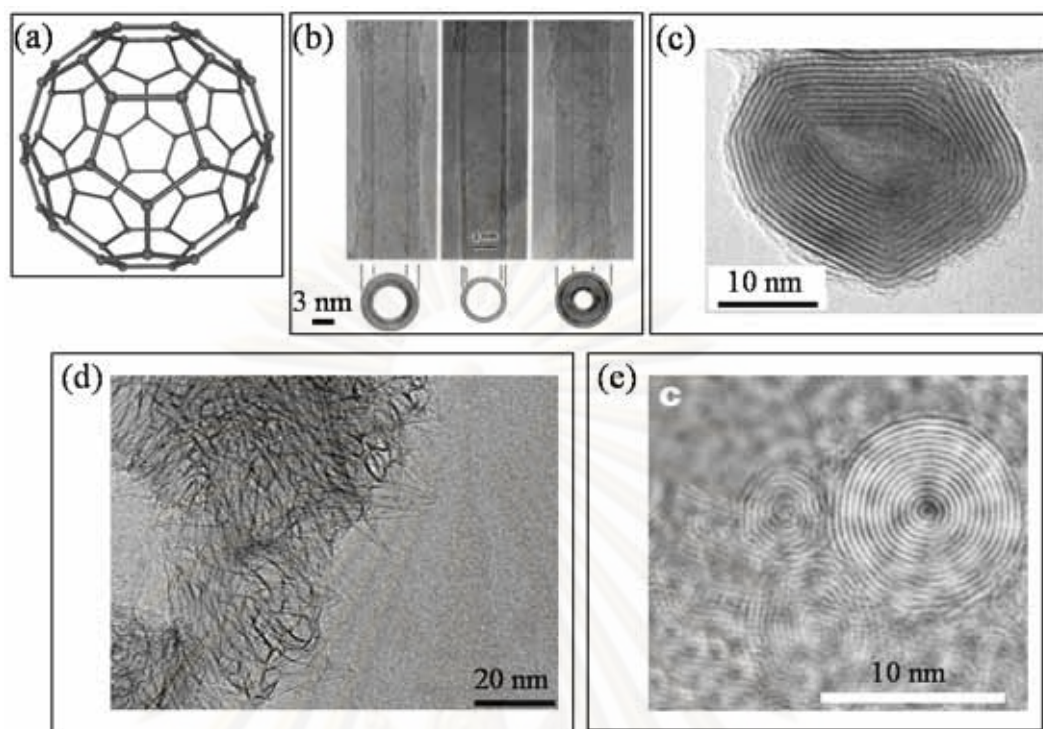


Figure 2.1 Structures image of carbon nanoparticles (a) molecular structure of Buckminsterfullerene C_{60} [1, 25], TEM images of (b) carbon nanotubes [2], (c) multishelled nanoparticle [26], (d) single walled carbon nanohorns and (e) carbon nano-onions [22].

Carbon nanotubes (CNTs) reported officially in 1991 [2] are different from typical carbonic graphite, with a lattice of hexagons that roll into a cylinder. The diameter of these CNTs could vary and the length is generally over a 100 times that of the diameter reaching up to $1\mu\text{m}$. In general, single walled or multi-walled carbon nanotubes are concentric cylinders of the “honeycomb” lattice structure inside of each other. The ends of the cylinders are round off with the help of pentagons to close off the tube with a rounded edge. Similarly if there are defects in the tubes it is due to the inclusion of a pentagon in the honeycomb lattice, resulting in a bend in the tube rather than the straight structure.

Carbon nanocapsules (CNCs) or multishelled carbon nanoparticles [27] are that exhibit various shapes, such as spherical, polyhedral or short tubes. The nanoparticles exhibit a wide variety of different shapes, although the outer shape seems to depend on the size of the inner cavity. Thus, nanoparticles with large central cores tend to be more faceted than those with small inner shells. The faceted particles sometimes have pentagonal or hexagonal profiles, but are more frequently irregularly shaped with many sides such as Fig. 2.1 (c).

Carbon nanohorns (CNHs) [10, 11] are widely recognized as a novel and more easily produced carbon nanoparticles, as they do not require any catalyst for its synthesis. Carbon nanohorns always aggregate as particles and hence can be purified at high percentages easily [28]. These particles are spherical with many short single walled nanotubes with cone cap shape either pointing in or out of the spherical shape. This allows them to have high adsorption ability and surface areas.

Carbon nano-onions (CNOs) [29] have a central shell similar to that of buckminsterfullerene (very small). The onions are almost always quasi-spherical in shape, but sometimes they have a slightly faceted configuration at the outer wall. It is important to distinguish between carbon onions and multishelled carbon nanoparticles. Unlike onions, nanoparticles can have a wide variety of shapes, some polyhedral and some rounded, with central cavities of varying sizes, and they frequently contain defects. Moreover, all the electron microscopy evidence points to onions being comprised of concentric shells.

2.2 Arc discharge technique

2.2.1 Electric arc

An electric arc is formed when an electric current passes between two electrodes separated by short distance from each other. In electric arc (we will first consider direct-current arc) one electrode is the cathode, while the other is the anode to be evaporated. The anode and cathode are connected to the power supply, one to the positive pole and one to the negative pole. Basically for arc welding, the arc is started by momentarily touching the anode on to the cathode and then withdrawing it to about 0.5 to 4 mm from the cathode but by arc in liquid the arc discharge can be started by high voltage spark without the touch. When the arc is generated, a current flow, and as it is withdrawn from the anode the current continues to flow in the form of a 'spark' across the very small gap first formed. This causes the air gap to become ionized or made conducting (Figure 2.2 (b)), and as a result the current is able to flow across the gap, even when it is quite wide, in the form of an arc. The anode can be touched on to the cathode before the arc can be started, since the smallest air gap will not conduct a current (at the voltages used in arc) unless the air gap is first ionized or made conducting.

The arc is generated by electrons (small negatively charged particles) flowing from the negative to the positive pole and carbon ion (positive ion) from graphite electrode. The electrical energy is changed in the arc into the light. Approximately two-thirds of the heat is developed near the anode, which burns into the form of a crater, the temperature near the crater being about 4000-6000°C, while the remaining third is developed near to the cathode. As a result an anode connects to

the positive pole will be evaporated. The thicker anode used, the more heat is required to evaporate it, and thus the more current is required. The arc current may vary from 20 to 600 A. [30]

Anyway, the arc discharge does not obey Ohm's law. In many cases of electronics, higher voltage is necessary for higher current but the voltage becomes lower when current is higher in the case of arc discharge. Because arc discharge contains high density plasma which has many positive ions and they also conduct current. When ions and electrons appearing in the inter-electrodes space increase, high current can be conducted because there are more carrier particles. If there are more carrier particles, the resistance can become low. This is the reason why the character of the arc discharge is opposite to the tendency of Ohm's law. So, if the materials of the electrodes which can emit ions with lower temperature are used to generate arc discharge, the arc temperature can be lower.

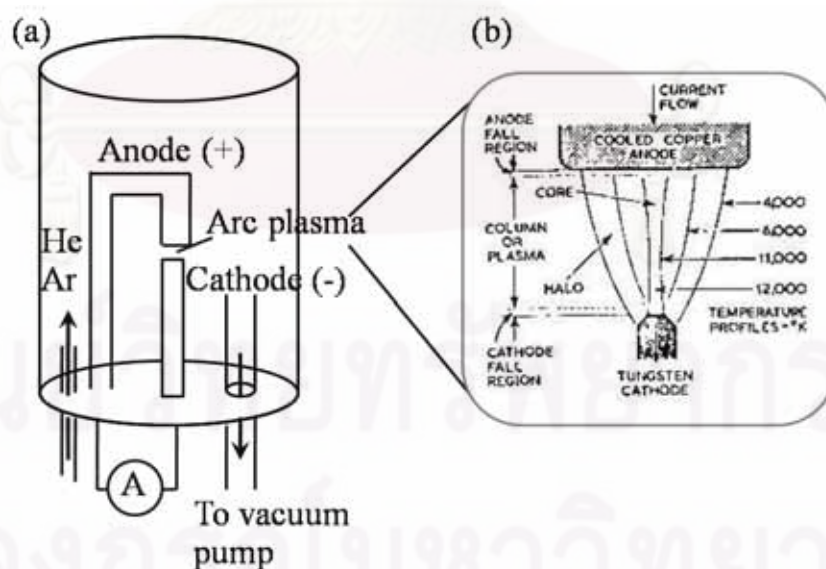


Figure 2.2 (a) Schematic of an arc discharge chamber [31]

(b) A characteristic electric arc [32], arc current 200A in nitrogen at atmospheric pressure.

2.2.2 Production of carbon nanotubes by arc discharge technique [31]

Arc discharge was the first recognized method for producing both SWCNT and MWCNTs, and has been optimized to be able to produce gram quantities of either. The method is similar to the Kratschmer-Huffman method of generating fullerenes and the procedure to make carbon whiskers developed by Roger Bacon over 30 years ago (Fig. 2.2 (a)). Arc discharge synthesis uses a low-voltage (~12 to 25 V), high-current (50 to 120 A) power supply (an arc welder can be used). An arc is produced across a 1-mm gap between two graphite electrodes 5 to 20 mm in diameter. An inert gas such as He or Ar is used as the atmosphere for the reaction, at a pressure of 100 to 1000 Torr. Iijima produced the first MWCNTs by this method. He found that nanotubes formed on the cathode, along with soot and fullerenes. Iijima and Ichihashi and Bethune et al. were the first report on the production of SWCNTs. Both Iijima and Bethune found that SWCNTs could only form by adding metal catalyst to the anode; specifically, Iijima used a Fe:C anode in methane: argon environment, while Bethune utilized a Co:C anode with He environment. These are several variations one can make to tailor the arc discharge process. Currently, most growth is carried out in an Ar:He gas ratio, the diameter of the SWCNTs formed can be controlled, with greater Ar yielding smaller diameters. The anode-cathode distance can be changed to vary the strength of the plasma formed in between. The overall gas pressure has been shown to affect the weight percent yield of SWCNTs. Several metal catalyst compositions produce SWCNTs, but the current standard widely used for SWCNT production average diameter of 1.2 to 1.4 nm. In general, the nanotubes produced by this synthesis method need extensive purification before use. On the other hand, both SWCNTs and MWCNTs made from this process are now commercially available relatively inexpensively, and have been for several years.

2.2.3 Properties of arc plasma [29]

Most models of nanotube growth discussed so far assume that the tubes nucleate and grow in the arc plasma. However, few authors have considered the physical state of the plasma and its role in nanotube formation. The most detailed discussion of this topic has been given by Eugene Gamaly, an expert on plasma physics, and Thomas Ebbesen. This is a complex area, and only a brief summary is possible here.

Gamaly and Ebbesen begin by assuming that the nanotubes and nanoparticles form in the region of the arc next to the cathode surface. They then analyze the density and velocity of carbon vapors in this region, taking into account the temperature and the properties of the arc, in order to develop their model. They suggest that in the layer of carbon vapor adjacent to the cathode surface there will be two groups of carbon particles with different velocity distributions. This idea is central to their growth model. One group of carbon particles will have a Maxwellian, i.e. isotropic, velocity distribution corresponding to the temperature of the arc ($\sim 4000\text{K}$). The other group is composed of ions accelerated in the gap between the positive space charge and the cathode. The velocity of these carbon particles will be much greater than those of the thermal particles, and in this case the flux will be directed rather than isotropic. The process of nanotube (and nanoparticles) formation is considered to occur in a series of cycles, each of which comprises the following stages:

1. *Seed formation* At the beginning of the discharge process the velocity distribution of carbons in the vapor layer is predominantly Maxwellian, and this results in the formation of structures without any axis of symmetry such as nanoparticles. As the current becomes more directed, open structures begin to form which Gamaly and Ebbesen consider to be the seeds for nanotube growth.

2. *Tube growth during stable discharge* As the discharge stabilizes, the current of carbon ions flows to the vapor layer in a direction perpendicular to the cathode surface. These directed carbons will contribute to the extension of single-walled and multi-walled nanotubes. Since the interaction of directed carbons with a solid surface will be much more intense than that of carbons in the vapor layer, the growth of elongate structures will be favored over the formation of isotropic structures. However, the condensation of carbons from the vapor layer at the cathode surface will contribute to nanotube thickening.

3. *Termination and capping* Gamaly and Ebbesen point out that nanotubes are often observed to grow in bundles and that in a given bundle all the tubes appear to begin and end growth at approximately at the same time. This leads them to suggest that instabilities occur in the arc discharge which can lead to abrupt termination of nanotube growth. These instabilities might result from the erratic movement of the cathode spot around the cathode surface or from spontaneous interruption and re-striking of the arc. In such circumstances, carbons with a Maxwellian velocity distribution will again predominate, and the condensation of these carbons will tend to result in tube capping and the termination of growth.

2.3 Background of arc-in-water with gas injection for SWCNHs synthesis

2.3.1 Synthesis of carbon nano-onions in water [22]

The nanoparticles, which have C₆₀ cores surrounded by onion-like nested particles, are generated by an arc discharge between two graphite electrodes submerged in water; the discharge voltage and current were 16-17 V and 30 A, respectively. The nano-onions are mostly found floating on the water surface, with the rest falling to the bottom of the beaker through natural segregation, giving material of high purity. This technique is economical and environmentally benign, and produces uncontaminated nanoparticles which are convenient to separate the products.

2.3.2 Formation mechanism of nanoparticles under arc discharge in water: vapor phase growth [33]

A plasma zone occurs between these electrodes, this is encapsulated by a vapor bubble of the vaporized carbon that is encapsulated by the surrounding submersion liquid (water or nitrogen). The sublimation temperature of carbon is approximately 4000°C, hence the plasma zone is believed to be at this temperature, and hence the bubble will be a carbon vapor not a liquid at these temperatures. The vaporized carbon (from the decreasing anode) can be converted to nano structures in the plasma zone and the gas bubble. Due to these high temperatures gas is produced and bubbles through the liquid in the beaker, with water as the submersion liquid the following reaction occurs at the gas liquid interface



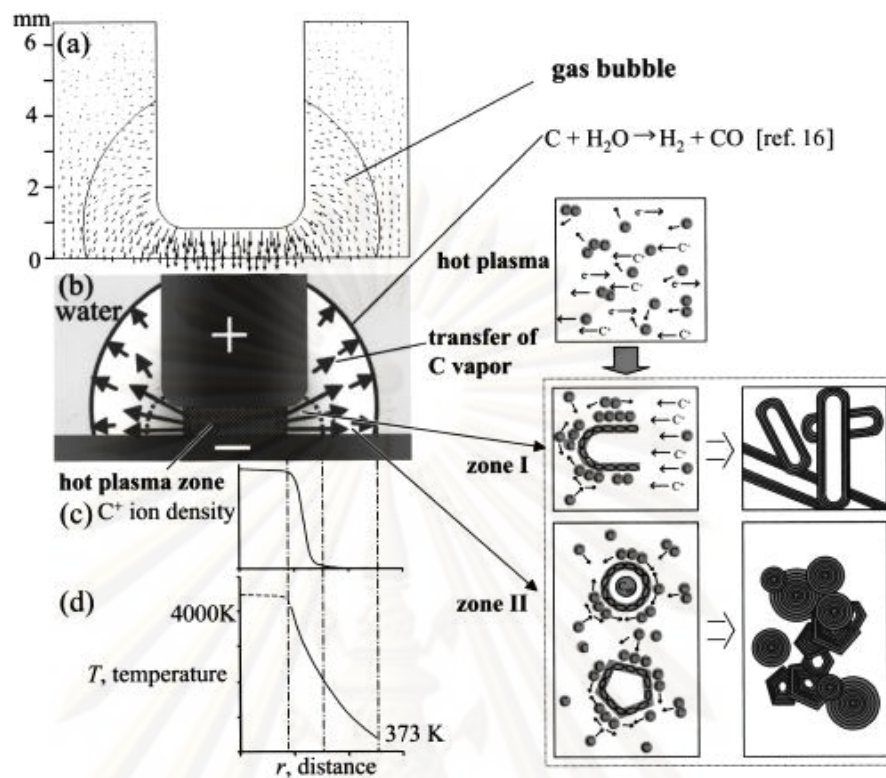


Figure 2.3 Diagram from article that proposed formation mechanism of onions in a water arc [33]. (a) Relative electric field strength, shown by arrows, between a rod anode (17 V) and a flat cathode (ground) in a gas bubble surrounded by water. (b) Direction of thermal expansion from the plasma to the gas-water interface. (c) Qualitative ion density distribution. (d) Temperature gradient obtained from Eq. 2.2 assuming q_c , Q_R , and $dT/dt = 0$. The formation of elongated nanoparticles in zone I and onions in zone II is also shown schematically.

The liquid plays a dual role, both to provide gas to the plasma zone and to quench the carbon vapor, thus enabling the formation of the nanoparticles. The plasma zone is the region with the highest density of atomic vaporized carbon, and

hence structures that are long and produced by directional growth would be preferential in this region from zone I in Fig. 2.3. Where as the surround area of the bubble where there is a low current density there is a production of isotropic structures such as nano-onions, zone II. Controlling the operational parameters can allow the alteration of the products structures such as the submersion liquid and the current through put.

Due to the sharp temperature gradient in the bubble from the plasma to the gas water interface there is a certainty in the solidification of the vaporized carbon. As the melting point of graphite is 3550°C and boiling point is 3930°C, it is assumed that the plasma is approximately mid way at 3727°C. As the interface of the bubble and the liquid would cause the water to boil it is at 100°C. In the case of liquid nitrogen this would be at -196°C. Using radial heat transfer to calculate the heat transfer gradient the heat balance equation is as follows:

$$-\frac{d}{dr}(4\pi r^2 q_k) - \frac{d}{dr}(4\pi r^2 q_c) + 4\pi r^2 Q_R = 4\pi r^2 \rho C_p \frac{dT}{dt} \quad (2.2)$$

where r , q_k , q_c , Q_R , ρ , C_p , T , and t are distance from the arc center, heat transfer rate by thermal conductivity, heat transfer rate by convection, reaction heat, density of the gas, specific heat of the gas, temperature, and time, respectively. To simplify the calculation q_c , Q_R , and dT/dt are assumed to be zero but in the real system they should be significant and all parameters must be highly space and time dependent.

$$q_k = -k \frac{dT}{dr} \quad (2.3)$$

Equation 2.3 (Fourier's Law) with the proportional constant k , can be used to calculate a rough temperature gradient using boundary conditions for both water and liquid nitrogen as the submersion liquids. These were found to be 1209 K min^{-1} [33] and 1308 K min^{-1} [27], respectively for water and liquid nitrogen using boundary conditions of $T = 4000 \text{ K}$ at $r = 2 \text{ mm}$, and $T = 373$ or 77K for water and liquid nitrogen respectively at $r = 5\text{mm}$. It is noted that this simple calculation is only to estimate a rough approximation of temperature gradient.

To explain the production of onions and nanotubes a model of the arc-in-water system in which there are two quenching zones were proposed. In zone (I) the quenching of C vapor occurs within the ion current adjacent to the hot plasma zone. The elongated structures such as nanotubes are expected to be produced because of their epitaxial growth in the C ion current. On the other hand, in zone (II) without the ion current, three-dimensional isotropic growth of nanoparticles is preferable because of the absence of an axis of symmetry. In this case, onions may be produced.

2.3.3 Synthesis of SWCNT with nanohorns by 'arc in liquid' nitrogen [10]

The anode consisting of graphite mixed with Ni and graphite cathode was sustained horizontally in liquid nitrogen (LN). Arc discharge was initiated by touch and release of these electrodes, and sustained by keeping the gap between the electrodes approximately 1 mm. The discharge current and voltage were controlled at 60 A and 20-30 V, respectively. The concentration of Ni in these anodes were varied to 0.0, 0.64, 1.8, 4.6, 9.2, 22.3, 28.1 mol%. When LN was evaporated after the discharge process, a bulky deposit and powdery products were found respectively at the cathode tip and reactor bottom.

When the anode of [Ni]=0.0 mol% was used, SWNHs were observed in the powdery products. Meanwhile, when the anode of [Ni]=0.64 mol% was used, Ni-included SWNHs were found among normal SWNHs. The Ni nano-particles included in SWNHs typically had diameters of 50-100 nm, and encapsulated by several graphitic shells.

When the anode of [Ni]=1.8 and 4.6 mol% were used, most SWNHs turned to include Ni nano-particles and SWCNTs were also observed in this product. This result suggests that excessive concentration of Ni vapor at the arc zone inhibits the formation of the single-walled carbonaceous structures. Therefore, it is considered that relatively inert environment at the arc region is necessary to form these structures even though Ni is supplied to the reaction zone.

2.3.4 Synthesis of SWCNHs using the gas-injected arc in water method (GI-AIW) [11]

As a success of synthesis of SWNHs using arc in LN [10], it was considered that the inertness of bubbles formed at the arc plasma in LN is important for forming the delicate structure of SWNHs. However, the cost of consumable LN will be a problem for scaling it up to a continuous process on a low-cost basis. Meanwhile, an arc in water is superior to an arc in LN in that water is substantially cheaper than LN. Therefore, the method of arc in water (AIW) with the support of gas injection (GI) was studied in this research (Figure 2.4) and it was successful in synthesizing SWNHs.

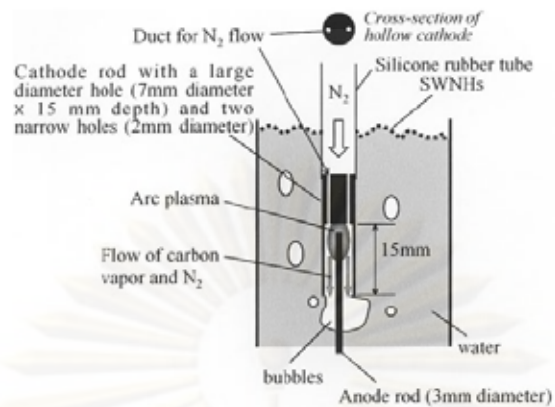


Figure 2.4 Image from articles that showed schematic of reaction system [11].

SWNHs were produced at a large production rate using the arc in water method with N_2 injection. The key condition is that reactive gases must be excluded from the arc zone, maintaining a rapid quenching rate of ablated carbon to form SWNHs. As development of rapid production of SWNHs on a significantly low-cost basis is required to promote the widespread use of SWNHs, the proposed method will give a breakthrough for such a demand.

2.4 Continued literature review on arc discharge model

As mention previously in topic 2.3.2, there are currently several proposed models that explain the production structures formed in arc discharge. The arc as previously described occurs in between the anode and cathode when the circuit is closed. The growth mechanisms are split into the following categories.

2.4.1 Liquid phase growth

More recently there has been articles put forward illustrating the growth of carbon nanotubes using a liquid phase model [34]. This research concluded that liquid carbon played a central role in nanotube nucleation and growth. Base on their observations, and on the known properties of liquid carbon, they proposed the following nanotube formation scenario. When arc-discharge is initiated, the carbon anode is locally heated by electron bombardment from the cathode, causing the surface to locally liquefy and liquid carbon globules to be ejected from the anode. Initially, because of the high vapour pressure of liquid carbon, the surface of a globule will evaporatively cool very rapidly. However, the cooling of the interior of the globule occurs much more slowly, and this causes the liquid carbon to supercool. It is within this supercooled liquid carbon that carbon nanotubes and nanoparticles are envisaged to homogeneously nucleate and grow.

2.4.2 Solid phase growth

Initially the proposal for solid phase growth was put forward in 1994. Harris [35] has been recently revisited and summarized as follows. In the initial stages of arc-evaporation, carbon in the vapour phase (consisting largely of C_2 species) condenses onto the cathode as a fullerene soot-like material. This condensed carbon then experiences extremely high temperatures as the arcing process continues, resulting in the formation firstly of nanotube “seeds” and then of multiwalled nanotubes. Growth terminates when the supply of carbon is exhausted or when arcing finishes. The model is illustrated in Fig. 2.5. An important element of the model is that it requires rapid heating to high temperature.

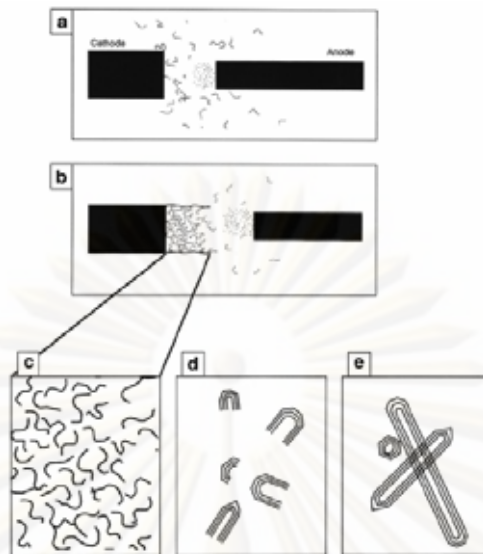


Figure 2.5 Diagram from article that showed schematic illustration of the solid phase growth model for multiwalled carbon nanotube (MWCNT).

(a) Electron bombardment from cathode causes heating of the anode surface, and evaporation of C_2 and other species. These rapidly coalesce into fullerene soot fragments.

(b) Some of the fullerene soot condenses onto the cathode, with the remainder being deposited on the walls of the vessel.

(c), (d) and (e) enlarged views of the interior of the cathodic deposit, showing transformation of the fullerene soot into firstly open-ended “seed” structures and then MWCNT and nanoparticles.

2.4.3 The crystallization model

Based on the viewing of the defects present in nanotubes, it was proposed that growth does not proceed from one end to the other but rather by a crystallization method [35]. Similar to solid phase growth this is believed to be a two step process. Initial the amorphous carbon assembles on the cathode; these are of all

different morphologies. The second stage cooling occurs and graphitization forms on the surface then towards the internal of these deposits.

2.5 Carbon nanotube-metal composite

2.5.1 Preparation by hot-pressing process [44]

A few papers report the fabrication of CNT-metal composites by powder metallurgy techniques and some results on the stability of CNTs toward the solid metal matrix at high temperatures of on the influence of CNTs on the electrical and mechanical properties of the materials.

To study the electrical properties of MWCNT-Al composites, The MWNTs (CCVk, diameter 30 nm) were ground with an aluminum powder and the resulting mixtures were hot-pressed at 793 K. In the obtained material, MWNTs are located mainly at Al grain boundaries and some aluminum carbides were formed, which was attributed to a reaction between amorphous carbon and Al. The electrical resistivity at room temperature increases slightly (3.4-5.5 $\mu\Omega$ cm) with increasing MWNT volume fraction. From room temperature down to 80K all the composites show the typical metallic decrease of the electrical resistivity. At about 80K their resistivity abruptly drops by more than 90%. MWNT-Al composite using unpurified arc-discharge MWNTs also investigated. The composites (5 or 10% MWNTs) were produced by hot-pressing at 873K and hot-extrusion at 773K. The MWNTs were found undamaged and, on the contrary to conventional carbon fiber/systems, no aluminum carbides were detected at the interface with the matrix, even after a heat treatment at 983K. The tensile strength and elongation of the composites are only

slightly affected by annealing at 873K in contrast to those of aluminum. They also studied MWNT-Ti composites using similar samples of MWCNTs (diameter 5-50 nm), containing graphitic particles and amorphous carbon. The powder was remixed and hot-pressed at 1208K. The relative density of a pure Ti specimen prepared as a reference was 98.6% and that of the composite was 95.8%. The formation of TiC was observed but TEM observations showed that the MWNTs themselves did not react with the titanium matrix. Probably, TiC comes from the reaction between amorphous carbon and the matrix. The Young's modulus of the composite is about 1.7 times that of pure Ti. This result may be caused by both TiC formation and the addition of MWNTs. The composite has about 5.5 times the Vickers' hardness of pure Ti. This is associated with the suppression of coarsening of the Ti grains, TiC formation, and addition of MWNTs with extremely high Young's modulus. It is proposed that the MWNTs play an important role in blocking migration of dislocations. The other research prepared CCVD MWNT-Cu composites by similar techniques. The hardness of the composites increases with MWNT fraction (0-25 vol%). Rolling tests reveal that the composites can reach a deformation of 50-60% and have a good isotropy of the mechanical properties.

Thus, these first works have shown the stability of MWNTs in some solid metal environments during the hot pressing or hot-extrusion processes. But the homogeneity of dispersion of CNTs has to be improved and the use of SWNTs has to be tested. The study of more optimized materials will probably confirm the beneficial influence of CNTs on some mechanical properties of metal-matrix composites. The MWNTs, some of which are filled with an iron alloy, are well dispersed in the so-

obtained composites ribbon (40 μ m thick). Thus, it seems that techniques involving molten metals can also be considered to fabricate CNT metal composites.

2.5.2 Preparation of metal nanoparticles embedded in carbon nanotubes [45]

There are several routes to production of catalyst nanoparticles, and the most commonly used methods are described in the follow sections.

2.5.2.1 Impregnated with aqueous solution of metal catalyst

In the impregnation method, a liquid solution containing the catalyst in salt form is applied to the substrate via dipping the substrate, spray coating, spin coating, or micro-contact printing. Soluble salts are typically used, such as acetates or nitrates (e.g., in iron, nickel, or cobalt nitrate [Fe(NO₃)₃·9H₂O, Ni(NO₃)₂·6H₂O, Co(NO₃)₂·6H₂O]). After application to the substrate, the salt solution is often reduced to oxide nanoparticles by calcinations (i.e., heating in air). Metal oxides are stable and improve the catalyst-support interaction at growth temperature---in some cases, metal oxides are used directly as the catalyst. During growth, these oxides are reduced to metal nanoparticles (e.g., using hydrogen) which catalyze the subsequent growth of carbon nanotubes. Note that catalyst decomposition and reduction can occur as part of the deposition process because the nanotube growth is usually performed at elevated temperatures. The density of the nanotubes is simply controlled by the concentration of the catalyst solution, which is typically in the range of 1 to 500 mM. Selective growth on substrates with metal catalysts often involves the use of inked stamps/molds, inkjet printing onto desired areas, or wet coating of a resist-masked substrate.

Mixtures of different metal salts have also been used as catalysts for nanotube growth. The combination of different metal catalysts can enhance the yield of nanotubes. However, with different combinations of metal salts, it becomes increasingly difficult to find an optimum “recipe.” One method to overcome this challenge is to use high-throughput inkjet printing or microarray printing to transfer different catalyst mixtures onto a substrate. Microarray printing has the advantage of being relatively low cost when applied over large areas, and it can provide relatively high spot density ($> 10^3$ spots per cm^2) and experimental flexibility with different mixtures of catalyst solutions. For example, this method was used to study the effectiveness different metal salts to determine the optimal catalyst composition for the growth of multi wall and single wall carbon nanotubes.

It is also possible to deposit catalyst nanoparticles onto a substrate by electrochemical deposition with a metal salt solution. Tu et al. used a solution of 0.01 M of $\text{Ni}(\text{SO}_4)$ and 0.01 M of H_3BO_3 to electroplate Ni nanoparticles onto a Si substrate which was metallized with Cr. By changing both the current density and time during electrochemical deposition, it is possible to control the density of the particles and hence the density of the carbon nanotubes on the substrate.

The catalyst support for nanotubes could also be in the form of a powder/nanoparticles (typically alumina, silica, or graphite). In the impregnation of metal catalysts method, these powders are impregnated with the catalyst. For example, graphite can be impregnated with a 40 vol% ethanol/60 vol% water of iron (III) oxalate to form a 2.5 wt% Fe/graphite sample. This sample was next dried in nitrogen at 250°C and reduced in hydrogen to form metallic iron which was then used to catalyze the growth of multiwall nanotubes using acetylene at 700°C . the impregnation method has also been used to prepare catalyst for single wall nanotubes

as well. The most promising catalyst that has been reported by such method is a Co-Mo metal supported on silica. The impregnation technique is often used for the bulk production of nanotubes. At the end of the reaction, the support can be removed by dissolution in strong acid or alkali to yield the carbon structures.

Another metal catalyst preparation route is co-precipitation which involves the reaction of metal salt solutions with ammonium bicarbonate form metal carbonates. The metal carbonates can be reduced to metal oxides by calcinations and further reduced to the metal catalyst during growth using hydrogen.

Metal catalysts are especially useful for coating nanoplanar geometries such as wires or tips. These surfaces can either be dipped in the catalyst solution or the solution can be spin-coated onto the substrate.

2.5.2.2 Thin film deposition

Another common technique of depositing the metal catalyst is by physical vapor deposition. A very thin film of Fe, Co, or Ni is carefully deposited on a substrate using sputtering or evaporation. The film thickness is usually in the few nanometer range and is monitored during deposition using a quartz oscillator-type film thickness monitor for accuracy. When this thin film is heated up to a high temperature (such as the growth temperature), the thin film breaks up and coalesces to form nanoclusters due to increased surface mobility and strong cohesive forces of the metal atoms. These nanoclusters then catalyze the growth of the carbon nanotube. In general, the size of the nanoclusters formed can be controlled by the thickness of the catalyst film, by the temperature, or by the annealing time. Thickness, high temperatures, and lengthy annealing times lead to the formation of larger metal clusters due to increased surface migration of the metal atoms. Although these parameters

may be used to control the average size of the nanoclusters (i.e., diameter of resultant nanotubes), one should note that the formation of nanoclusters from the metal film is a random process and thus there will still be a distribution in the diameters of the structures.

Multilayer metal films have also been used to catalyze nanotube growth. A noncatalyst metallic underlayer can be used to control the surface properties of the catalyst or the deposition yield as discussed earlier. Single wall nanotubes have been grown using a three layer metal film containing 0.2 nm Mo on 1 nm Fe on 10 nm Al on a silicon substrate. These authors showed that the metal films formed Fe/Mo catalyst particles of ~ 2 nm diameter which seeded the single wall nanotubes. The advantage of using catalyst thin films is that they can easily and accurately be patterned by using masking or etching techniques based around photolithography or electron beam lithography. In fact, individual freestanding nanotubes have been deposited using this process.

Note that when the metal film thickness exceeds a few tens of nanometers, nanoclusters are no longer formed and the film forms islands a few micrometers in size. These large micrometer-size islands/particles usually do not catalyze filament growth but instead absorb carbon into their bulk. Nanotube growth is usually found around the grain boundaries of metal islands. This is because smaller (sub-micrometer) catalyst particles are often present around the grain boundaries. Baker et al. also observed that carbon filament growth occurred only from the edges of macroscopic Fe foil. In this case, the catalyst material probably easily detached at the metal foil edges to form small catalyst particles which nucleated the carbon filaments. Note that large (micrometer-sized) catalyst grains or thick continuous catalyst films do not nucleate nanotubes. The uniform growth of nanotubes inside

large metal grains or catalyst metal substrates is only possible if nanoparticles are present on the surface of the metal as described in the next section.

2.5.2.3 Thick metal catalyst film coating

Nanotubes can be grown with high yield on thick catalyst metal films or catalyst metal substrates when surface treatment techniques are first used to roughen the substrate surfaces. Mechanical roughening (e.g., by using sandpaper) or electrochemical etching may be used to generate a coarse surface. Plasma etching or ion bombardment has also been used to increase the roughness of the metal surface and to generate submicrometer metal islands/particles. These surface roughening techniques generate the small catalyst particles needed to grow carbon filaments. An alternative technique is to oxidize the metal surface through heating in oxygen or by rusting formed from the rusty, porous oxide surface by decomposing it with a reducing gas (e.g., H_2).

2.5.2.4 Colloidal method

Colloidal metal (or oxide) particles have also been used to catalyze the growth of nanotubes. Colloids are usually synthesized (or bought) in liquid suspensions where the colloid are separated by adsorbed charged species or organic molecules. The advantage of using colloids is that these can be highly homogenous in size and can be synthesized in diameters down to 2 nm. Thus, the use of colloidal catalysts allows the growth of nanotubes with well defined diameters, in contrast to the other techniques mentioned above which tend to produce nanotubes with a significant variation in diameter (except for the growth of single nanotubes from a small catalyst patterned dot where the catalyst is essentially fixed in

size/volume). Cheung et al. describes the preparation of monodisperse Fe clusters with different diameters and uses these to catalyze the growth of single wall nanotubes supported on an oxidized Si substrate. Li et al. have also synthesized colloids of diameters varying from 3 to 14 nm to catalyze nanotube growth. Colloidal metal suspensions can in general be applied to the substrate using similar techniques as for the impregnation method. Additionally, colloidal solutions in which the particles are separated by charge can be easily applied/adhered to substrates which have been functionalized with oppositely charged surface layers.

2.5.2.5 Sol-gel technique

The sol-gel technique has also been used to prepare catalyst for both multiwall and single wall carbon nanotube synthesis. Sol-gels impregnated with metal catalysts have very high surface area, high porosity, and ultralow density--- these characteristics lead to a high yield of nanotubes during growth. For example, a Fe-Mo catalyst was prepared by the sol-gel technique based on supercritical CO₂ drying and then used for single wall carbon nanotube synthesis. This catalyst was reported to be capable of deposition yield of over 200% compared with the original weight of the catalyst for a 1 hour deposition. The catalyst was active for 6.5 hours of growth, yielding 600% weight gain a high surface area, high porosity, and good metal-support interaction. As yet, no other research group has been able to exceed the yields of single wall carbon naotubes on a supported substrate by sol-gel.

2.5.2.6 Unsupported/floating catalyst method

The floating catalyst method is commonly used for the bulk/mass production of nanotubes by chemical vapor deposition (CVD). The main

advantage of using this technique is that purification is not required to recover nanotubes from the substrate. The simplest method is to inject catalyst nanoparticles (e.g., in the form of a colloidal/particle suspension or organometallic precursors with a carbon feedstock) directly into the CVD chamber. In this case, a vertical CVD chamber is usually used so that the nanotubes grow as the catalyst particles fall from top to the bottom of the chamber. This technique has been used to prepare vapor grown carbon fibers for over 20 years.

Organometallic compounds are often used as precursors for the catalyst. Examples of organometallic compounds that have been commonly used are metallocenes, iron pentacarbonyl, and iron (II) phthalocyanine. These precursors are usually sublimed and catalyst nanoparticles are formed *in-situ* when the compound is decomposed/reduced by heat or hydrogen. A double stage furnace is typically needed because of the different temperatures needed for organometallic sublimation and nanotube growth. In general, the sublimation of metallocenes offers little control over the structural parameters of the nanotubes such as length and diameter, although it has been shown that by varying the relative concentration of the metallocene to carbon in the gas phase the average diameter of the structures may be change. An improvement over the double stage furnace is to use a syringe pump and atomizer to continuously feed a metallocene-liquid carbon feed stock solution into a single stage furnace where nanotube growth occurs. Aligned, high yield and pure multiwall carbon nanotubes can be obtained with conversion rate of 25% of the carbon input using this method. Very often, the floating catalyst technique leads to highly dense/close-packed nanotube deposition where essentially only upward (i.e., “aligned”) growth of the nanotubes is possible.

Interestingly, the floating catalyst method can also be used to selectively grow nanotubes on substrates. It was observed that multiwall carbon nanotubes grown by CVD of ferrocene and xylene at 800°C only occurred on silica (SiO₂) surfaces and not on Si surfaces. Thus, by using lithographic means to pattern SiO₂ on a Si substrate, selective growth of nanotubes was obtained. The multiwall nanotubes were aligned and grew perpendicularly from the SiO₂ surfaces. In this case, it was suggested that it was the good catalyst-support interaction between SiO₂ and Fe that led to the growth of nanotubes. If metal layers of nickel (Ni) were patterned onto Si, the nanotubes were seen to lift these metal patterns during growth. Such aligned nanotubes have also been grown on gold and MgO substrates and palladium seeds.

Typically, metallocene assisted CVD of hydrocarbons (e.g. benzene, xylene) produces multiwall carbon nanotubes at lower temperatures (~700°C) whereas a combination of multiwall and single wall nanotubes are produced at much higher (>900°C) temperatures. For example, pyrolysis of iron pentacarbonyl with benzene at 900°C leads to single wall nanotube formation. Nickelocene and cobaltocene were reported to be more favorable for single wall nanotube than ferrocene, although no differences in single wall nanotube yields were observed when binary mixtures of metallocenes were used, except that the nanotubes appeared to be “cleaner” when mixtures were used.

“HiPCO,” developed at Rice University, is also a process involving a high pressure gas phase catalytic process for single wall nanotube growth. The catalyst is formed *in-situ* by the thermal decomposition of iron pentacarbonyl in a heated flow of CO, and growth is performed at pressures ranging from 1 to 10 atmospheres (atm) and temperatures ranging from 800 and 1200°C. The optimum condition for maximum yield was at 1200°C and 10 atm. The rate at which the

reactant gases were heated also had substantial effects on the amount and quality of nanotubes produced. The addition of small amounts of methane (0.7% by volume) produced clean nanotubes and increased the such a process is continuous and is being currently scaled up to produced larger quantities of single wall nanotubes (marketed as HiPCO™ single wall nanotubes by Carbon Nanotechnologies Inc.)

2.5.3 Literature review on preparation of carbon nanoparticles together with metal nano-particles by using arc discharge technique

2.5.3.1 Arc-discharge in solution method [16, 46]

This research proposed by Bera et al. Carbon nanotubes (CNTs) were synthesized in a reactor with two graphite electrodes immersed in 2.087 mM PdCl₂/HCl solution. TEM and XPS studies confirmed that the Pd-nanoparticles-filled CNTs are being formed during the arc-discharge in solution. In HCl medium, PdCl₂ form a palladium tetra-chloro-square-planar complex, [PdCl₄]²⁻, according to reaction:



During the arc-discharge in solution process, simultaneous formation of CNT and reduction of [PdCl₄]²⁻ to Pd-nanoparticles and their *in-situ* encapsulation inside the CNTs have been taken place. The author proposed the mechanism of reduction of palladium chloride into Pd- nanoparticles as the following possibilities may be considered:

1. Carbon monoxide and hydrogen might have reduced Pd-ions to Pd in solution. Such gases were expected to form near the electrodes during arc-discharge process as follows:



2. The temperature at the site of the arc is expected to be greater than 3000°C, while the decomposition temperature of PdCl₂ is 738°C at one atmospheric pressure. Due to the presence of four coordinate bonds, decomposition of [PdCl₄]²⁻ is easier than that of the PdCl₂. Such thermal decomposition process possibly formed atomic palladium and chlorine gas near the electrodes.

3. The plasma region near the electrodes that was formed due to the arc-discharge is an excellent source of electrons. The Pd-ions near the solution-vapor interface might have reduced to Pd atoms accepting electrons from such electron pool.

4. The formation of atomic Pd through electrochemical process under the applied bias is another possibility.

The author also proposed that rolling of graphitic sheets from the anode formed graphitic tubules during the present process of arc-discharge in solution. Pd-nanoparticles thus simultaneously formed, were encapsulated in the CNTs during rolling of graphene sheets. The possible scheme of simultaneous formation and encapsulation of Pd-nanoparticles in CNTs is shown in Fig. 2.6.

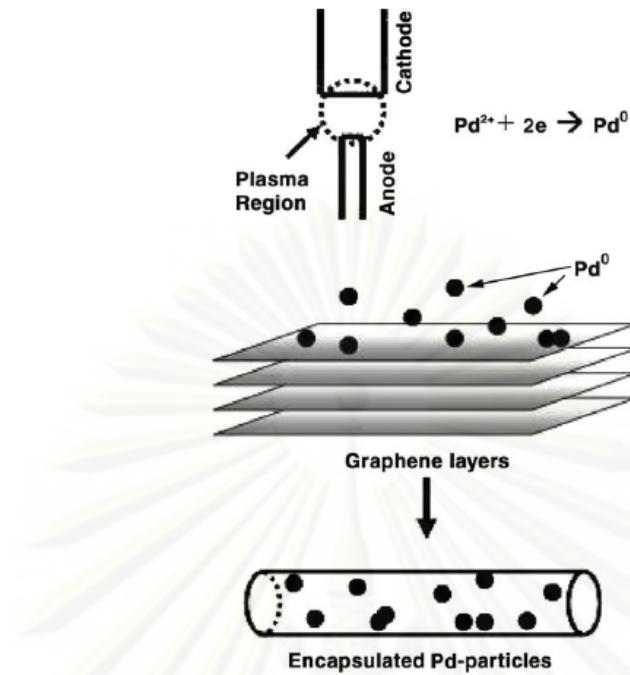


Figure 2.6 Diagram from article that showed schematic formation of Pd-nanoparticles-filled CNT during arc-discharge in solution process.

2.5.3.2 Arc-discharge between graphitic carbon rod and metal rod in liquid nitrogen [47, 48]

Charinpanitkul et al. [47] employed graphitic carbon rod as the anode and iron rods were set as the cathode in liquid nitrogen arc discharge. They concluded that use of iron rods as cathode could provide carbon nanocapsules with iron nanoclusters as the core. Typical TEM image (Fig. 2.7) reveals that under some certain conditions of arc discharge in liquid nitrogen carbon nanocapsules (CNCs) with mean diameter of 50-400 nm could be synthesized. It could be confirmed that making use of pure iron-carbon electrodes for arc discharge in liquid nitrogen could provide higher production yield of carbon nanoparticles.

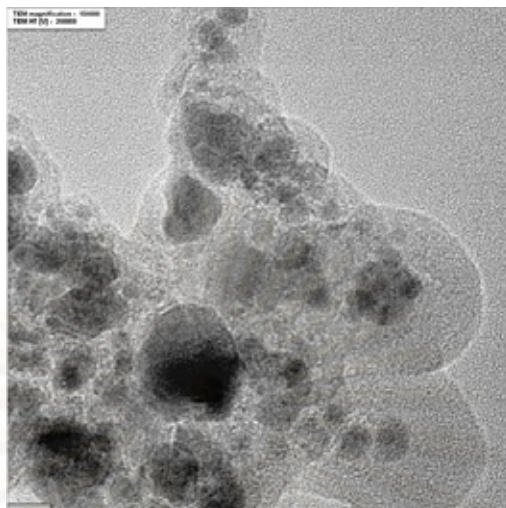


Figure 2.7 Typical TEM image from article [47] that showed carbon nanocapsules containing Fe core. The nanocapsules existing in cathode deposit was obtained from arc discharge using carbon-iron electrodes with arc current of 100A in liquid nitrogen.

Moreover, the author [48] also proposed a new strategy for single-step synthesis of copper and carbon nanoparticle composite by arc discharge in liquid nitrogen. The synthesized products consist of carbon nanoparticles which include multi-walled carbon nanotubes (MWCNTs), single-walled carbon nanohorns (SWCNHs) and multi-shelled carbon nanocapsules (MSCNCs) containing Cu clusters inside. Evidence of transmission electron microscopic analyses (in Fig. 2.8) reveal that under with arc current of 180A arc discharge between copper and graphite electrodes in liquid nitrogen could provide MSCNCs with narrow size distribution in range of 70-150 nm. From spectroscopic analyses (Raman spectroscopic and X-ray diffractometry) confirm that copper nanoparticles are cuprite (Cu_2O)

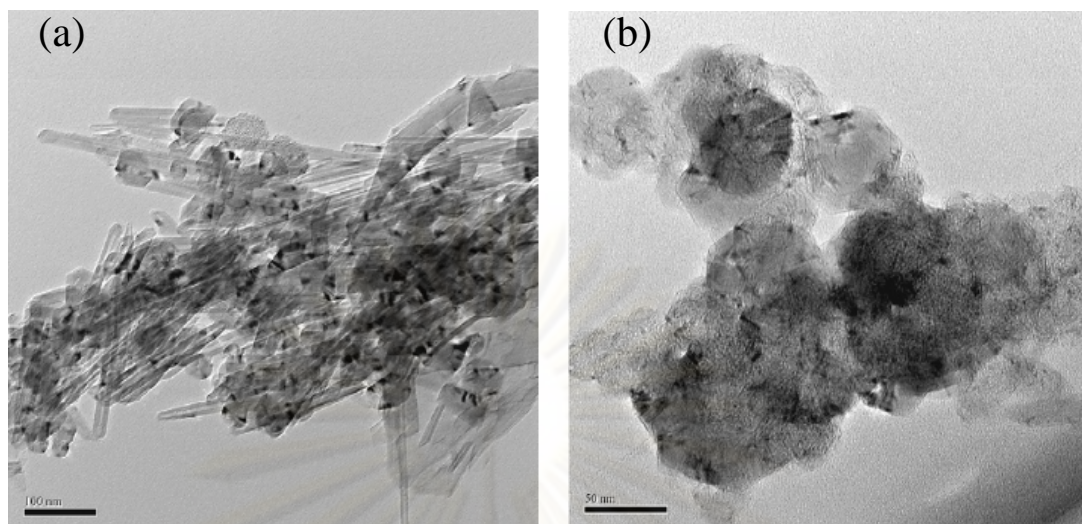


Figure 2.8 Typical TEM image from article [48] that showed (a) MWCNT/cuprite (Cu_2O) composite and (b) MSCNC/cuprite (Cu_2O) composite.

CHAPTER III

EXPERIMENTAL PROCEDURE

3.1 Synthesis of SWCNHs: Influence of water temperature

3.1.1 Electrodes

As shown in Fig. 3.1 a cathode was a hollow graphite rod of 12 mm diameter with a large hole of 8 mm diameter and 25 mm depth on its bottom. The other side of the cathode had two narrow channels of 2 mm diameter and 25 mm depth to inject N_2 gas into the arc zone. The anode was a graphite rod of 3 mm diameter with 75 mm length.

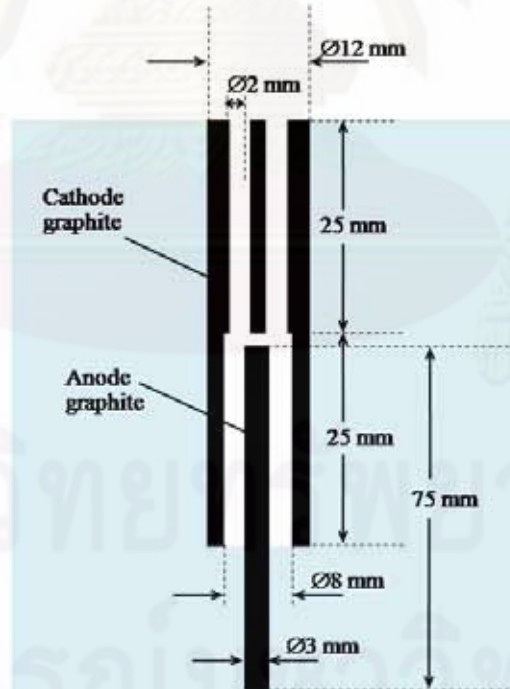


Figure 3.1 Dimension of cathode and anode which were employed in the synthesis of SWCNHs by GI-AIW method.

3.1.2 Experimental method

The apparatus used in this study is schematically shown in Fig. 3.2. Arc discharge was generated at 80A (40V) between electrodes submerged in water by a DC power supply (Shindaiwa, STW200A).

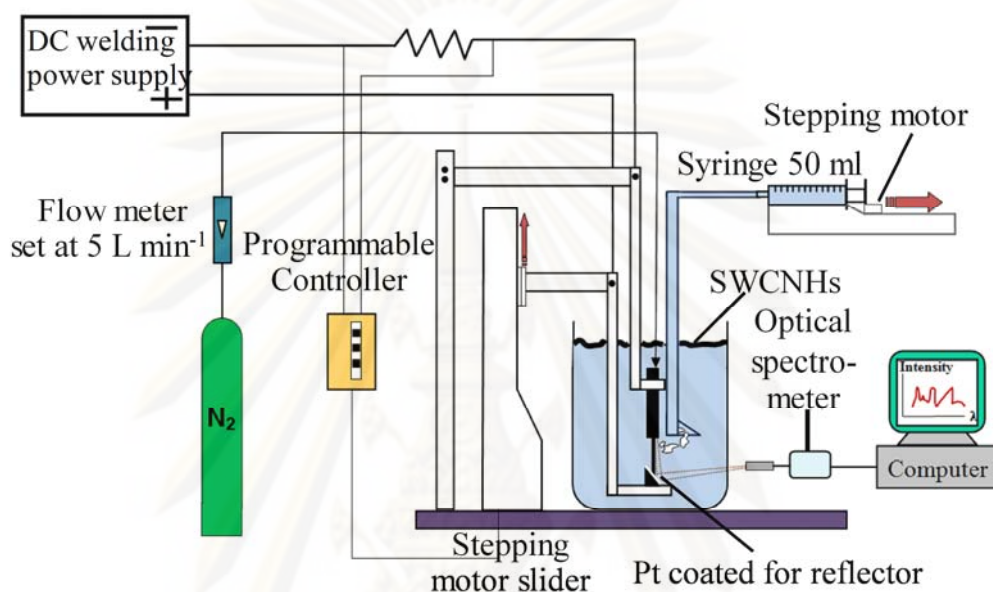


Figure 3.2 Experimental set-up for synthesis of SWCNHs by Gas-Injected Arc-in-Water (GI-AIW) method.

N_2 was supplied from a cylinder at a constant flow rate of 5 L min^{-1} . This flow rate was employed because a previous work [12] revealed that the gas resident time with this gas flow rate leads to a preferable quenching rate of carbon vapor at approximately $2.1 \times 10^6 \text{ K s}^{-1}$ to form SWCNHs. Moreover, the N_2 -injection was necessary to produce SWCNHs because water vapor that reacts with carbon vapor must be purged out. In the present apparatus, the anode was raised up toward a static cathode to keep the inter-electrode gap constantly during the anode is consumed by the arc discharge. The anode-ascending speed was controlled at 1.5 mm

s⁻¹ to continue the arc discharge for 15 seconds by a stepping motor slider (Oriental Motor, EZS3-15M). The inter-electrode gap to sustain arc discharge was approximately 0.45 mm. To investigate the influence of water temperature, the temperature was varied to 2, 23, 46, 62 and 79°C. During the arc discharge, SWCNHs were continuously produced and they floated on the water surface because of their hydrophobic behavior.

The experimental data of synthesis of SWCNHs at various water temperatures are shown in appendix A. The graph of arc current and voltage which was recorded during arc discharge are also shown in experimental data.

3.1.3 Characterization of SWCNHs

3.1.3.1 The weights of the floating SWCNHs and the consumed anode were weighed to determine the yield and the production rate of SWCNHs. In our condition, energetic carbon ions colliding to the cathode surface did not cause the consumption of the cathode, but they were deposited on the cathode surface.

3.1.3.2 A transmission electron microscope (TEM; JEOL, JEM-1010) in Fig. 3.3 was used to characterize the morphology of SWCNHs. TEM is a microscopy technique whereby a beam of electrons is transmitted through an ultra thin specimen, interacting with the specimen as it passes through. An image is formed from the interaction of the electrons transmitted through the specimen; the image is magnified and focused onto an imaging device, such as a fluorescent screen, or to be detected by a sensor such as a CCD camera.



Figure 3.3 Transmission electron microscope (TEM; JEOL, JEM-1010).

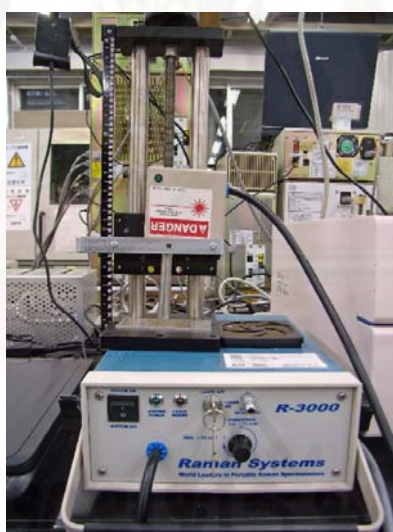


Figure 3.4 Green light Raman spectroscopy (Raman Systems, R-3000).

3.1.3.3 Raman spectroscopy (Raman Systems, R-3000) which is shown in Fig. 3.4 was used to evaluate the crystallinity of the as-grown SWCNHs. The Raman effect occurs when light impinges upon a molecule and interacts with the

electron cloud and the bonds of that molecule. For the spontaneous Raman effect, a photon excites the molecule from the ground state to a virtual energy state. When the molecule relaxes it emits a photon and it returns to a different rotational or vibration state. The difference in energy between the original state and this new state leads to a shift in the emitted photon's frequency away from the excitation wavelength. The shift in energy gives information about the phonon modes in the system. In direct imaging, the whole field of view is examined for scattering over a small range of wave numbers (Raman shifts).

3.1.4 Characterization of gas emerging from arc zone

In this study, gas emerging from the reaction zone was also investigated to elucidate the reaction mechanism. A gas-collector glass tube was used to collect the gas bubbles which were released from the cathode hole. The gas sampling via a glass syringe (50 ml) was automatically started after the arc discharge was continued for 3 seconds. The collected gas was analyzed by a gas chromatograph (Shimadzu, GC-14B) with TCD detector using a packed column (Unibeads C 60/80; Waters, Porapak-Q). The column temperature was controllably constant at 30°C. Helium gas was used as carrier gas. Figure 3.5 shows the gas chromatograph that was used in this study. The data of gas concentration from GC curve is shown in appendix A.



Figure 3.5 Gas chromatograph (Shimadzu, GC-14B) with TCD detector.

3.1.5 Characterization of optical spectra emitted from arc plasma zone

In addition, the optical spectra of radiation from the arc plasma were recorded by an optical spectrometer (Ocean Optics, USB2000) to estimate the arc temperature and to analyze radical formation. For this spectral analysis, a reflector coated with Pt was used to introduce the light from the arc zone to an optical fiber which is shown in Fig. 3.6. A spectrometer is used in spectroscopy for recording spectral lines that consist of wavelengths and radiation intensities and can operate in the range of 200-850 nm with 600 grating line.

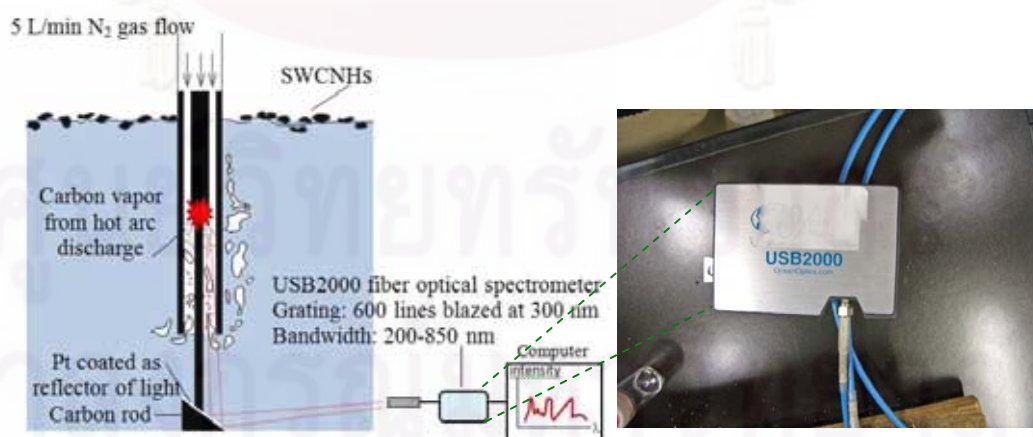


Figure 3.6 Schematic illustration of recording the spectra from arc plasma zone by using fiber optical spectrometer (Ocean Optics, USB2000).

3.2 Influence of Pd wire diameter on synthesis of SWCNHs/Pd nanocomposite

3.2.1 Materials and procedures

The cathode which was a hollow graphite rod with the same dimension as shown in Fig. 3.1. The anode was a graphite rod with of 3 mm diameter. The anode was drilled to have a hole of 1 mm in diameter and a depth of 24 mm at the centre of the anode rod.

High purity palladium wire (99.95%, Nilaco) with the length of 23 mm and various diameters of 0.1, 0.3, 0.5, and 0.8 mm was employed in this study. The Pd wire was inserted in the 1 mm-anode hole.

The dimension of graphite cathode, anode and Pd wire which were used for synthesis of SWCNHs/Pd nanocomposites is shown in Fig. 3.7. The palladium metal wire was inserted in this anode hole with various diameters of 0.1, 0.3, 0.5 and 0.8 mm, and 23 mm in length. We used the same DC arc current (80A, 40V) and N₂ gas flow rate (5 L min⁻¹) that was used for the synthesis of SWCNHs in water at room temperature for this study. The anode is raised up toward a static cathode with constant speed of 1.5 mm s⁻¹ to continue the arc discharge for 15 seconds. During the arc discharge, SWCNHs/Pd composite was continuously produced, and they floated on the water surface because of their hydrophobic behavior. After arc discharge, Pd wire was completely consumed. The experimental data of preparing SWCNHs/Pd nanocomposites are shown in appendix B.

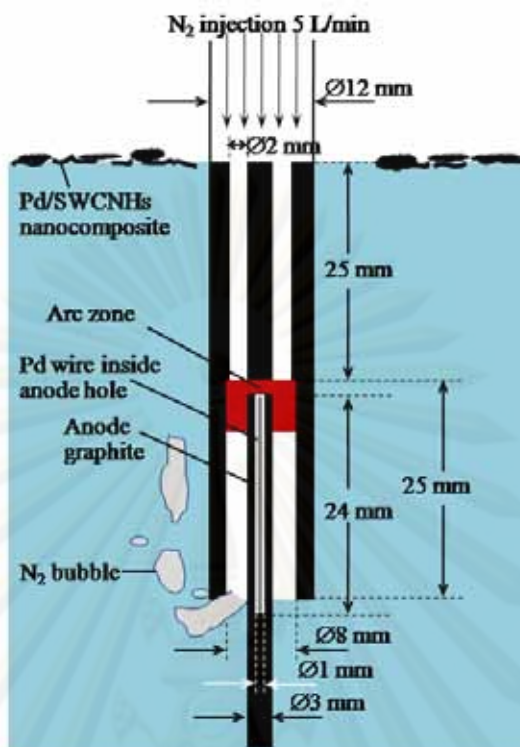


Figure 3.7 Dimension of electrodes and the structure of apparatus for the synthesis of SWCNHs/Pd nanocomposite.

3.2.2 Characterization of SWCNHs/Pd nanocomposite

3.2.2.1 Production yield of SWCNHs/Pd

The weights of the floating SWCNHs/Pd, the consumed carbon anode and the consumed Pd wire inside anode hole were measured to determine the yield of SWCNHs/Pd nanocomposite.

3.2.2.2 Transmission electron microscopic analysis

The morphology of Pd nanoparticles and SWCNHs were characterized by a transmission electron microscope (TEM; JEOL, JEM-1010) as mentioned in topic 3.1.3.2. From TEM images, the diameter of Pd nanoparticles can

be measured from 500 particles. Then the diameter histograms of Pd nanoparticles were also determined.

3.2.2.3 X-ray diffractometric analysis

The crystallinity of SWCNHs/Pd nanocomposite was characterized by X-ray diffractometer (XRD; RINT2100 with $\text{CuK}\alpha$ radiation under the power of 40 kV and 40 mA) which is shown in Fig. 3.8. XRD is the measuring instrument for analyzing the structure of a material from the scattering pattern produced when a beam of radiation (as X rays) interacts with crystalline materials. Crystals are regular arrays of atoms, and X-rays can be considered waves of electromagnetic radiation. The beam of X-rays strikes a crystal and diffracts into many specific directions. The angles and intensities of these diffracted beams are usually presented as a diffractogram in which the diffracted intensity is shown as function of the scattering angle 2θ .



Figure 3.8 X-ray diffractometer (XRD; RINT2100).

3.2.2.4 Raman spectroscopic analysis

Raman spectroscopy (Raman Systems, R-3000) was used to evaluate the crystallinity of the SWCNHs.

3.2.2.5 BET specific surface area analysis

Total BET specific surface areas of SWCNHs/Pd composite were measured by N₂ adsorption (BEL Japan, Belsorp mini). The apparatus for N₂ adsorption is shown in Fig. 3.9. The BET specific surface areas can be determined base on a rule for the physical adsorption of gas molecules on a solid surface.



Figure 3.9 Analytical apparatus for N₂ adsorption (BEL Japan, Belsorp mini) which was used for determining BET specific surface area.

3.2.2.6 Analysis of Exposed surface area of Pd nanoparticles

Exposed surface area of Pd nanoparticles outside SWCNHs aggregates were measured by CO chemisorptions (BEL Japan, BEL-CAT). The apparatus for CO chemisorptions is shown in Fig. 3.10. Since the metal Pd is active

for chemical adsorption of CO [36, 37] the exposed surface area of Pd can be estimated. If the saturated amount of CO adsorbed on Pd is measured. For this measurement, a known amount of CO was supplied to the powder-bed of SWCNHs/Pd nanocomposites in pulsed-way with a carrier gas, He, at a constant flow rate, and CO concentration was monitored in downstream to confirm the saturation and to measure the adsorbed amount of CO. Finally we can determine the specific surface area of metal Pd exposed from SWCNHs matrix.

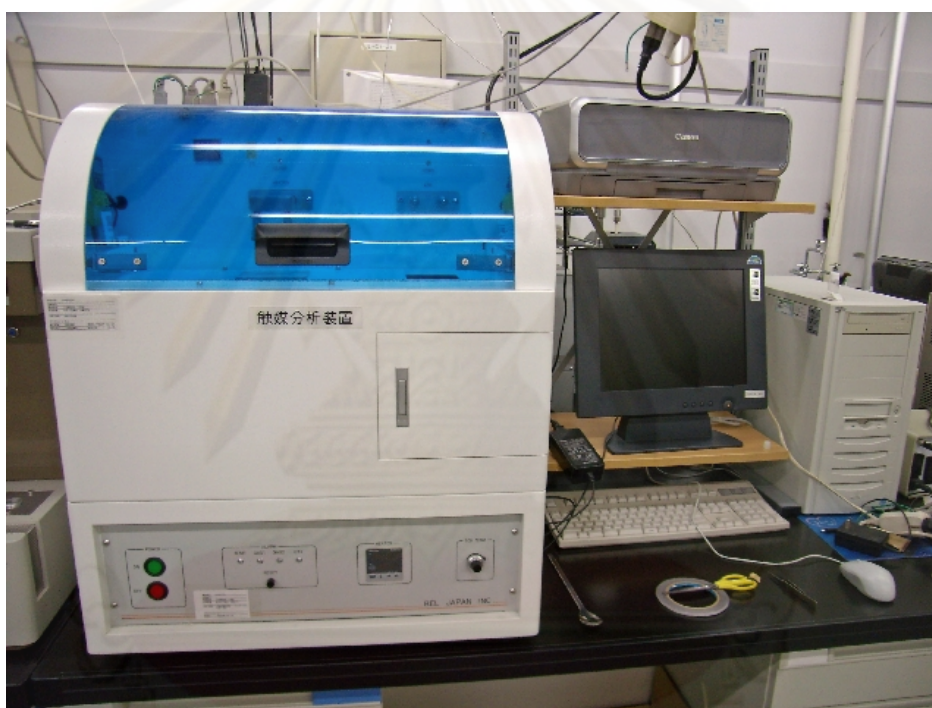


Figure 3.10 Analytical apparatus for CO chemisorptions (BEL Japan, BEL-CAT) which was used for determining exposed Pd surface area.

3.2.2.7 Thermogravimetric and differential thermal analysis (TG-DTA)

The samples were examined by thermogravimetry (TG) and differential thermal analysis (DTA). Thermogravimetric analyzer (TGA-50, Shimadzu) in Fig. 3.11 was carried out in the oxygen flow of 20 mL min^{-1} over the

temperature range of ambient temperature to 1000°C with the heating rate of 10°C min⁻¹. TG analysis or TGA is a type of testing that determines weighted changes as a function of temperature in controlled atmosphere. DTA curve provides data on the transformations that have occurred, such as glass transitions, crystallization, melting and sublimation. In addition the weights of Pd nanoparticles in samples were also determined from TG data.



Figure 3.11 Thermogravimetric analyzer (TGA-50, Shimadzu).

ศูนย์วิทยทรัพยากร
จุฬาลงกรณ์มหาวิทยาลัย

CHAPTER IV

RESULTS AND DISCUSSION

4.1 Influence of water temperature on synthesis of SWCNHs by GI-AIW method

4.1.1 Influence of water temperature on characteristics of SWCNHs

4.1.1.1 Transmission electron microscopic analysis

The morphology of SWCNHs which were synthesized in this research can be observed in TEM images (Fig. 4.1).

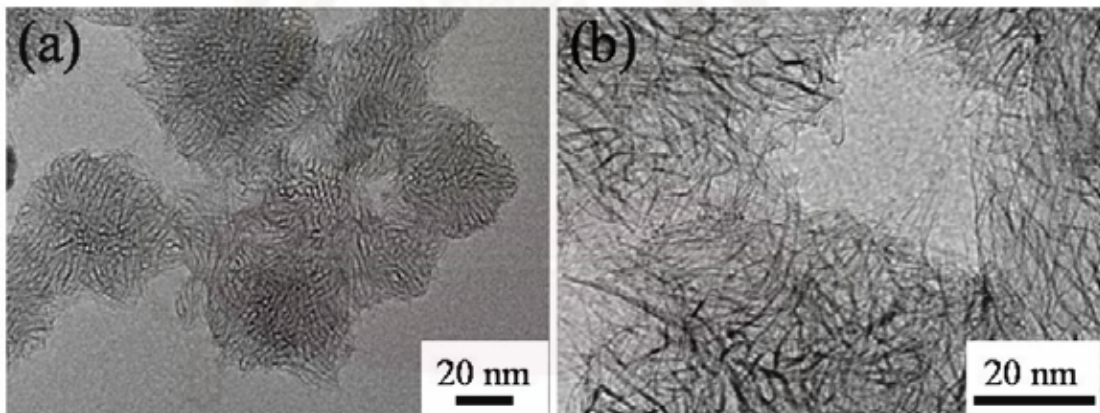


Figure 4.1 Typical TEM images of SWCNHs produced by GI-AIW. (a) Low magnification image. (b) High magnification image.

These images show that SWCNHs consisted of aggregated single-walled horns of which diameters were less than 4.6 nm and length was less than 17 nm. In comparison between typical TEM images of the as-grown SWNHs obtained from a low

temperature condition (2°C) and a high temperature condition (79°C), no significant difference was observed. In both cases, the purity of SWCNHs was c.a. 70 % regarding to our TEM observation. Amorphous carbon was observed as impurities.

4.1.1.2 Raman spectroscopic analysis

Raman spectroscopy was used to evaluate the crystallinity of the as-grown SWCNHs. Figure 4.2 shows a typical Raman spectrum of SWCNHs which were synthesized at 2°C. It is obvious that there are two peaks, graphite band (G-peak) at 1580 cm^{-1} and disorder band (D-peak) at 1330 cm^{-1} of which intensities are almost comparative. Such balance in the intensities of these G-peak and D-peak is common in as-grown SWCNHs [11, 38-39].

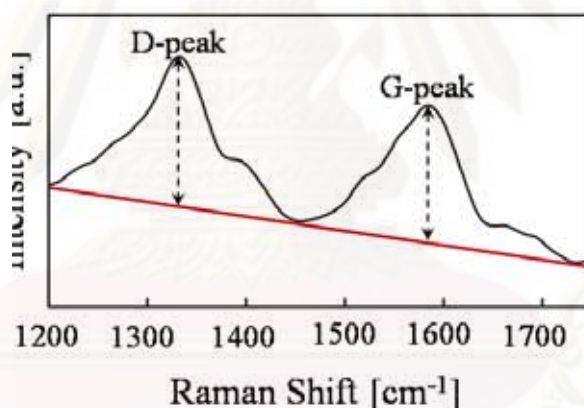


Figure 4.2 A Raman spectrum of as-grown SWCNHs which were synthesized with the water temperature of 2°C.

The dependence of G/D ratio on the temperature of water is depicted in Fig. 4.3 to show a tendency in the crystallinity of the as-grown SWCNHs obtained under different conditions. In general, when G/D ratio is higher, the concentration of crystalline carbon nanostructures would be expected to become higher. Though amorphous impurities would possibly contain in our as-grown SWCNHs, the rather

high G/D ratio (almost ~ 1.0) may indicate the higher purity. Based on our Raman investigation, it is worth to notice that the G/D ratio is hardly affected by the temperature of water. As a result, the purity of SWCNHs would reasonably be independent on the water temperature. This tendency is also consistent with the result obtained by the TEM analysis.

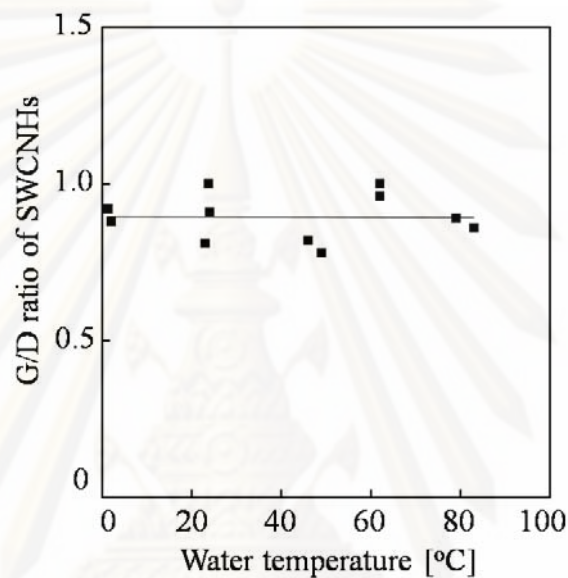


Figure 4.3 Influence of water temperature on G/D ratio in Raman spectra from as-grown SWCNHs which were synthesized by GI-AIW with varied water temperature.

4.1.2 Influence of water temperature on production yield of SWCNHs and by-product gases

4.1.2.1 Yield and production rate of SWCNHs

Figures 4.4 (a) and 4.4 (b) show the yield and the production rate of SWCNHs. The yield is defined as the ratio of the weight of as-grown SWCNHs to the total weight loss of the consumed anode in each batch of the arc discharge process. The yield and the production rate of SWCNHs tend to significantly

decrease with an increase in the water temperature, in which the both yield and production rate can decrease approximately 80% when the water temperature is elevated from 2°C to 79°C. Meanwhile, in the gas analysis, emergence of H₂ gas was also confirmed as explained latter. This H₂ production could be ascribed to the reaction between carbon vapor and water vapor. Although N₂ was introduced to purge water vapor out from the reaction zone in GI-AIW, a certain amount of water vapor could diffuse into this zone, resulting in the inhibited formation of SWCNHs. The potential reaction mechanism is proposed in equations (4.1) and (4.2).



Where, m means the number of carbon in SWCNHs.

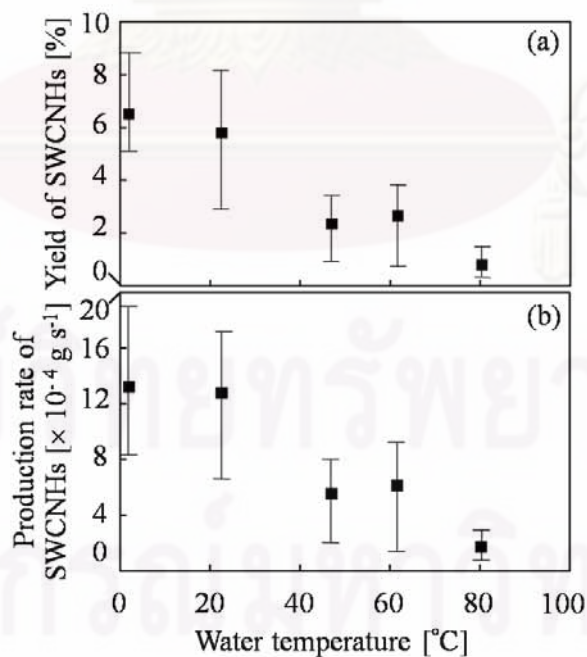


Figure 4.4 Influence of water temperature on (a) the yield of SWCNHs, (b) the production rate of SWCNHs.

4.1.2.2 Production of by-product gases analyzed by gas chromatography analysis

To verify the reaction in Eq. (4.2), formation of gaseous products were analyzed using the gas chromatograph that is shown in Fig. 4.5. Based on the precision of our GC, we intentionally selected the analytical condition to raise detecting sensitivity for H_2 . It should be noted that a single mole of CO formed by Eq. (4.2) corresponds to a single mole of H_2 . In fact, CO production rate was slightly lower than H_2 rate in our analysis, which was close to this stoichiometrical relationship. The gap in the production rates of CO and H_2 is attributed to formation of other by-products, which was not detectable by our GC. Furthermore, we confirmed that O_2 was not produced by arc discharge in water. As a result, H_2 should not be generated by electrolysis of water, but mainly from Eq. (4.2).

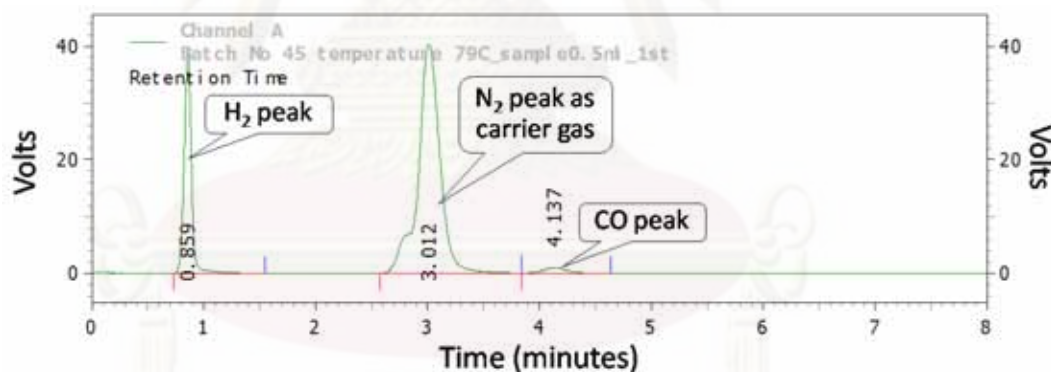


Figure 4.5 A typical GC curve from by-product gases when SWCNHs were synthesized at the water temperature of $79^{\circ}C$.

Then the H_2 production rate was plotted against the water temperature as shown in Fig. 4.6. The H_2 production rate was determined from the gas flow rate multiplied by H_2 concentration obtained from the analysis of gas chromatograph. The H_2 production rate was enhanced from approximately

$1.5 \times 10^{-5} \text{ mol s}^{-1}$ to $7 \times 10^{-5} \text{ mol s}^{-1}$ when the water temperature was increased from 2°C to 79°C .

For comparison, H_2 production rate in the conventional system of arc-in-water (AIW) [22, 33] without N_2 injection was also determined to evaluate the effect of the N_2 injection. It should be noted that the conventional AIW cannot provide SWCNHs due to the dominating Eq. (4.2). Within AIW system, H_2 production rate was so high as $1.02 \times 10^{-3} \text{ mol.s}^{-1}$. However, H_2 production rate in GI-AIW system with low-temperature water (2°C) was two orders of magnitude lower than in the conventional AIW. With an increase in the water temperature to 79°C , the H_2 production rate in GI-AIW became up to approximately 7 percent of that in AIW. This result indicates that N_2 injection can effectively prevent the diffusion of water vapor into the SWCNHs-producing zone. Without N_2 injection the emergence of water vapor could result in the drastic decrease in the yield of SWCNHs.

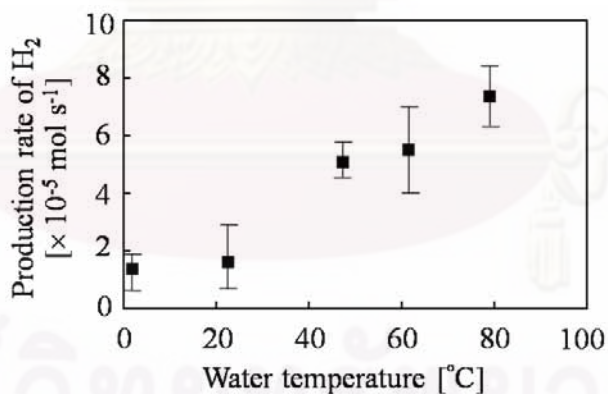


Figure 4.6 Influence of water temperature on the production rate of H_2 gas.

4.1.2.3 Selectivity of SWCNHs production

Figure 4.7 shows the selectivity of the SWCNHs formation (Eq. (4.1)) regarding to products including gaseous by-products (Eq. (4.2)). The selectivity shown in this figure is defined by

$$\psi = \frac{r_{\text{CNH}}}{r_{\text{CNH}} + r_{\text{H}_2}} \quad (4.3)$$

where ψ , r_{CNH} and r_{H_2} are the selectivity for SWCNHs production, the production rate of SWCNHs, and that of H_2 , respectively. It can be observed that the selectivity of SWCNHs production was hindered when the water temperature was increased. This is attributed to the increase in water vapor penetrating into the reaction zone due to the increased water temperature.

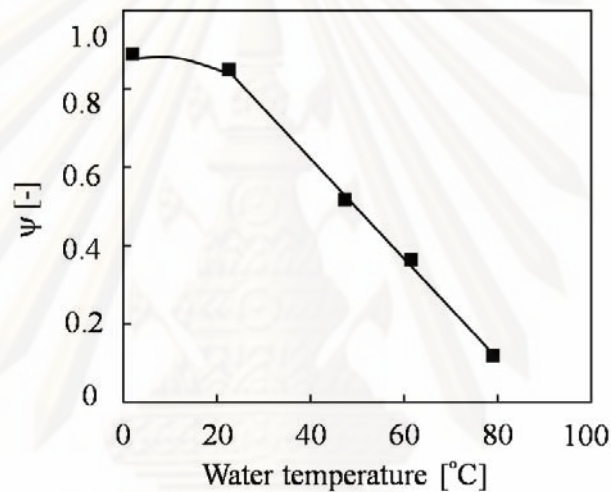


Figure 4.7 Influence of water temperature on the selectivity of SWCNHs formation (ψ).

4.2 Development of mathematical model of phenomena in GI-AIW method

4.2.1 Analysis of optical spectra from arc plasma zone

4.2.1.1 Phenomena obtained from optical spectra

The radical formation in arc plasma zone and the temperature were investigated by analysis of its optical spectra. Figure 4.8 shows typical optical

spectra obtained from three conditions: (1) GI-AIW with low water temperature at 2°C, (2) GI-AIW with high water temperature at 70°C, and (3) conventional AIW at the ambient temperature. In all cases, a peak at 516 nm could indicate the existence of C₂ radical [40]. In the conventional AIW, an outstanding peak at 660 nm would indicate the H radical (H α) formation [40, 41]. However, such H-radical peak can not be observed in both cases of GI-AIW. This result suggests that H₂ production can be significantly hindered in the arc plasma zone of GI-AIW systems since N₂ flow could effectively purge H₂O out from the arc plasma zone. As mentioned above, H₂ was generated from H₂O inside the cathode hole, where SWCNHs were also produced. Here it should be noted that Eq. (4.2) could possibly take place outside the arc plasma zone, but at a SWCNHs-producing zone.

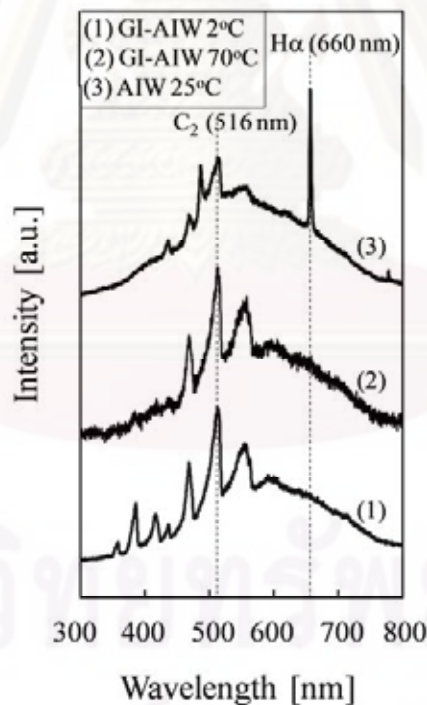


Figure 4.8 Optical spectra from arc plasma in conventional arc-in-water (AIW) and GI-AIW: (1) GI-AIW at water temperature 2°C, (2) GI-AIW at water temperature 70°C, (3) AIW at water temperature 25°C.

4.2.1.2 Conceptual illustration of reaction field in GI-AIW

We propose a schematic diagram for illustrating three zones [(1) arc plasma zone, (2) quenching zone, and (3) downstream zone] which would reasonably exist in the cathode in GI-AIW system, as shown in Fig. 4.9.

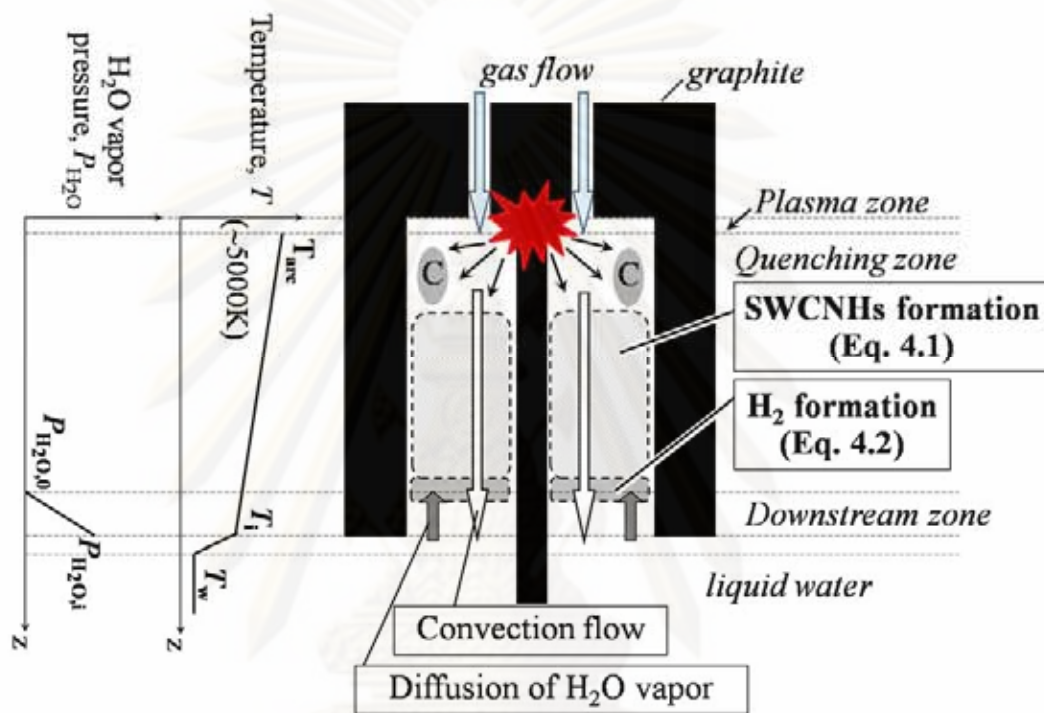


Figure 4.9 Conceptual illustration of the reaction field in GI-AIW with three categorized zones and schematic image of the profiles of temperature and water vapor pressure in the reaction field in GI-AIW system.

In this figure, the profiles of the temperature and the partial pressure of water vapor are also shown as a simple model. The arc plasma zone plays a role to generate carbon vapor. The quenching zone leads to the conversion of carbon vapor to SWCNHs. In the downstream zone, water vapor is generated at liquid-gas interface, resulting in the diffusion of the water vapor toward the quenching zone.

However, with sufficient flow of N₂ injection, the water vapor could not reach the arc-plasma zone so that the H-radical peak would not be seen in the optical spectra of the arc plasma in GI-AIW. Thus, it may be reasonable that Eq. (4.2) would take place at the bottom of the quenching zone.

4.2.1.3 Determination of arc plasma temperature by optical spectra analysis

In this study, the radiation equations known as Planck distribution law and Wien's displacement law, written by Eqs. (4.4) and (4.5) respectively, are used to determine the temperature of the arc plasma from its optical spectra.

$$q_{\lambda} = 2\pi c^2 h \lambda^{-5} (e^{ch/\lambda\kappa T} - 1)^{-1} \quad (4.4)$$

$$\lambda_{\max} T = 0.2884 \quad [\text{cm K}] \quad (4.5)$$

where q_{λ} , T , λ , λ_{\max} , c , h , κ are energy flux of light at a wavelength, temperature, wavelength, wavelength at a maximum radiation, speed of light, Planck's constant and Boltzman's constant, respectively. Figure 4.10 demonstrates one of the determination curve from Eq. (4.4) that was used for estimating arc plasma temperature. The detail of determination of arc plasma temperature is described in Appendix C. As a result, the temperature at the arc plasma zone is estimated to be approximately 5000K at all conditions used in this study. Such high temperature would be responsible for vaporization of carbon anode, leading to emergence of carbon vapor which is essential for carbon nanostructure formation.

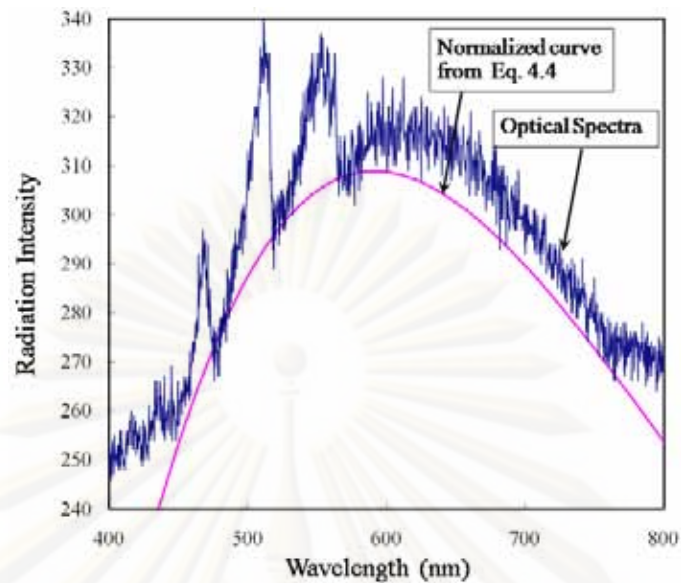


Figure 4.10 Normalized curve from Planck distribution law together with typical optical spectra used for estimating arc temperature.

4.2.2 Model of water vapor diffusion and hydrogen production

In a previous literature, a simple model was proposed to estimate the quenching rate of carbon vapor to produce SWCNHs [12]. At that time, the temperature at the liquid-gas interface was assumed to be the boiling point of water regardless of bulk water temperature. However, this assumption is insufficient for describing the results observed in this study, in which the yield of SWCNHs and H_2 production rate are significantly dependent on the water temperature. To explain the present results, the temperature at the liquid-gas interface at the bottom of the cathode hole must reasonably depend on the water temperature.

4.2.2.1 Mathematic model of heat transfer

We modify the model, considering the temperature profile in the narrow zone adjacent to the liquid-gas interface in liquid phase. Here, the heat flux from the arc plasma zone to the liquid-gas interface and the heat flux from this interface to the bulk water are described by the heat transfer coefficient multiplied by relevant temperature-difference as driving force. These heat transfers are described by Eqs. (4.6) and (4.7).

$$Q_g = h_g (T_{\text{arc}} - T_i) + v_i M_g C_{vg} T_i \quad (4.6)$$

$$Q_w = h_w (T_i - T_w) + v_i M_w C_{vw} T_i \quad (4.7)$$

Q , h , T , v , M , and C_v are heat flux [$\text{J m}^{-2} \text{s}^{-1}$], heat transfer coefficient [$\text{J s}^{-1} \text{K}^{-1}$], temperature [K], velocity of gas or water at interface to axial direction [m s^{-1}], mole density [mol m^{-3}], and heat capacity [$\text{J mol}^{-1} \text{K}^{-1}$], respectively. The subscript g, w, arc, and i mean gas phase, liquid phase, arc plasma zone, and liquid-gas interface, respectively. The terms including v_i represent the effect by convection. T_{arc} in our condition is approximately 5000K as discussed in the above section. In fact, the liquid-gas interface fluctuates due to gas flow. Nevertheless, the location of this interface is assumed to be averaged constantly for the simplified steady state approximation in this study. If the steady state condition is applied, Q_g must be equal to Q_w .

When the bulk water temperature reaches the boiling point, the temperature of the liquid-gas interface should also be equivalent to the boiling point; T_b . Thus, a boundary condition there can be considered as Eq. (4.8).

$$T_i = T_w \text{ when } T_w = T_b \quad (4.8)$$

From the relationship $Q_g = Q_w$ with Eq. (4.8), Eq. (4.9) can be derived.

$$T_i = a + T_w(T_b - a)/T_b \quad (4.9)$$

where a is a complex of parameters as below.

$$a = k_g T_{arc} / [k_w + k_g + v_i A (-M_g C_{vg} + M_w C_{vw})] \quad (4.10)$$

4.2.2.2 Mathematic model of mass transfer

The mass transfer rate of H_2O in the direction from the liquid-gas interface toward the quenching zone through the down stream zone can be written as below.

$$N_{H_2O} = K_p A (P_{H_2O,i} - P_{H_2O,0}) - (Av_0 P_{H_2O,0}/RT_0 + Av_i P_{H_2O,i}/RT_i)/2 \quad (4.11)$$

N_{H_2O} , K_p , $P_{H_2O,i}$, $P_{H_2O,0}$ are H_2O mass transfer rate, mass transfer coefficient, H_2O partial pressure at liquid-gas interface, and H_2O partial pressure at the bottom of the quenching zone, respectively. The term including K_p represents the diffusion effect with a driving force, $P_{H_2O,i} - P_{H_2O,0}$. The terms including v_0 and v_i represent the average H_2O transfer rate caused by the convection flow.

When H_2 is produced in the reaction zone, H_2O vapor must be supplied from the liquid-gas interface to the bottom of quenching zone. From Eq.

(4.2), H_2 production rate r_{H_2} is stoichiometrically equivalent to the mass transfer rate of H_2O (Eq. (4.12)).

$$r_{H_2} = N_{H_2O}. \quad (4.12)$$

Here, we assume that the reaction of Eq. (4.2) is instantaneously fast so that the partial pressure of H_2O at the bottom of the quenching zone can be approximated to be zero (Eq. (4.13)).

$$P_{H_2O,0}=0 \quad (4.13)$$

Because the partial pressure of H_2O can be estimated by Antoine equation, $P_{H_2O,i}$ [Pa] can be written as below.

$$P_{H_2O,i} = \left(\frac{1.013 \times 10^6}{760} \right) 10^{x-y/(T_i - 273+z)} \quad (4.14)$$

where $x=7.96681$, $y=1668.21$, $z=228$, as reported by Ref. 22. Summarizing all the equations above, the partial pressure of H_2O at liquid-gas interface and H_2 production rate can be described as Eqs. (15) and (16).

$$P_{H_2O,i} = \left(\frac{1.013 \times 10^6}{760} \right) 10^{x-y/(a + T_w(T_b-a)/T_b - 273 + z)} \quad (4.15)$$

$$r_{H_2} = (K_p A - v_i A / 2RT_i) P_{H_2O,i} \quad (4.16)$$

In Eq. (4.16), $v_i A / RT_i$ is equivalent to mass flow rate divided by total pressure [$\text{mol s}^{-1} \text{Pa}^{-1}$] based on the ideal gas ($PV=nRT$) assumption. In the present study, the total pressure in gas stream can be considered to be nearly constant at atmospheric pressure, and the mass flow rate of N_2 was also constant ($0.00347 \text{ mol s}^{-1}$). Thus, the value of $v_i A / RT_i$ is determined as $3.4 \times 10^{-8} [\text{mol s}^{-1} \text{Pa}^{-1}]$.

4.2.2.3 Phenomena of water vapor diffusion and hydrogen production

From Eq. (4.15) and Eq. (4.16), T_i and $P_{\text{H}_2\text{O},i}$ at each T_w can be estimated after two parameters (a and K_p) are determined by fitting the calculated r_{H_2} with the experimental values. Here, a and K_p are determined as 55 and 2.2 [$\text{mol m}^{-2} \text{s}^{-1} \text{K}^{-1}$], respectively. Fig. 4.11 shows the calculated relationship between r_{H_2} and $P_{\text{H}_2\text{O},w}$, which can show a characteristic of $r_{\text{H}_2} \cdot P_{\text{H}_2\text{O},w}$ here means the vapor pressure of H_2O directly estimated from bulk water temperature, which can be calculated by substituting T_i by T_w in Eq. (4.14). In this figure, a calculated convex curve compared with the experimental values indicates that the present model can correlate the experimental results fairly well. Once T_i is considered as T_b as assumed in our previous model in Ref. 12, r_{H_2} becomes constant at 9.8 mol s^{-1} , which is not consistent with the present experimental values. Oppositely, if T_i is considered as T_w , the tendency in the increase of r_{H_2} seems linear, leading to an inconsistent result regarding to the experimental values as well.

Based on our newly proposed model, it can be observed in Fig. 4.12 that T_i is higher than T_w in any conditions used in our experiments ($T_w=2-79 \text{ }^\circ\text{C}$). Therefore, the vapor pressure of H_2O at the liquid-gas interface, $P_{\text{H}_2\text{O},i}$,

is obviously higher than the vapor pressure estimated directly from water temperature, $P_{\text{H}_2\text{O},\text{w}}$.

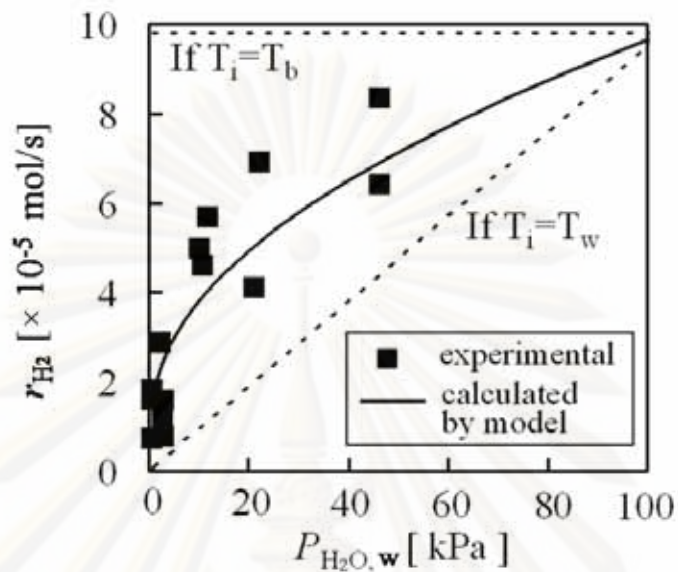


Figure 4.11 Relationship between H_2 production rate and the water vapor pressure directly estimated from bulk water temperature.

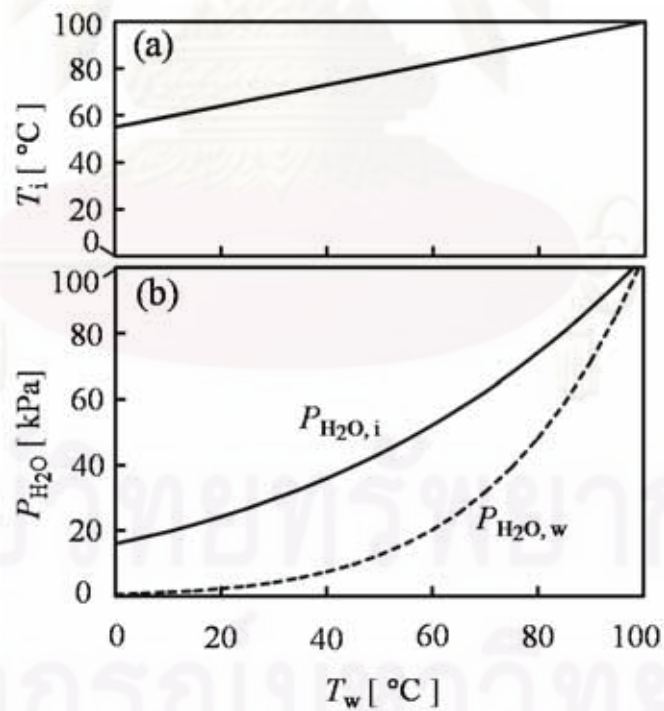


Figure 4.12 Influence of water temperature on (a) temperature at liquid-gas interface (T_i), (b) water vapor pressure at liquid-gas interface ($P_{\text{H}_2\text{O},i}$) and water vapor pressure at the bulk water temperature ($P_{\text{H}_2\text{O},w}$).

Figure 4.13 shows the well-fitting result of the calculated r_{H_2} compared with experimental values. As a result, it is reasonable that the proposed model can acceptably predict the effect of water temperature on the increasing vapor pressure of water diffusing into the GI-AIW system, causing the hydrogen production which will in turn hinder the formation of SWCNHs.

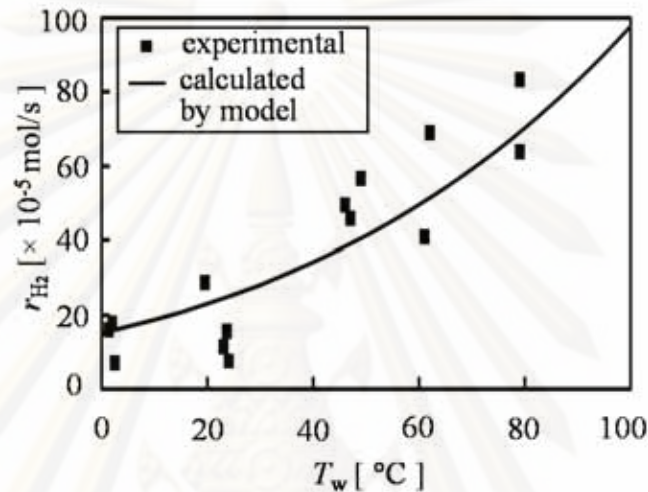


Figure 4.13 Influence of water temperature on H_2 production rate (r_{H_2}).

It should be noted that the position of the interface between the quenching zone and the down-stream zone can be considered to be changeable depending on the water temperature. When the water temperature is high, the zone of the down-stream zone becomes larger, resulting that the position of this interface is shifted upward. When this shift occurs, the quenching zone will shrink. This is why the production SWCNHs is retarded with the elevation of water temperature in the present model. In the mathematical equations, the position of this interface is not apparently shown. However, this effect is included in the parameter fitting work, as the mass transfer coefficient K_p and heat transfer coefficient k_g and k_w are dependent on the length of the down-stream zone.

For further improvement of the simplified model, one may want to consider the mass balance of carbon vapor and H₂O in each reaction zone. For this consideration, the concentration profile of carbon vapor should be discussed. At the present stage, this aspect is not included in the model. However, there is information to give a hint to consider this problem. In our previous article [11], it is reported that the yield of bulky deposit containing multi-walled carbon nanotubes (MWCNTs) is about one-order magnitude higher than that of SWCNHs, and such deposit can sink down to the bottom of the water container or stay at the bottom of the cathode hole. (It should be noted that such deposit is separated from the powdery SWCNHs floating on the water surface.) From the location of this deposit, it is considered that the concentration of carbon vapor in the plasma zone is dominantly higher than in the quenching zone and in the downstream zone. Even if the concentration of carbon vapor in the plasma zone is very high, the carbon vapor there will not contribute to the formation of SWCNHs because the production of SWCNHs in this deposit is observed as negligible, and the most of the carbon vapor in the plasma zone is used to produce the MWCNTs-including deposit. From the comparison between the production rate of SWCNHs (Fig. (4.4)) and production rate of H₂ in Fig. 4.6, their molar production rates seem to be comparable average. (The molar production rate of SWCNHs in carbon basis is derived by division of its mass production rate [g s⁻¹] by molar weight of carbon [12.01 g mol⁻¹].) From this comparison, mean molar concentration of carbon in the SWCNHs-producing zones including the quenching-zone and the downstream-zone can be considered as comparable.

4.2.3 Possible mechanism of SWCNHs formation

The possible mechanisms of SWCNHs formation and the effects of the water vapor have not yet been clarified even though the simplified model in the reaction field is established in this study. Nevertheless, we consider a hypothesis that SWCNHs may be formed from bubbled carbon droplets generated from carbon vapor. It should be noted that round shape of ordinal bubble is stable, but round shape of carbon bubble is not stable because the grapheme sheet can not be round without adding many defects. Instead, horn or tube shape can be stable, and thus quenched carbon bubbles may become agglomerated horn shape in self-assembling way. In this way, horns are formed from inside of carbon droplets by their boiling. On the other hand, water vapor may destroy the SWCNHs by encroaching the SWCNHs from outside of SWCNHs. Thus, the structure of SWCNHs may remain even if SWCNHs are decreased by the reaction of water vapor. However, it should be recognized that there is a limiting value of H₂O water concentration to preserve SWCNHs. If the water vapor concentration is excessively high as observed in the conventional AIW, SWCNHs can not be formed as mentioned above.

4.3 One-step synthesis of SWCNHs/Pd nanocomposite by GI-AIW method: Influence of Pd wire diameter

4.3.1 Characterization of SWCNHs/Pd nanocomposite

4.3.1.1 Transmission electron microscopic analysis

The morphology of SWCNHs/Pd nanocomposite which was synthesized in this research can be observed in TEM images (Fig. 4.14). These images show that the spherical Pd nanoparticles can be synthesized by our arc discharge

technique. Pd nanoparticles are also embedded inside SWCNHs aggregate. The SWCNHs aggregate particles have about 20-40 nm in diameter and have a bud like structure as same as our previous work [11, 12].

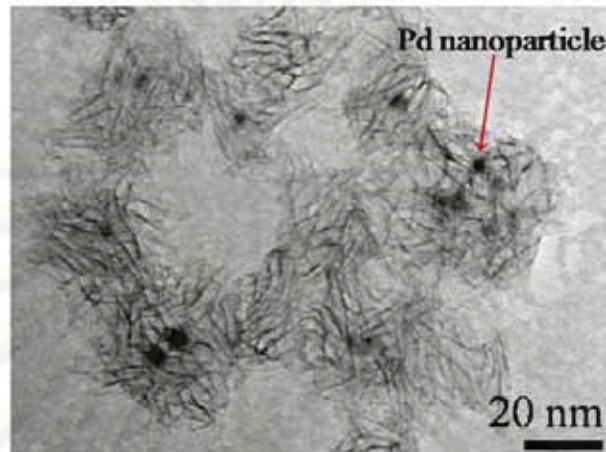


Figure 4.14 TEM image of SWCNHs/Pd nanocomposites.

4.3.1.2 Pd nanoparticles size distribution

We used TEM images for determining particle size of Pd nanoparticles which were synthesized from various diameters of Pd wires inside anode hole. Figure 4.15 shows TEM image of nanocomposites which was synthesized from different diameter of Pd wire together with their corresponding particles size distribution histograms. The distribution histograms are the discrete expression in particle size range of 3 nm and their density distribution which can be determined their average diameter of particles in each column of histogram by Eq. (4.17) [43].

$$\bar{D}_N = \sum \Delta n D_p / N \quad (4.17)$$

where Δn is the number of particles having diameter D_p and N is the total particle number (from our determination, $N = 500$).

Then we also used Eq. (4.17) for determining mean diameter of Pd nanoparticles by substituting the number and average size of particles in each column of histogram for Δn and D_p . From Fig. 4.15, the Pd nanoparticles which were synthesized from Pd wire of diameter 0.1 mm [Fig. 4.15(a)] and 0.3 mm [Fig. 4.15(b)] show similar average particle sizes of 6.9 nm, but the particle size distribution from 0.1 mm wire diameter is narrower than that from 0.3 mm. Moreover the TEM images of Pd nanoparticles from 0.1 and 0.3 mm Pd wire diameters show the presence of very small particles of approximately 3-6 nm in size, embedded in SWCNHs aggregates. Pd nanoparticles from 0.5 and 0.8 mm Pd wire diameter [Fig. 4.15(c) and 4.15(d)] exhibit clearly larger diameters, showing 8.6 and 9.4 nm in average size.

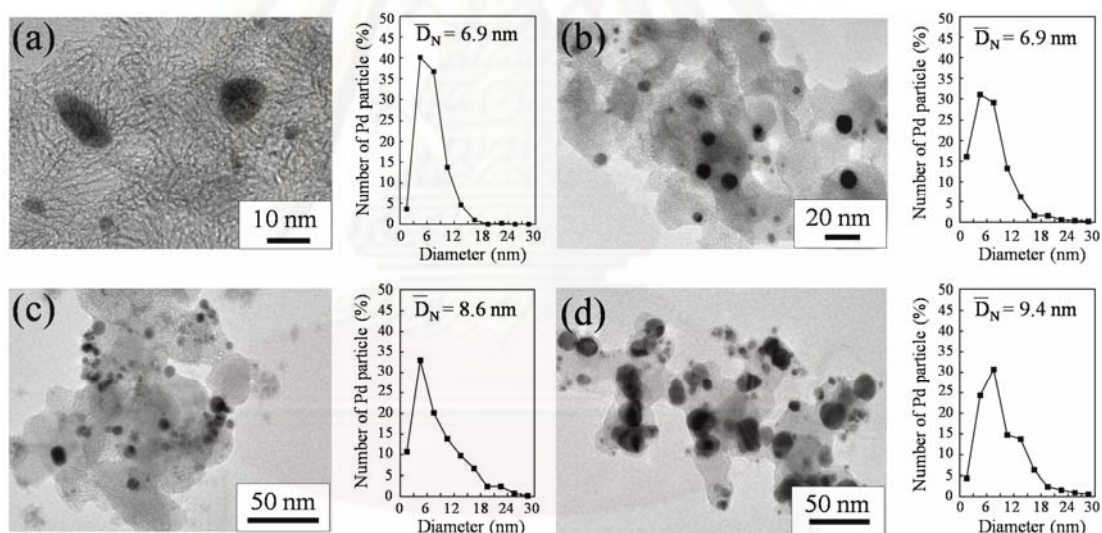


Figure 4.15 TEM images of SWCNHs/Pd and their corresponding Pd nanoparticles size distribution histograms which were synthesized by inserting Pd wire of (a) 0.1 mm, (b) 0.3 mm, (c) 0.5 mm and (d) 0.8 mm in diameter inside anode hole.

These results suggest that the size of Pd nanoparticles depends on the Pd wire diameter. It is noteworthy that the concentration of Pd cluster generated in arc zone

should be considered. When the anode was consumed in arc discharge, Pd wire was also consumed to form Pd vapor together with carbon vapor. With the high quenching rate of these vapors inside cathode hole at mega-K s^{-1} level [12] due to the large temperature difference between arc zone and water and rapid resident time (1.7×10^{-3} s, [12]) of these vapor inside the cathode hole, the carbon vapor can become a stable structure; SWCNHs. Meanwhile, Pd vapor also becomes stable structure as a spherical nanoparticle. In this situation, the concentration of Pd vapor affects the size of Pd nanoparticles. During carbon vapor and Pd vapor are generated, smaller Pd wire diameter leads to lower concentration of Pd vapor than larger Pd wire diameter, causing many small Pd particles typically ranging from 3 to 6 nm. Because of the geometric reason, the smaller Pd nanoparticles seem to be dispersed better than larger Pd nanoparticles. Meanwhile with the larger diameter of Pd wire, high concentration of Pd vapor are generated and they tend to form larger particles which can be observed in TEM image [Fig. 4.15(c) and 4.15(d)], and their size distribution are broad in large particle diameter range.

4.3.1.3 X-ray diffraction analysis

Figure 4.16 shows typical XRD pattern of SWCNHs without Pd nanoparticles and SWCNHs/Pd nanocomposite which floated on water surface during arc discharge at various Pd wire diameter. Diffraction peaks of both SWCNHs and Pd can be observed. It can be seen that SWCNHs were highly graphitized carbon materials for the diffraction peaks at 24.5° and the pattern of Pd metal are indicated for (111), (200) and (220) diffraction peaks at 40° , 47° and 69° , respectively. Through the peak, the carbide form Pd is not observed in these spectra. From the peak (111) are clearly recognized and they are rather sharp which can be used to estimate the

crystalline size of Pd metal by using the Debye-Scherrer method [49]. The calculated crystalline size of Pd metal are 5.0, 6.0, 4.9 and 6.7 nm which using the peak (111) of the pattern (a) 0.1 mm, (b) 0.3 mm, (c) 0.5 mm and (d) 0.8 mm Pd wire diameter respectively. It can be claimed that the crystal structure of Pd nanoparticles do not depend on the Pd wire diameter.

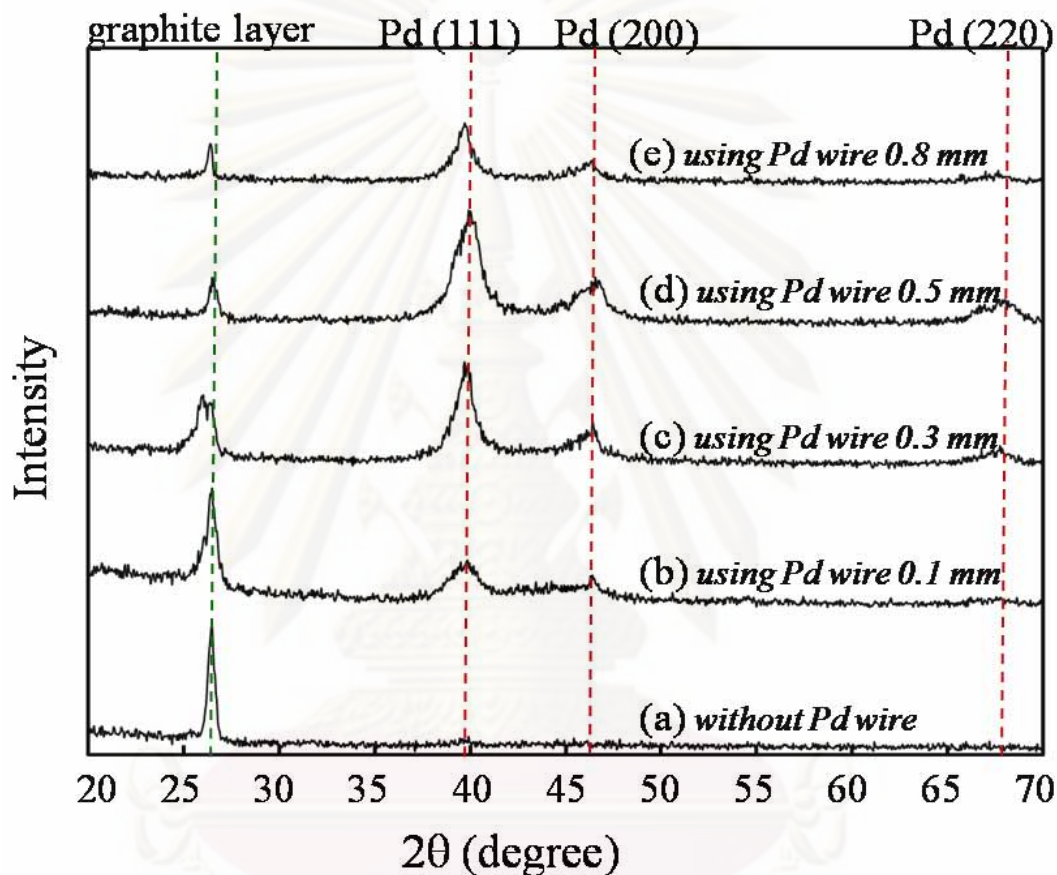


Figure 4.16 XRD pattern of SWCNHs/Pd which were synthesized by arc discharge (a) SWCNHs without Pd nanoparticle, (b) SWCNHs/Pd nanocomposite by inserting Pd wire diameter 0.1 mm, (c) 0.3 mm, (d) 0.5 mm and (e) 0.8 mm, respectively.

4.3.1.4 Raman spectroscopic analysis

In addition the crystallinity of SWCNHs in the composite is characterized by Raman spectroscopy. Fig. 4.17 shows the intensity ratio of

G-band (Raman shift at 1580 cm^{-1}) over D-band (Raman shift at 1330 cm^{-1}) in Raman spectra as a function of Pd wire diameter compare with G/D ratio of as-grown SWCNHs which were synthesized at the same condition but Pd wire was not inserted in anode hole. The G/D ratios of SWCNHs/Pd nanocomposite are slightly higher than that of as-grown SWCNHs. In general when G/D ratio is higher, the concentration of crystalline carbon nanostructures would become higher. In our case, the higher G/D ratio is caused by graphitic carbon which contained in SWCNHs/Pd nanocomposite. We will mention about the composition characterization of carbon structure in SWCNHs later by thermogravimetric analysis. Anyway, based on our Raman characterization, it can be said that Pd wire diameter did not have an effect on the purity of SWCNHs. This tendency is also consistent with the result obtained by the thermogravimetric analysis.

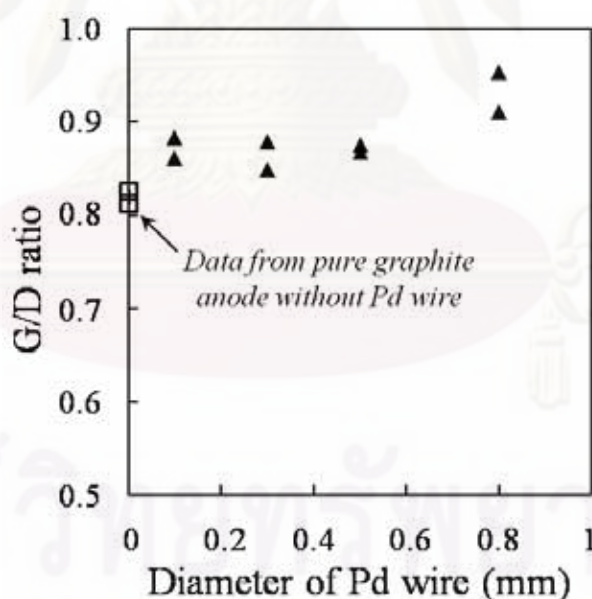


Figure 4.17 The intensity ratio of G-band over D-band (G/D) in Raman spectra as a function of Pd wire diameter.

4.3.1.5 Thermogravimetric analysis

The composition of SWCNHs in the composite can be provided by using thermogravimetric (TG) analysis. In TG analysis, the SWCNHs/Pd nanocomposites were heated at constant rate ($10^{\circ}\text{C min}^{-1}$) in the furnace. The temperature which was used for burning-off the composite is reaching up to 900°C . Then the weight loss of the sample was measured with increasing of temperature. The typical TG curve is show in Fig. 4.18. From the TG curve, the onset temperature of weight loss of SWCNHs was about 300°C . When SWCNHs and Pd nanoparticles were shaped into composite SWCNHs/Pd, the onset temperature of weight loss in air remained at about the same temperature as that of the parent SWCNHs.

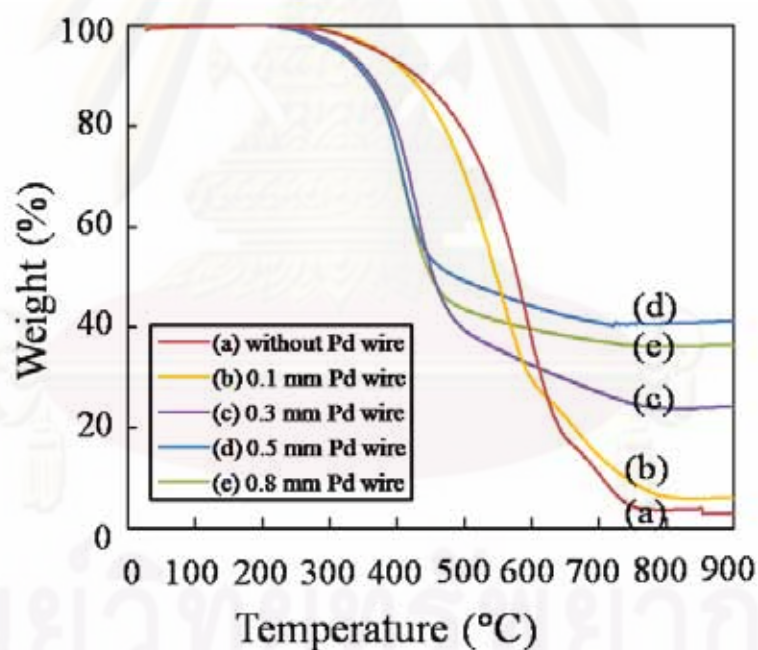


Figure 4.18 Weight loss versus temperature of as-grown SWCNHs and SWCNHs/Pd with varied size of Pd wire in anode hole.

We can also determine the differential weight in each temperature and plot in Fig. 4.19, which is differential thermal analysis (DTA). It is

found that the DTA chart of as-grown SWCNHs consists of three exothermic peaks. These peaks are denoted as peak 1-3 for the order of temperature elevation. All DTA exothermic peaks stem from the combustion of carbon having different structures.

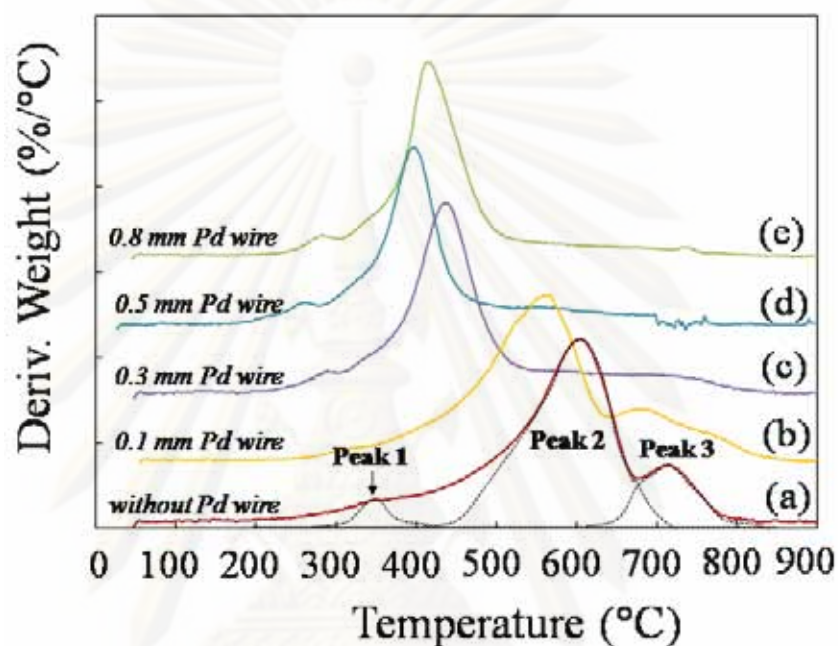


Figure 4.19 Derivative weight loss versus temperature of as-grown SWCNHs and SWCNHs/Pd with varied size of Pd wire in anode hole.

Utsumi et al. [50] assume that peaks 1, 2 and 3 were assigned to the combustion peak of amorphous carbon, tubular graphene carbon, and graphitic carbon in the SWCNHs aggregates, respectively. Here, “amorphous carbon” must be amorphous carbon nanoparticles produced under arc discharge, which have started burning-off at 300°C. With increase in the Pd wire diameter, the smallest peak 1 slightly increases. “Tubular graphene carbon” is the main tubular part of SWCNHs particles, showing the strongest combustion DTA peak about 600°C for as-grown SWCNHs. From fig. 4.19, the DTA peaks of SWCNHs/Pd nanocomposites which

were synthesized by inserting Pd wire of 0.1, 0.3, 0.5 and 0.8 mm. diameters respectively indicate that decomposed temperature of SWCNHs/Pd nanocomposites was lower by increasing of Pd wire. In addition, DTA peak values of SWCNHs/Pd nanocomposites which were synthesized by using Pd wire diameter of 0.3, 0.5 and 0.8 mm. were higher than that of as-grown SWCNHs, whereas peak width of SWCNHs/Pd nanocomposites were narrower than that of as-grown SWCNHs, showing that SWCNHs/Pd nanocomposites combustion was more compact and acute than as-grown SWCNHs. These results showed that Pd nanoparticles which dispersed in SWCNHs aggregates significantly influence the decomposed temperature of SWCNHs/Pd nanocomposites. The last peak is “Graphitic carbon” indicated very thin layered-graphite composed of aggregates of SWCNHs. In our composite, it is possible that the peak 3 is the carbon nanocapsules (CNCs) [51] which wrapped Pd nanoparticles. Anyway, Pd nanoparticles can have catalytic effect to burn carbon part in TG analysis, resulting the decomposed temperature of SWCNHs/Pd nanocomposite is lower than that of as-grown SWCNHs.

Regarding to TG analysis, after the temperature was increased to 900°C, the as-grown SWCNHs would almost completely be burned off. However, SWCNHs/Pd nanocomposite would exhibit different thermal behavior because the Pd metal was not burned off at this temperature. In general, Pd metal has melting temperature at 1554.9°C. Therefore, there were the Pd metal remained in the composite. We can confirm that Pd was not oxidized after burn by checking with XRD analysis. It clearly shows the peak of (111), (200) and (220). After the complete burning-off of SWCNHs, the remaining weight of Pd metal should be related with the amount of Pd vapor in arc zone which depended on Pd wire diameter.

4.3.2 Yield of SWCNHs and Pd nanoparticles

As mention previously, the weight of Pd in Pd-dispersed SWCNHs was measured by a thermogravimetric analysis so that the percentage of Pd weight in the nanocomposites can be determined and plotted in Fig. 4.20.

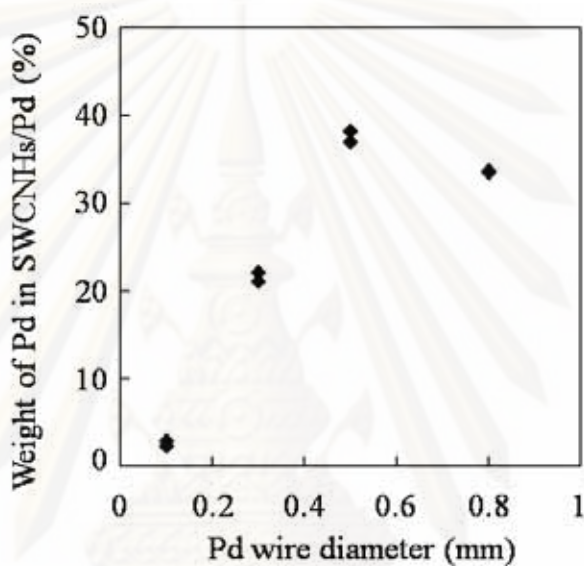


Figure 4.20 Weight of Pd in SWCNHs/Pd as a function of Pd wire diameter.

This figure shows a tendency that the weight of Pd nanoparticles in the SWCNHs/Pd nanocomposites increases with the Pd wire diameter due to the increasing of mass of Pd wire in the synthesis system. The weight of SWCNHs in the composite was also determined. Thus the yield of Pd nanoparticle and SWCNHs can be determined from Eq. (4.18) and Eq. (4.19), respectively. The yield of each component in the nanocomposite was determined and plotted in Fig. 4.21.

$$\%Yield\ of\ Pd = \frac{Total\ weight\ remained\ of\ Pd\ in\ the\ nanocomposite}{Consumed\ weight\ of\ Pd\ wire} \times 100 \quad (4.18)$$

$$\% \text{Yield of SWCNHs} = \frac{\text{Total weight of nanocomposite} - \text{Total weight of Pd}}{\text{Consumed weight of graphite anode}} \times 100 \quad (4.19)$$

Yield of Pd nanoparticles have relatively high when 0.1 and 0.3 mm Pd wire were used and the yield is decreased with larger diameter. Meanwhile the yield of SWCNHs is almost same. In a way, at the arc zone Pd wire are vaporized to form Pd vapor and then becomes Pd nanoparticles by high quenching rate in cathode hole.

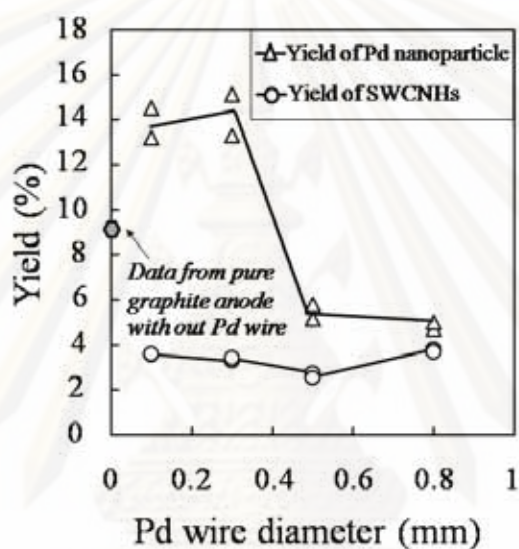


Figure 4.21 Yield of SWCNHs and Pd nanoparticles as a function of Pd wire diameter.

Pd nanoparticles with diameter in a range of 3-9 nm can be hybridized with SWCNHs and escapes outside cathode hole with N_2 gas by buoyancy force. But the Pd particles which have higher density would not go through cathode hole with N_2 gas because we can observe Pd nanoparticles with significantly large diameter in the cathode deposit from TEM image in Fig. 4.22. Moreover when Pd wire diameter of 0.5 and 0.8 mm. was used, the Pd nanoparticles diameter tends to be increased. Thus the large particles of Pd highly remained in cathode deposit. Therefore the yield of Pd nanoparticles

hybridized with SWCNHs was dramatically decreased. This could be attributed that the formation of Pd nanoparticles from Pd vapor are affected by Pd wire diameter. On the other hand, the formation of SWCNHs should be hardly affected by the Pd wire diameter because the size of anode graphite is constant.

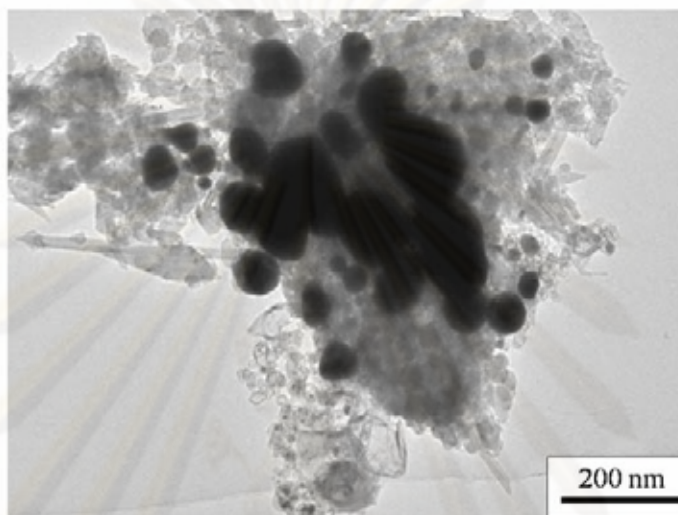


Figure 4.22 Typical TEM image of Pd nanoparticles in cathode deposit.

4.3.3 Surface area of SWCNHs/Pd nanocomposite

4.3.3.1 BET specific surface area

The structure of SWCNHs/Pd nanocomposite can be characterized by BET specific surface area (SSA) which is shown in Fig. 4.23. The BET specific surface areas are evaluated from N_2 adsorption on SWCNHs and Pd nanoparticles which are not migrated in carbonaceous parts. Thus, the total exposed surface area of SWCNHs/Pd can be shown by BET surface area. In addition, if we subtract the Pd exposed specific surface area (describe in section 4.3.3.2) from the total BET specific surface area, the specific surface area of carbonaceous part (base on unit mass of SWCNHs/Pd nanocomposites) can be obtained. To determine the specific surface area of carbonaceous part per mass of carbonaceous part which is

shown in Fig. 4.23, the surface area of carbonaceous per mass of nanocomposites should be multiplied by the ratio of mass of nanocomposites over mass of carbonaceous part.

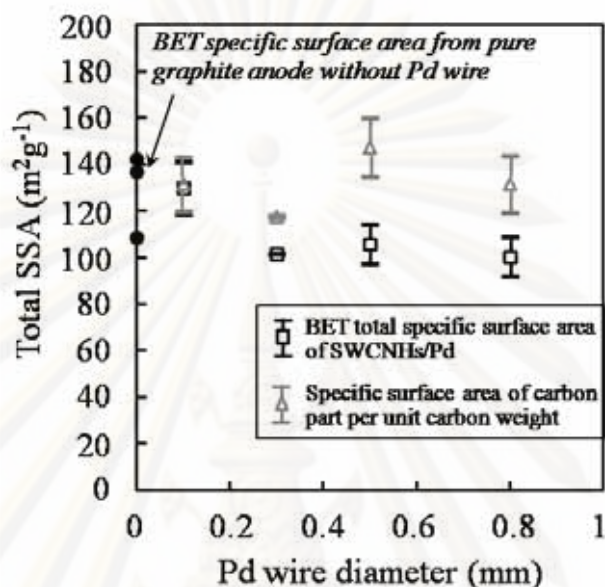


Figure 4.23 BET specific surface area of SWCNHs/Pd and specific surface area of carbonaceous part as a function of Pd wire diameter.

From this figure, it can be seen that the SWCNHs specific surface area is not depended on Pd wire diameter. The SWCNHs surface area still has the range of surface area as same as that of as-grown SWCNHs. Moreover, it seems likely that the specific area of SWCNHs/Pd nanocomposite dominantly depends on the surface area of SWCNHs. Because the SWCNHs/Pd surface area is not different from surface area of only-SWCNHs part, especially when Pd wire diameter at 0.1-0.3 mm.

4.3.3.2 Pd nanoparticle exposed surface area

The specific surface area of only Pd nanoparticles which expose outside SWCNHs matrix, Pd-S_{expo}, which is shown in Fig. 4.24 can be

measured by CO chemisorption. Because the metal Pd is active for chemical adsorption of CO [36,37]. Thus the exposed surface area of Pd can be estimated if the saturated amount of CO adsorbed on Pd is measured. For this measurement, a known amount of CO was supplied to the powder-bed of SWCNHs/Pd nanocomposites in pulsed-way with a carrier gas, He, at a constant flow rate, and CO concentration was monitored in downstream to confirm the saturation and to measure the adsorbed amount of CO. Finally we can determine the specific surface area of metal Pd exposed outside SWCNHs matrix.

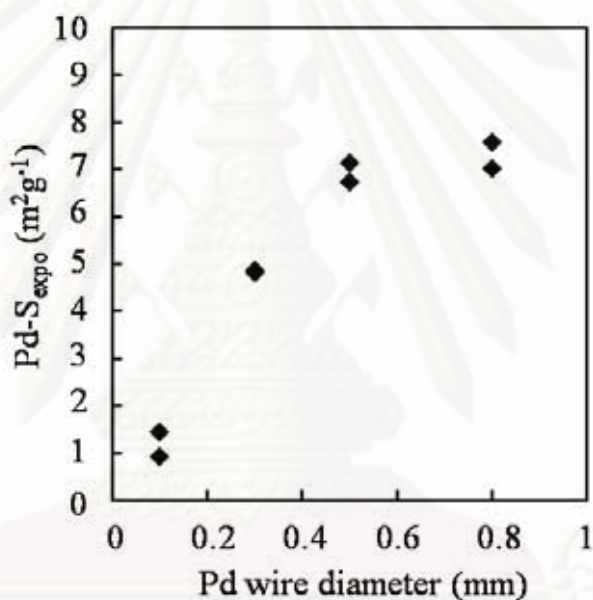


Figure 4.24 Pd nanoparticle exposed specific surface area as a function of Pd wire diameter.

The Pd exposed surface area as the active metal area is depended on Pd wire diameter as shown in Fig. 4.24. The exposed area of Pd nanoparticles drastically increases with increasing of Pd wire diameter. This trend agrees with change of diameter of particles in size distribution analysis described previously. When the Pd nanoparticles get larger diameter, they tend to expose outside the SWCNHs aggregate. Because larger size of Pd wire diameter makes the

high concentration of Pd vapor so the larger diameter of Pd nanoparticles can be formed with higher weight remained in the composite. Obviously, the larger size diameter of Pd nanoparticles tends to be exposed outside the SWCNHs matrix.

In additional, we estimated the percentage of the exposed surface area of Pd particles in total Pd surface, P from Eq. (4.20). For this estimation, the surface area of Pd particles (not only exposed surface but also migrated surface) per unit mass of Pd, S_T , is calculated from the average Pd particle size by Eq. (4.21)

$$P = (Pd \cdot S_{\text{expo}} / S_T) \times 100 \quad (4.20)$$

$$S_T = (4\pi r_a^2) / [(4/3)\pi r_a^3 \cdot \rho] \quad (4.21)$$

where ρ and r_a are the density of metal Pd (= 12.02 g cm⁻³ at room temperature) and the average Pd nanoparticle radius calculated from the values in Fig. 4.15.

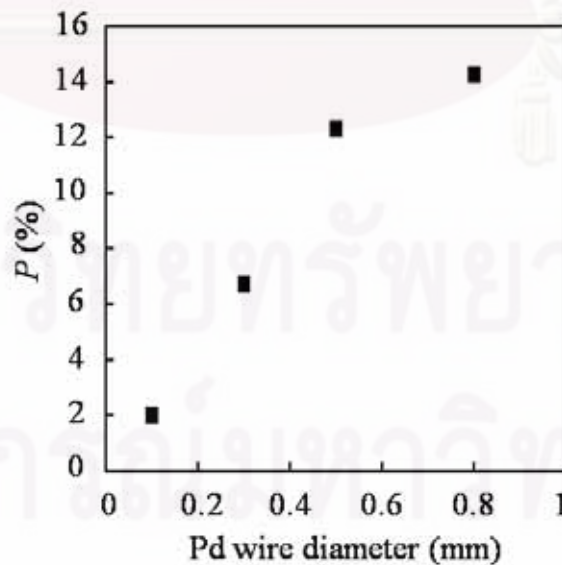


Figure 4.25 Percentage of exposed surface area of Pd nanoparticle outside SWCNHs aggregate as a function of Pd wire diameter.

The result of calculation is shown in Fig. 4.25. From this figure, it clearly shows that most of Pd nanoparticles are migrated in SWCNHs aggregates, especially when narrow Pd wire was used. On the other hand P is reaching approximately 14% when larger Pd wire was used. It can be said that by increasing the Pd wire diameter, the diameter of Pd nanoparticle tends to be increased and exposed outside SWCNHs aggregate.



ศูนย์วิจัยทรัพยากร
จุฬาลงกรณ์มหาวิทยาลัย

CHAPTER V

CONCLUSIONS AND RECOMMENDATIONS

5.1 Conclusions

Based on our experimental investigation, the influence of the water temperature on the synthesis of SWCNHs by GI-AIW by the analyses of morphology of SWCNHs, SWCNHs production, byproduct-gas production and the optical spectra emitted from the arc plasma have been better understood. The simplified model of relevant reaction mechanism was proposed by taking into account the diffusion of water vapor in cathode hole in the GI-AIW system. It was observed that the yield and production rate of SWCNHs was significantly decreased with the increase in water temperature although the purity of as-grown SWCNHs was independent of the water temperature. These experimental results are ascribed to the reaction between carbon vapor and water vapor in a zone around the interface between the so-called quenching zone and the downstream zone inside the cathode hole. By comparison with experimental data, the proposed model can acceptably correlate the relationship between H₂ gas production and water temperature, which can affect the SWCNHs formation.

Additionally, in this work SWCNHs hybridized with Pd nanoparticles could be synthesized by using Pd wire which was inserted inside anode hole and subject to

GI-AIW method. The composite of Pd nanoparticles embedded in SWCNHs matrix successfully synthesized by this method could be verified by our microscopic analyses. The SWCNHs/Pd nanocomposite was characterized by XRD, TEM, BET, TG-DTA analysis and CO chemisorption. By changing the Pd wire diameter, it is possible to control the concentration of Pd vapor at arc zone. Hence large amount Pd nanoparticle can be formed and have large diameter when wide Pd wire was used. From the characterization result, it is confirmed that Pd nanoparticles tend to get larger diameter and expose outside SWCNHs aggregate with increasing of Pd wire diameter. The average diameter of Pd nanoparticles which were embedded inside SWCNHs matrix is 3-6 nm in range. Meanwhile the formation and structure of SWCNHs are not depended on Pd wire diameter.

5.2 Recommendations

To improve the simplified model which was proposed here, one may need to consider the mass balance of carbon vapor and H₂O in each reaction zone. For this consideration, the concentration profile of carbon vapor should be discussed.

The study of SWCNHs/Pd nanocomposite for H₂ gas detection should be further investigated.

REFERENCES

- [1] Kroto, H.W., Heath, J.R., O'Brien, S.C., Curl, R.F., and Smalley, R.E. C₆₀: Buckminsterfullerene. Nature 318 (November 1985): 162-163.
- [2] Iijima, S. Helical microtubules of graphitic carbon. Nature 354 (November 1991): 56-58.
- [3] Kroto, H.W. Carbon onions introduce new flavour to Fullerene studies. Nature 359 (October 1992): 670-671.
- [4] Iijima, S., Yudasaka, M., Yamada, R., Bandow, S., Suenaga, K., Kokai, F., and Takahashi, K. Nano-aggregates of single-walled graphitic carbon nano-horns. Chemical Physics Letters 309 (August 1999): 165-170.
- [5] Bandow, S., Kokai, F., Takahashi, K., Yudasaka, M., Qin, L.C., and Iijima, S. Interlayer spacing anomaly of single-wall carbon nanohorn aggregate. Chemical Physics Letters 321 (May 2000): 514-519.
- [6] Itoh, T., Urita, K., E. Bekyarova, Arai, M., Yudasaka, M., Iijima, S., Ohba, T., Kaneko, K., and Kanoh, H. Nanoporosities and catalytic activities of Pd-tailored single wall carbon nanohorns. Journal of Colloid and Interface Science 322 (2008): 209-214.
- [7] Suehiro, J., Sano, N., Zhou, G., Imakiire, H., Imasaka, K., and Hara, M. Application of dielectrophoresis to fabrication of carbon nanohorn gas sensor. Journal of Electrostatics 64 (2006): 408-415.
- [8] Ohba, T., Murata, K., Kaneko, K., Steele, W.A., Kokai, F., Takahashi, K., Kasuya, D., Yudasaka, M., and Iijima, S. N₂ adsorption in an internal nanopore space of single-walled carbon nanohorn: GCMC simulation and experiment. Nano Letters 1, 7 (2001): 371-373.
- [9] Xu, J., Yudasaka, M., Kouraba, S., Sekido, M., Yamamoto, Y., and Iijima, S. Single wall carbon nanohorn as a drug carrier for controlled release. Chemical Physics Letters 461 (2008): 189-192.
- [10] Sano, N., Nakano, J., and Kanki, T. Synthesis of single-walled carbon nanotubes with nanohorns by arc in liquid nitrogen. Carbon 42 (2004): 686-688.

- [11] Sano, N. Low-cost synthesis of single-walled carbon nanohorns using the arc in water method with gas injection. Journal of Physics D: Applied Physics 37 (2004): L17-L20.
- [12] Sano, N., Kimura, Y., and Suzuki, T. Synthesis of carbon nanohorns by a gas-injected arc-in-water method and application to catalyst-support for polymer electrolyte fuel cell electrodes. Journal of Materials Chemistry 18 (2008): 1555-1560.
- [13] Takikawa, H., Ikeda, M., Hirahara, K., Hibi, Y., Tao, Y., Ruiz, P.A., Jr., Sakakibara, T., Itoh, S., and Iijima, S. Fabrication of single-walled carbon nanotubes and nanohorns by means of a torch arc in open air. Physica B 323 (2002): 277-279.
- [14] Ikeda, M., Takikawa, H., Tahara, T., Fujimura, Y., Kato, M., Tanaka, K., Itoh, S., and Sakakibara, T. Preparation of carbon nanohorn aggregates by cavity arc jet in open air. The Japan Society of Applied Physics 41 (2002): L852-L854.
- [15] Guerret-Plecourt, C., Le Bouar, Y., Lolseau, A., and Pascard, H. Relation between metal electronic structure and morphology of metal compounds inside carbon nanotubes. Nature 372 (1994): 761-764.
- [16] Bera, D., Kuiry, S., C., McCutchen, M., Seal, S., Heinrich, H., and Slane, G., C. In situ synthesis of carbon nanotubes decorated with palladium nanoparticles using arc-discharge in solution method. Journal of Applied Physics 96,9 (November 2004): 5152-5157.
- [17] Karousis, N., Tsotsou, G.E., Evangelista, F., Rudolf, P., Ragoussis, N., and Tagmatarchis, N. Carbon nanotubes decorated with palladium nanoparticles: Synthesis, characterization, and catalytic activity. J. Phys. Chem. C 112 (2008): 13463-13469.
- [18] Sun, Y., and Hau Wang, H. High-performance, flexible hydrogen sensors that use carbon nanotubes Decorated with Palladium Nanoparticles. Advanced Materials 19 (2007): 2818-2823.
- [19] Tribolet, P., and Kiwi-Minsker, L. Palladium on carbon nanofibers grown on metallic filters as novel structured catalyst. Catalysis Today 105 (2005): 337-343.

- [20] Litran, R., Sampedro, B., Rojas, T.C., Multigner, M., Sanchez-Lopez, J.C., Crespo, P., Lopez-Cartes, C., Garcia, M.A., Hernando, A., and Fernandez, A. Magnetic and microstructural analysis of palladium nanoparticles with different capping systems. Physical Review B 73 (2006): 054404-1-054404-7.
- [21] Li, Y., Wang, H., Chen, Y., and Yang, M. A multi-walled carbon nanotube/palladium nanocomposite prepared by a facile method for the detection of methane at room temperature. Sensors and Actuators B 132 (2008): 155-158.
- [22] Sano, N., Wang, H., Chhowalla, M., Alexandrou, I., and Amaratunga, G. A., J. Synthesis of carbon 'onions' in water. Nature 414 (November 2001): 506-507.
- [23] Sano, N., Charinpanitkul, T., Kanki, T., and Tanthapanichakoon, W. Controlled synthesis of carbon nanoparticles by arc in water method with forced convective jet. Journal of Applied Physics 96, 1 (July 2004): 645-649.
- [24] Zhu, H.W., Li, X.S., Jiang, B., Xu, C.L., Zhu, Y.F., Wu, D. H., and Chen, X.H. Formation of carbon nanotubes in water by the electric-arc technique. Chemical Physics Letters 366 (2002): 664-669.
- [25] NanoPrint Technologies. Nanotechnology. [Online] Available from: http://www.nanoprinttech.com/nano_info.html [2010, January].
- [26] Tenne, R. Inorganic nanotubes and fullerene-like nanoparticles. Nature Nanotechnology 1 (2006) [Online] Available from: <http://www.nature.com/nnano/journal/v1/n2/full/nnano.2006.62.html> [2009, August].
- [27] Phattarapongsant, E. Synthesis of carbon nanoparticles by arc discharge in liquid using metallic cathode and their applications as a filler for polymer nanocomposite. Master degree Thesis Submission. Department of Chemical Engineering Faculty of Engineering Chulalongkorn University, 2005.
- [28] Ishiguro, K. Interview report of Iijima, S. Nanotube and nanohorn-Future real key player of nanotechnology. Japan Nonotech Bulletin: Nanonet Interview : 1-2.23rd Issue (22 July, 2004)
- [29] Harris, P., J.F. Carbon nanotubes and related structures : New materials for the 21st century. 1st ed. United Kingdom: Cambridge University Press, 1999.
- [30] Davies, A.C. The science and practice of welding. 7th ed. United Kingdom: Cambridge University Press, 1977.

- [31] O'Connell, M. Carbon nanotubes : properties and applications. United States of America: CRC Press Taylor & Francis Group, 2006.
- [32] Jackson, K.G. Dictionary of Electrical Engineering. 1st ed. London: Butterworth & Co. Ltd., 1965.
- [33] Sano, N., Wang, H., Alexandrou, I., Chhowalla, M., Teo, K.B.K., Amaratunga, G.A.J., and Iimura, K. Properties of carbon onions produced by an arc discharge in water. Journal of Applied Physics 92, 5 (2002): 2783-2788.
- [34] De Heer, W.A., Pocharal, P., Berger, C., Gezo, J., Song, Z., Bettini, J., and Ugarte, D. Liquid carbon, carbon-glass beads, and the crystallization of carbon nanotubes. Science 307 (February 2005): 907-910.
- [35] Harris, P., J.F. Solid state growth mechanisms for carbon nanotubes. Carbon 45 (2007): 229-239.
- [36] Boronin, A.I., Slavinskaya, E.M., Danilova, I.G., Gulyaev, R.V., Amosov, Yu.I., Kuznetsov, P.A., Polukhina, I.A., Koscheev, S.V., Zaikovskii, V.I., and Noskov, A.S. Investigation of palladium interaction with cerium oxide and its state in catalysts for low-temperature CO oxidation. Catalysis Today 144 (2009): 201-211.
- [37] Agostini, G., Pellegrini, R., Leofanti, G., Bertineti, L., Bertarione, S., Groppo E., Zecchina, A., and Lamberti, C. Determination of the particle size, available surface area, and nature of exposed sites for silica-alumina-supported Pd nanoparticles: A multitechnical approach. J. Phys. Chem. C 113 (2009): 10485-10492.
- [38] Yamaguchi, T., Bandow, S., and Iijima, S. Synthesis of carbon nanohorn particles by simple pulsed arc discharge ignited between pre-heated carbon rods. Chemica Physics Letters 389 (2004): 181-185.
- [39] Wang, H., Chhowalla, M., Sano, N., Jia, S., and Amaratunga, G.A.J. Large-scale synthesis of single-walled carbon nanohorns by submerged arc. Nanotechnology 15, 5 (May 2004): 546-550.
- [40] Muthakarn, P., Sano, N., Charinpanitkul, T., Tanthapanichakoon, W., and Kanki, T. J. Phys. Chem. B. 110 (2006): 18299-18306.
- [41] Baravian, G., Chouan, Y., Ricard, A., and Sultan, G. Doppler-broadened H α line shapes in a rf low-pressure H $_2$ discharge. Journal of Applied Physics 61, 12 (June 1987): 5249-5253.

- [42] Eguchi, W. Kagaku Kogaku Ryoron, Stoichiometry in Chemical Engineering. 2nd ed. Tokyo: Kagakudojin, 1988 (pp.318-319).
- [43] Kousaka, Y., and Endo, Y. Particle size. In: Gotoh, K., Masuda, H., Higashitani, K, (eds.), Powder technology handbook, pp. 3-8. New York: Marcel Dekker, 1997.
- [44] Laurent, Ch., and Peigney, A. Carbon nanotubes in composite materials. In: Nalwa, H.S. (ed.), Encyclopedia of nanoscience and nanotechnology, pp. 637-638. New York: American Scientific Publishers, 2004.
- [45] Teo, K, B.K., Singh, C., Chhowalla, M., and Milne, W.I. Catalytic synthesis of carbon nanotubes and nanofibers. In: Nalwa, H.S. (ed.), Encyclopedia of nanoscience and nanotechnology, pp. 672-675. New York: American Scientific Publishers, 2004.
- [46] Bera, D., Kuiry, S.C., McCutchen, M., Kruize, A., Heinrich, H., Meyyappan, M., and Seal, S. In-situ synthesis of palladium nanoparticles-filled carbon nanotubes using arc-discharge in solution. Chemical Physics Letters, 386 (2004): 364-368.
- [47] Charinpanitkul, T., Tanthapanichakoon, W., and Sano, N. Carbon nanostructures synthesized by arc discharge between carbon and iron electrodes in liquid nitrogen. Current Applied Physics, 9 (2009): 629-632.
- [48] Charinpanitkul, T., Soottitantawat, A., Tonanon, N., and Tanthapanichakoon, W. Single-step synthesis of nanocomposite of copper and carbon nanoparticles using arc discharge in liquid nitrogen. Materials Chemistry and Physics, 116 (2009): 125-128.
- [49] Hall, B. D., Zanchet, D.Z., and Ugarte, D.U. Estimating nanoparticle size for diffraction measurements. Journal of Applied Crystallography, 33 (2000): 1335-1341.
- [50] Utsumi, S., Miyawaki, J., Tanaka, H., Hattori, Y., Itoi, T., Ichikuni, N., Kanoh, H., Yudasaka, M., Iijima, S., and Kaneko, K. Opening mechanism of internal nanoporosity of single wall carbon nanohorn. J. Phys. Chem. B, 109 (2005): 14319-14324.

[51] Sano, N., Kikuchi, T., Wang, H., Chhowalla, M., Amaratunga, G. A.J.

Carbon nanohorns hybridized with the metal-included nanocapsule. Carbon,
42 (2004): 95-99.



ศูนย์วิทยทรัพยากร
จุฬาลงกรณ์มหาวิทยาลัย

APPENDIX A

EXPERIMENTAL DATA FOR SWCNHs SYNTHESIS

Data sheet of experiment on SWCNHs synthesis by GI-AIW method by varying water temperature is shown in appendix A. The data sheet is used for plotting yield and production rate of SWCNHs in Fig 4.4 and H₂ production rate in Fig. 4.6.

The data sheet which is shown in this section can be catalogued in four groups of water temperature as following:

Group 1: range of temperature 1-2°C is shown in Table A.1- A.3

Group 2: range of temperature 19-24°C is shown in Table A.4- A.7

Group 3: range of temperature 46-62°C is shown in Table A.8- A.14

Group 4: range of temperature 79-83°C is shown in Table A.15- A.17

Table A.1 Data sheet of experiment on SWCNHs synthesis at 1.3°C

Data Sheet for Batch NO.35 (13 Nov, 08)			
Constant variable			
Arc current	80 A		
Arc time	15 sec		
N ₂ gas flow rate	5 L/min		
Anode ascending velocity	1.5 mm/s		
Cathode			
Weight before arc	7.1594 g		
Weight after arc	7.3892 g		
Length before arc	49.1 mm		
Length after arc	49.1 mm		
Anode			
Weight before arc	0.9277 g		
Weight after arc	0.6087 g		
Consumed weight	0.3190 g		
Length before arc	74.0 mm		
Length after arc	49.0 mm		
Loss of length	25.0 mm		
Independent variable			
Temperature of water before arc	1.3 °C		
Temperature of water after arc	8 °C		
Volume of water before arc	1,000 ml		
Volume of water that was loosed during arc process	30 ml		
Volume of sample gas	7.0 ml		
Dependent variable: weight measurement			
Weight of CNHs floating on water surface	0.0281 g		
Weight of product inside cathode hole	0.2266 g		
$\% \text{ Yield} = \frac{\text{wt. of CNHs floating on water surface}}{\text{Consumed weight of anode}}$			8.81%
Dependent variable: Gas chromatography analysis			
	Retention time (min)	Curve area	Concentration (ppm)
H ₂ gas analysis	0.845	63110	4637.03
	0.832	63555	4669.73
	0.849	63920	4696.55
CO gas analysis			
Comment:			

Table A.2 Data sheet of experiment on SWCNHs synthesis at 2°C

Data Sheet for Batch NO.36 (13 Nov, 08)			
Constant variable			
Arc current	80 A		
Arc time	15 sec		
N ₂ gas flow rate	5 L/min		
Anode ascending velocity	1.5 mm/s		
Cathode			
Weight before arc	7.0031 g		
Weight after arc	7.2679 g		
Length before arc	49.9 mm		
Length after arc	49.9 mm		
Anode			
Weight before arc	0.9324 g		
Weight after arc	0.5972 g		
Consumed weight	0.3352 g		
Length before arc	74.4 mm		
Length after arc	49.0 mm		
Loss of length	25.4 mm		
Independent variable			
Temperature of water before arc	2 °C		
Temperature of water after arc	9.2 °C		
Volume of water before arc	1,000 ml		
Volume of water that loosed during arc process	30 ml		
Volume of sample gas	7.0 ml		
Dependent variable: weight measurement			
Weight of CNHs floating on water surface	0.0185 g		
Weight of product inside cathode hole	0.2592 g		
% Yield = $\frac{\text{wt. of CNHs floating on water surface}}{\text{Consumed weight of anode}}$	5.52%		
Dependent variable: Gas chromatography analysis			
	Retention time (min)	Curve area	Concentration (ppm)
H ₂ gas analysis	0.839	70781	5200.66
	0.845	72563	5331.59
	0.832	70073	5148.64
CO gas analysis			
Comment:			

Table A.3 Data sheet of experiment on SWCNHs synthesis at 2.5°C

Data Sheet for Batch NO.29 (5 Nov, 08)			
Constant variable			
Arc current	80 A		
Arc time	20 sec		
N ₂ gas flow rate	5 L/min		
Anode ascending velocity	1.0 mm/s		
Cathode			
Weight before arc	7.1726 g		
Weight after arc	7.3543 g		
Length before arc	49.5 mm		
Length after arc	49.5 mm		
Anode			
Weight before arc	0.9422 g		
Weight after arc	0.6933 g		
Consumed weight	0.2489 g		
Length before arc	75.2 mm		
Length after arc	53.1 mm		
Loss of length	22.1 mm		
Independent variable			
Temperature of water before arc	2.5 °C		
Temperature of water after arc	8.0 °C		
Volume of water before arc	1,000 ml		
Volume of water that loosed during arc process	11 ml		
Volume of sample gas	6.0 ml		
Dependent variable: weight measurement			
Weight of CNHs floating on water surface	0.0129 g		
Weight of product inside cathode hole	0.1820 g		
% Yield = $\frac{\text{wt. of CNHs floating on water surface}}{\text{Consumed weight of anode}}$	5.18%		
Dependent variable: Gas chromatography analysis			
	Retention time (min)	Curve area	Concentration (ppm)
H ₂ gas analysis	0.829	28453	2090.60
	0.822	28422	2088.32
	0.819	28387	2085.74
CO gas analysis Sample gas 0.4 ml per one batch	4.762	1783	
	4.726	1673	
	4.739	1602	
Comment:			
Step arc occurred			

Table A.4 Data sheet of experiment on SWCNHs synthesis at 19.5°C

Data Sheet for Batch NO.28 (5 Nov, 08)			
Constant variable			
Arc current	80 A		
Arc time	20 sec		
N ₂ gas flow rate	5 L/min		
Anode ascending velocity	1.0 mm/s		
Cathode			
Weight before arc	7.0519 g		
Weight after arc	7.3227 g		
Length before arc	49.9 mm		
Length after arc	49.9 mm		
Anode			
Weight before arc	0.9308 g		
Weight after arc	0.5899 g		
Consumed weight	0.3409 g		
Length before arc	74.4 mm		
Length after arc	44.8 mm		
Loss of length	29.6 mm		
Independent variable			
Temperature of water before arc	19.5 °C		
Temperature of water after arc	29.5 °C		
Volume of water before arc	1,000 ml		
Volume of water that loosed during arc process	0 ml		
Volume of sample gas	7.0 ml		
Dependent variable: weight measurement			
Weight of CNHs floating on water surface	0.0102 g		
Weight of product inside cathode hole	0.2691 g		
% Yield = $\frac{\text{wt. of CNHs floating on water surface}}{\text{Consumed weight of anode}}$	2.99%		
Dependent variable: Gas chromatography analysis			
	Retention time (min)	Curve area	Concentration (ppm)
H ₂ gas analysis	0.612	113203	8317.63
	0.812	113355	8328.80
	0.835	114315	8399.34
CO gas analysis Sample gas 0.4 ml per one batch	4.736	6778	
	4.769	6735	
	4.440	6638	
Comment:			
Step arc occurred			

Table A.5 Data sheet of experiment on SWCNHs synthesis at 23°C

Data Sheet for Batch NO.30 (11 Nov, 08)			
Constant variable			
Arc current	80 A		
Arc time	15 sec		
N ₂ gas flow rate	5 L/min		
Anode ascending velocity	1.5 mm/s		
Cathode			
Weight before arc	7.1670 g		
Weight after arc	7.4256 g		
Length before arc	49.2 mm		
Length after arc	49.2 mm		
Anode			
Weight before arc	0.9555 g		
Weight after arc	0.6064 g		
Consumed weight	0.3491 g		
Length before arc	76.3 mm		
Length after arc	47.5 mm		
Loss of length	28.8 mm		
Independent variable			
Temperature of water before arc	23 °C		
Temperature of water after arc	29.3 °C		
Volume of water before arc	1,000 ml		
Volume of water that loosed during arc process	30 ml		
Volume of sample gas	11.0 ml		
Dependent variable: weight measurement			
Weight of CNHs floating on water surface	0.0253 g		
Weight of product inside cathode hole	0.2320 g		
$\% \text{ Yield} = \frac{\text{wt. of CNHs floating on water surface}}{\text{Consumed weight of anode}}$			7.25%
Dependent variable: Gas chromatography analysis			
	Retention time (min)	Curve area	Concentration (ppm)
H ₂ gas analysis	0.832	45026	3308.30
	0.849	45600	3350.48
	0.845	46292	3401.32
CO gas analysis			
Comment:			

Table A.6 Data sheet of experiment on SWCNHs synthesis at 23.7°C

Data Sheet for Batch NO.33 (12 Nov, 08)			
Constant variable			
Arc current	80 A		
Arc time	15 sec		
N ₂ gas flow rate	5 L/min		
Anode ascending velocity	1.5 mm/s		
Cathode			
Weight before arc	7.0120 g		
Weight after arc	7.3370 g		
Length before arc	49.9 mm		
Length after arc	49.9 mm		
Anode			
Weight before arc	0.8698 g		
Weight after arc	0.4935 g		
Consumed weight	0.3763 g		
Length before arc	69.3 mm		
Length after arc	42.3 mm		
Loss of length	27.0 mm		
Independent variable			
Temperature of water before arc	23.7 °C		
Temperature of water after arc	32 °C		
Volume of water before arc	1,000 ml		
Volume of water that loosed during arc process	25 ml		
Volume of sample gas	6.0 ml		
Dependent variable: weight measurement			
Weight of CNHs floating on water surface	0.0183 g		
Weight of product inside cathode hole	0.2909 g		
$\% \text{ Yield} = \frac{\text{wt. of CNHs floating on water surface}}{\text{Consumed weight of anode}}$			4.86%
Dependent variable: Gas chromatography analysis			
	Retention time (min)	Curve area	Concentration (ppm)
H ₂ gas analysis	0.839	69095	5076.78
	0.852	55822	4101.54
	0.845	61667	4531.01
CO gas analysis			
Comment:			

Table A.7 Data sheet of experiment on SWCNHs synthesis at 24°C

Data Sheet for Batch NO.34 (12 Nov, 08)			
Constant variable			
Arc current	80 A		
Arc time	15 sec		
N ₂ gas flow rate	5 L/min		
Anode ascending velocity	1.5 mm/s		
Cathode			
Weight before arc	7.0206 g		
Weight after arc	7.2101 g		
Length before arc	49.9 mm		
Length after arc	49.9 mm		
Anode			
Weight before arc	0.9487 g		
Weight after arc	0.6654 g		
Consumed weight	0.2833 g		
Length before arc	75.6 mm		
Length after arc	51.8 mm		
Loss of length	23.8 mm		
Independent variable			
Temperature of water before arc	24 °C		
Temperature of water after arc	28.2 °C		
Volume of water before arc	1,000 ml		
Volume of water that loosed during arc process	10 ml		
Volume of sample gas	6.0 ml		
Dependent variable: weight measurement			
Weight of CNHs floating on water surface	0.0229 g		
Weight of product inside cathode hole	0.1997 g		
% Yield = $\frac{\text{wt. of CNHs floating on water surface}}{\text{Consumed weight of anode}}$	8.08%		
Dependent variable: Gas chromatography analysis			
	Retention time (min)	Curve area	Concentration (ppm)
H ₂ gas analysis	0.855	35782	2629.10
	0.879	24734	1817.34
CO gas analysis			
Comment:			

Table A.8 Data sheet of experiment on SWCNHs synthesis at 46°C

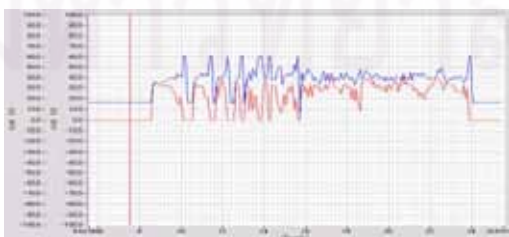
Data Sheet for Batch NO.38 (14 Nov, 08)			
Constant variable			
Arc current	80 A		
Arc time	15 sec		
N ₂ gas flow rate	5 L/min		
Anode ascending velocity	1.5 mm/s		
Cathode			
Weight before arc	7.1569 g		
Weight after arc	7.5115 g		
Length before arc	49.1 mm		
Length after arc	49.1 mm		
Anode			
Weight before arc	0.9334 g		
Weight after arc	0.5774 g		
Consumed weight	0.3560 g		
Length before arc	74.6 mm		
Length after arc	48.6 mm		
Loss of length	26.0 mm		
Independent variable			
Temperature of water before arc	46 °C		
Temperature of water after arc	54 °C		
Volume of water before arc	1,000 ml		
Volume of water that loosed during arc process	20 ml		
Volume of sample gas	5.0 ml		
Dependent variable: weight measurement			
Weight of CNHs floating on water surface	0.0034 g		
Weight of product inside cathode hole	0.3225 g		
% Yield = $\frac{\text{wt. of CNHs floating on water surface}}{\text{Consumed weight of anode}}$	0.96%		
Dependent variable: Gas chromatography analysis			
H ₂ gas analysis	Retention time (min)	Curve area	Concentration (ppm)
	0.865	81525	5990.08
	0.852	81053	5955.40
	0.852	81590	5994.86
Comment:			
Show a plot of current and voltage during arc discharge as a function of time.			

Table A.9 Data sheet of experiment on SWCNHs synthesis at 46°C

Data Sheet for Batch NO.47 (9 Dec, 08)			
Constant variable			
Arc current	80 A		
Arc time	15 sec		
N ₂ gas flow rate	5 L/min		
Anode ascending velocity	1.5 mm/s		
Cathode			
Weight before arc	6.7234 g		
Weight after arc	6.9482 g		
Length before arc	49.9 mm		
Length after arc	49.9 mm		
Anode			
Weight before arc	0.9061 g		
Weight after arc	0.5603 g		
Consumed weight	0.3458 g		
Length before arc	74.0 mm		
Length after arc	46.6 mm		
Loss of length	27.4 mm		
Independent variable			
Temperature of water before arc	46 °C		
Temperature of water after arc	56.5 °C		
Volume of water before arc	1,000 ml		
Volume of water that loosed during arc process	20 ml		
Volume of sample gas	6.0 ml		
Dependent variable: weight measurement			
Weight of CNHs floating on water surface	0.0077 g		
Weight of product inside cathode hole	0.2795 g		
% Yield = $\frac{\text{wt. of CNHs floating on water surface}}{\text{Consumed weight of anode}}$	2.23%		
Dependent variable: Gas chromatography analysis			
H ₂ gas analysis	Retention time (min)	Curve area	Concentration (ppm)
	0.829	194427	14254
	0.865	196141	14380
	0.855	196858	14432
Comment:			
Show a plot of current and voltage durin garc discharge as a function of time.			

Table A.10 Data sheet of experiment on SWCNHs synthesis at 47°C

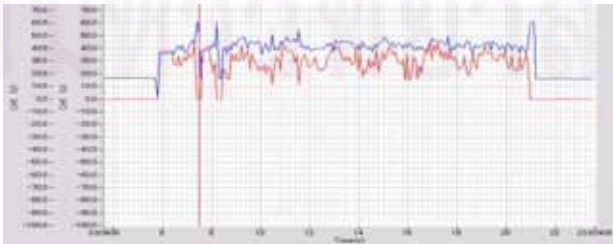
Data Sheet for Batch NO.48 (9 Dec, 08)			
Constant variable			
Arc current	80 A		
Arc time	15 sec		
N ₂ gas flow rate	5 L/min		
Anode ascending velocity	1.5 mm/s		
Cathode			
Weight before arc	6.9686 g		
Weight after arc	7.3094 g		
Length before arc	49.1 mm		
Length after arc	49.1 mm		
Anode			
Weight before arc	0.9040 g		
Weight after arc	0.5436 g		
Consumed weight	0.3604 g		
Length before arc	75.5 mm		
Length after arc	46.5 mm		
Loss of length	29.0 mm		
Independent variable			
Temperature of water before arc	47 °C		
Temperature of water after arc	55.5 °C		
Volume of water before arc	1,000 ml		
Volume of water that loosed during arc process	40 ml		
Volume of sample gas	7.0 ml		
Dependent variable: weight measurement			
Weight of CNHs floating on water surface	0.0102 g		
Weight of product inside cathode hole	0.3000 g		
% Yield = $\frac{\text{wt. of CNHs floating on water surface}}{\text{Consumed weight of anode}}$	2.83%		
Dependent variable: Gas chromatography analysis			
	Retention time (min)	Curve area	Concentration (ppm)
H ₂ gas analysis	0.869	180499	13233
	0.872	180745	13251
	0.862	182099	13350
Comment:			
Show a plot of current and voltage during arc discharge as a function of time.			

Table A.11 Data sheet of experiment on SWCNHs synthesis at 49°C

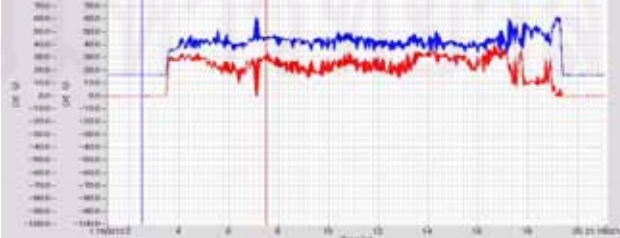
Data Sheet for Batch NO.44 (27 Nov, 08)			
Constant variable			
Arc current	80 A		
Arc time	15 sec		
N ₂ gas flow rate	5 L/min		
Anode ascending velocity	1.5 mm/s		
Cathode			
Weight before arc	6.7573 g		
Weight after arc	6.7785 g		
Length before arc	49.9 mm		
Length after arc	49.9 mm		
Anode			
Weight before arc	0.8949 g		
Weight after arc	0.5434 g		
Consumed weight	0.3515 g		
Length before arc	72.9 mm		
Length after arc	45.7 mm		
Loss of length	27.2 mm		
Independent variable			
Temperature of water before arc	49 °C		
Temperature of water after arc	57 °C		
Volume of water before arc	1,000 ml		
Volume of water that loosed during arc process	40 ml		
Volume of sample gas	15.0 ml		
Dependent variable: weight measurement			
Weight of CNHs floating on water surface	0.0119 g		
Weight of product inside cathode hole	0.2640 g		
% Yield = $\frac{\text{wt. of CNHs floating on water surface}}{\text{Consumed weight of anode}}$	3.38%		
Dependent variable: Gas chromatography analysis			
	Retention time (min)	Curve area	Concentration (ppm)
H ₂ gas analysis	0.842	226409	16599
	0.829	220850	16191
	0.835	224486	16458
Comment:			
Show a plot of current and voltage during arc discharge as a function of time.			

Table A.12 Data sheet of experiment on SWCNHs synthesis at 61°C

Data Sheet for Batch NO.46 (8 Dec, 08)			
Constant variable			
Arc current	80 A		
Arc time	15 sec		
N ₂ gas flow rate	5 L/min		
Anode ascending velocity	1.5 mm/s		
Cathode			
Weight before arc	6.7369 g		
Weight after arc	6.9394 g		
Length before arc	49.9 mm		
Length after arc	49.9 mm		
Anode			
Weight before arc	0.9178 g		
Weight after arc	0.6347 g		
Consumed weight	0.2831 g		
Length before arc	75.8 mm		
Length after arc	50.8 mm		
Loss of length	25.0 mm		
Independent variable			
Temperature of water before arc	61 °C		
Temperature of water after arc	66.5 °C		
Volume of water before arc	1,000 ml		
Volume of water that loosed during arc process	10 ml		
Volume of sample gas	2.5 ml		
Dependent variable: weight measurement			
Weight of CNHs floating on water surface	0.0024 g		
Weight of product inside cathode hole	0.1694 g		
% Yield = $\frac{\text{wt. of CNHs floating on water surface}}{\text{Consumed weight of anode}}$	0.85%		
Dependent variable: Gas chromatography analysis			
H ₂ gas analysis	Retention time (min)	Curve area	Concentration (ppm)
	0.845	161254	11822
	0.839	162050	11880
Comment:			
Show a plot of current and voltage during arc discharge as a function of time.			

Table A.13 Data sheet of experiment on SWCNHs synthesis at 62°C

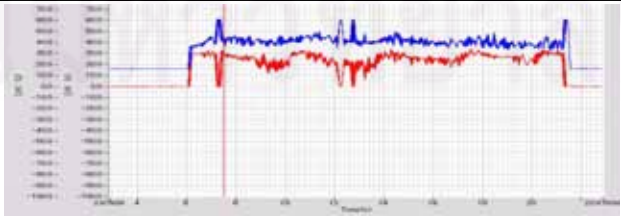
Data Sheet for Batch NO.41 (26 Nov, 08)			
Constant variable			
Arc current	80 A		
Arc time	15 sec		
N ₂ gas flow rate	5 L/min		
Anode ascending velocity	1.5 mm/s		
Cathode			
Weight before arc	7.1496 g		
Weight after arc	7.4452 g		
Length before arc	49.1 mm		
Length after arc	49.1 mm		
Anode			
Weight before arc	0.9098 g		
Weight after arc	0.5483 g		
Consumed weight	0.3615 g		
Length before arc	75.1 mm		
Length after arc	49.0 mm		
Loss of length	26.1 mm		
Independent variable			
Temperature of water before arc	62 °C		
Temperature of water after arc	68.5 °C		
Volume of water before arc	1,000 ml		
Volume of water that loosed during arc process	50 ml		
Volume of sample gas	3.0 ml		
Dependent variable: weight measurement			
Weight of CNHs floating on water surface	0.0137 g		
Weight of product inside cathode hole	0.2763 g		
% Yield = $\frac{\text{wt. of CNHs floating on water surface}}{\text{Consumed weight of anode}}$	3.79%		
Dependent variable: Gas chromatography analysis			
H ₂ gas analysis	Retention time (min)	Curve area	Concentration (ppm)
	0.839	59690	4376
Comment:			
Show a plot of current and voltage during arc discharge as a function of time.			

Table A.14 Data sheet of experiment on SWCNHs synthesis at 62°C

Data Sheet for Batch NO.43 (27 Nov, 08)			
Constant variable			
Arc current	80 A		
Arc time	15 sec		
N ₂ gas flow rate	5 L/min		
Anode ascending velocity	1.5 mm/s		
Cathode			
Weight before arc	7.0952 g		
Weight after arc	7.3532 g		
Length before arc	49.1 mm		
Length after arc	49.1 mm		
Anode			
Weight before arc	0.9006 g		
Weight after arc	0.5495 g		
Consumed weight	0.3511 g		
Length before arc	75.0 mm		
Length after arc	47.4 mm		
Loss of length	27.6 mm		
Independent variable			
Temperature of water before arc	62 °C		
Temperature of water after arc	68 °C		
Volume of water before arc	1,000 ml		
Volume of water that loosed during arc process	50 ml		
Volume of sample gas	9.0 ml		
Dependent variable: weight measurement			
Weight of CNHs floating on water surface	0.0116 g		
Weight of product inside cathode hole	0.2362 g		
% Yield = $\frac{\text{wt. of CNHs floating on water surface}}{\text{Consumed weight of anode}}$	3.30%		
Dependent variable: Gas chromatography analysis			
H ₂ gas analysis	Retention time (min)	Curve area	Concentration (ppm)
	0.839	254377	18649
	0.842	290005	21261
Comment:			
Show a plot of current and voltage during arc discharge as a function of time.			

Table A.15 Data sheet of experiment on SWCNHs synthesis at 79°C

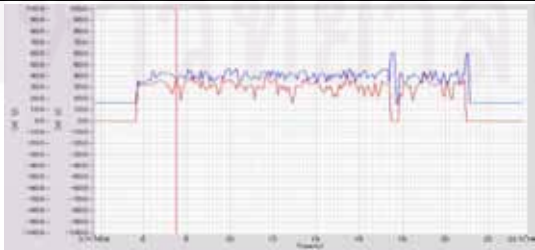
Data Sheet for Batch NO.39 (14 Nov, 08)			
Constant variable			
Arc current	80 A		
Arc time	15 sec		
N ₂ gas flow rate	5 L/min		
Anode ascending velocity	1.5 mm/s		
Cathode			
Weight before arc	6.9967 g		
Weight after arc	7.1224 g		
Length before arc	49.9 mm		
Length after arc	49.9 mm		
Anode			
Weight before arc	0.9352 g		
Weight after arc	0.5531 g		
Consumed weight	0.3821 g		
Length before arc	74.5 mm		
Length after arc	47.8 mm		
Loss of length	26.7 mm		
Independent variable			
Temperature of water before arc	79 °C		
Temperature of water after arc	81 °C		
Volume of water before arc	1,000 ml		
Volume of water that loosed during arc process	90 ml		
Volume of sample gas	4.0 ml		
Dependent variable: weight measurement			
Weight of CNHs floating on water surface	0.0020 g		
Weight of product inside cathode hole	0.2684 g		
% Yield = $\frac{\text{wt. of CNHs floating on water surface}}{\text{Consumed weight of anode}}$	0.52%		
Dependent variable: Gas chromatography analysis			
H ₂ gas analysis	Retention time (min)	Curve area	Concentration (ppm)
	0.872	255049	18739.82
	0.855	249504	18332.40
Curve area out of rage of calibration curve			
Comment:			
Show a plot of current and voltage during arc discharge as a function of time.			

Table A.16 Data sheet of experiment on SWCNHs synthesis at 79°C

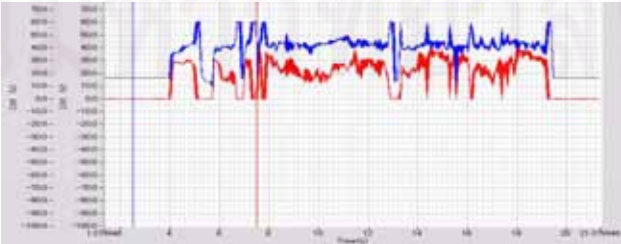
Data Sheet for Batch NO.45 (8 Dec, 08)			
Constant variable			
Arc current	80 A		
Arc time	15 sec		
N ₂ gas flow rate	5 L/min		
Anode ascending velocity	1.5 mm/s		
Cathode			
Weight before arc	7.0593 g		
Weight after arc	7.3520 g		
Length before arc	49.1 mm		
Length after arc	49.1 mm		
Anode			
Weight before arc	0.9566 g		
Weight after arc	0.6030 g		
Consumed weight	0.3536 g		
Length before arc	76.8 mm		
Length after arc	49.7 mm		
Loss of length	27.1 mm		
Independent variable			
Temperature of water before arc	79 °C		
Temperature of water after arc	81.5 °C		
Volume of water before arc	1,000 ml		
Volume of water that loosed during arc process	40 ml		
Volume of sample gas	3.0 ml		
Dependent variable: weight measurement			
Weight of CNHs floating on water surface	0.0015 g		
Weight of product inside cathode hole	0.2367 g		
% Yield = $\frac{\text{wt. of CNHs floating on water surface}}{\text{Consumed weight of anode}}$	0.42%		
Dependent variable: Gas chromatography analysis			
H ₂ gas analysis	Retention time (min)	Curve area	Concentration (ppm)
	0.859	358616	26292
	0.849	318172	23326
	0.862	309875	22718
Comment:			
Show a plot of current and voltage during arc discharge as a function of time.			

Table A.17 Data sheet of experiment on SWCNHs synthesis at 83°C

Data Sheet for Batch NO.37 (14 Nov, 08)			
Constant variable			
Arc current	80 A		
Arc time	15 sec		
N ₂ gas flow rate	5 L/min		
Anode ascending velocity	1.5 mm/s		
Cathode			
Weight before arc	6.9912 g		
Weight after arc	7.2349 g		
Length before arc	49.8 mm		
Length after arc	49.8 mm		
Anode			
Weight before arc	0.9304 g		
Weight after arc	0.6348 g		
Consumed weight	0.2956 g		
Length before arc	74.3 mm		
Length after arc	48.6 mm		
Loss of length	26.7 mm		
Independent variable			
Temperature of water before arc	83 °C		
Temperature of water after arc	90 °C		
Volume of water before arc	1,000 ml		
Volume of water that loosed during arc process	70 ml		
Volume of sample gas	6.0 ml		
Dependent variable: weight measurement			
Weight of CNHs floating on water surface	0.0043 g		
Weight of product inside cathode hole	0.2131 g		
% Yield = $\frac{\text{wt. of CNHs floating on water surface}}{\text{Consumed weight of anode}}$	1.45%		
Dependent variable: Gas chromatography analysis			
H ₂ gas analysis	Retention time (min)	Curve area	Concentration (ppm)
	0.825	18875	855.23
	0.842	18932	857.82
	0.522	17800	806.52
Commendation:			
Show a plot of current and voltage during arc discharge as a function of time.			

APPENDIX B

EXPERIMENTAL DATA FOR SWCNHs/Pd SYNTHESIS

Data sheet of experiment on SWCNHs/Pd nanocomposite synthesis by GI-AIW method by inserting Pd wire inside anode hole is shown in appendix B. The data sheet is used for plotting yield of SWCNHs and Pd nanoparticle in Fig 4.21.

The data sheet which is shown in this section can be catalogued in four groups of water temperature as following:

Group 1: using Pd wire diameter of 0.1 mm is shown in Table B.1- B.4

Group 2: using Pd wire diameter of 0.3 mm is shown in Table B.5- B.9

Group 3: using Pd wire diameter of 0.5 mm is shown in Table B.10- B.14

Group 4: using Pd wire diameter of 0.8 mm is shown in Table B.15- B.17

Table B.1 Data sheet on SWCNHs/Pd synthesis with using Pd wire of 0.1 mm

Data Sheet for Batch No.3 (22 April, 09)	
Constant variable	
Arc current	80 A
Arc time	7 sec
N ₂ gas flow rate	5 L/min
Anode ascending velocity	1.5 mm/s
Cathode	
Weight before arc	6.8089 g
Weight after arc	6.8328 g
Length before arc	49.8 mm
Length after arc	49.8 mm
Anode	
Weight before arc	0.8277 g
Weight after arc	0.7074 g
Consumed weight	0.1203 g
Length before arc	69.8 mm
Length after arc	57.9 mm
Loss of length	11.9 mm
Anode hole	
Diameter of hole	1.0 mm
Length of hole before arc	14.7 mm
Length of hole after arc	1.3 mm
Loss of hole length	13.4 mm
Independent variable	
Diameter of palladium wire	0.10 mm
Length of palladium wire before arc	15.0 mm
Length of palladium wire after arc	0 mm completely consumed
Weight of palladium wire	0.0017 g
Total weight of Pd and C	0.1220 g
Weight ratio of Pd/C	0.0141
Dependent variable: weight measurement	
Weight of CNHs/Pd floating on water surface	0.0032 g
Weight of product inside cathode hole	0.0726 g

Table B.2 Data sheet on SWCNHs/Pd synthesis with using Pd wire of 0.1 mm

Data Sheet for Batch No.9 (28 April, 09)	
Constant variable	
Arc current	80 A
Arc time	15 sec
N ₂ gas flow rate	5 L/min
Anode ascending velocity	1.5 mm/s
Cathode	
Weight before arc	6.6075 g
Weight after arc	6.6170 g
Length before arc	49.9 mm
Length after arc	49.9 mm
Anode	
Weight before arc	0.7142 g
Weight after arc	0.4400 g
Consumed weight	0.2742 g
Length before arc	61.9 mm
Length after arc	37.5 mm
Loss of length	24.4 mm
Anode hole	
Diameter of hole	1.0 mm
Length of hole before arc	24.5 mm
Length of hole after arc	0 mm
Loss of hole length	24.5 mm
Independent variable	
Diameter of palladium wire	0.10 mm
Length of palladium wire before arc	23.5 mm
Length of palladium wire after arc	0 mm completely consumed
Weight of palladium wire	0.0021 g
Total weight of Pd and C	0.2763 g
Weight ratio of Pd/C	0.0077
Dependent variable: weight measurement	
Weight of CNHs/Pd floating on water surface	0.0101 g
Weight of product inside cathode hole	0.1925 g

Table B.3 Data sheet on SWCNHs/Pd synthesis with using Pd wire of 0.1 mm

Data Sheet for Batch No.12 (5 May, 09)	
Constant variable	
Arc current	80 A
Arc time	15 sec
N ₂ gas flow rate	5 L/min
Anode ascending velocity	1.5 mm/s
Cathode	
Weight before arc	6.5617 g
Weight after arc	6.5586 g
Length before arc	49.9 mm
Length after arc	49.9 mm
Anode	
Weight before arc	0.8794 g
Weight after arc	0.5981 g
Consumed weight	0.2813 g
Length before arc	74.3 mm
Length after arc	50.1 mm
Loss of length	24.2 mm
Anode hole	
Diameter of hole	1.0 mm
Length of hole before arc	24.6 mm
Length of hole after arc	0.8 mm
Loss of hole length	23.8 mm
Independent variable	
Diameter of palladium wire	0.10 mm
Length of palladium wire before arc	23.6 mm
Length of palladium wire after arc	0 mm completely consumed
Weight of palladium wire	0.0021 g
Total weight of Pd and C	0.2834 g
Weight ratio of Pd/C	0.0075
Dependent variable: weight measurement	
Weight of CNHs/Pd floating on water surface	0.0124 g
Weight of product inside cathode hole	0.1875 g

Table B.4 Data sheet on SWCNHs/Pd synthesis with using Pd wire of 0.1 mm

Data Sheet for Batch No.13 (5 May, 09)	
Constant variable	
Arc current	80 A
Arc time	15 sec
N ₂ gas flow rate	5 L/min
Anode ascending velocity	1.5 mm/s
Cathode	
Weight before arc	6.7572 g
Weight after arc	6.7535 g
Length before arc	49.1 mm
Length after arc	49.1 mm
Anode	
Weight before arc	0.8299 g
Weight after arc	0.5709 g
Consumed weight	0.2590 g
Length before arc	74.3 mm
Length after arc	50.2 mm
Loss of length	24.1 mm
Anode hole	
Diameter of hole	1.0 mm
Length of hole before arc	23.4 mm
Length of hole after arc	0.6 mm
Loss of hole length	22.8 mm
Independent variable	
Diameter of palladium wire	0.10 mm
Length of palladium wire before arc	22.4 mm
Length of palladium wire after arc	0 mm completely consumed
Weight of palladium wire	0.0020 g
Total weight of Pd and C	0.2610 g
Weight ratio of Pd/C	0.0077
Dependent variable: weight measurement	
Weight of CNHs/Pd floating on water surface	0.0139 g
Weight of product inside cathode hole	0.1240 g

Table B.5 Data sheet on SWCNHs/Pd synthesis with using Pd wire of 0.3 mm

Data Sheet for Batch No.1 (20 April, 09)	
Constant variable	
Arc current	80 A
Arc time	7 sec
N ₂ gas flow rate	5 L/min
Anode ascending velocity	1.5 mm/s
Cathode	
Weight before arc	6.9423 g
Weight after arc	7.0127 g
Length before arc	49.1 mm
Length after arc	49.1 mm
Anode	
Weight before arc	0.8806 g
Weight after arc	0.7120 g
Consumed weight	0.1686 g
Length before arc	74.3 mm
Length after arc	59.7 mm
Loss of length	14.6 mm
Anode hole	
Diameter of hole	1.0 mm
Length of hole before arc	15.0 mm
Length of hole after arc	1.3 mm
Loss of hole length	13.7 mm
Independent variable	
Diameter of palladium wire	0.30 mm
Length of palladium wire before arc	15.0 mm
Length of palladium wire after arc	0 mm completely consumed
Weight of palladium wire	0.0132 g
Total weight of Pd and C	0.1818 g
Weight ratio of Pd/C	0.0783
Dependent variable: weight measurement	
Weight of CNHs/Pd floating on water surface	0.0036 g
Weight of product inside cathode hole	0.1186 g

Table B.6 Data sheet on SWCNHs/Pd synthesis with using Pd wire of 0.3 mm

Data Sheet for Batch No.2 (21 April, 09)	
Constant variable	
Arc current	80 A
Arc time	7 sec
N ₂ gas flow rate	5 L/min
Anode ascending velocity	1.5 mm/s
Cathode	
Weight before arc	6.9297 g
Weight after arc	6.9731 g
Length before arc	49.1 mm
Length after arc	49.1 mm
Anode	
Weight before arc	0.8965 g
Weight after arc	0.7165 g
Consumed weight	0.1800 g
Length before arc	75.8 mm
Length after arc	58.9 mm
Loss of length	16.9 mm
Anode hole	
Diameter of hole	1.0 mm
Length of hole before arc	15.3 mm
Length of hole after arc	0 mm
Loss of hole length	15.3 mm
Independent variable	
Diameter of palladium wire	0.30 mm
Length of palladium wire before arc	15.0 mm
Length of palladium wire after arc	0 mm completely consumed
Weight of palladium wire	0.0128 g
Total weight of Pd and C	0.1928 g
Weight ratio of Pd/C	0.0711
Dependent variable: weight measurement	
Weight of CNHs/Pd floating on water surface	0.0094 g
Weight of product inside cathode hole	0.1368 g

Table B.7 Data sheet on SWCNHs/Pd synthesis with using Pd wire of 0.3 mm

Data Sheet for Batch No.14 (5 May, 09)	
Constant variable	
Arc current	80 A
Arc time	15 sec
N ₂ gas flow rate	5 L/min
Anode ascending velocity	1.5 mm/s
Cathode	
Weight before arc	6.5576 g
Weight after arc	6.5659 g
Length before arc	49.9 mm
Length after arc	49.9 mm
Anode	
Weight before arc	0.8416 g
Weight after arc	0.5456 g
Consumed weight	0.2960 g
Length before arc	87.4 mm
Length after arc	49.8 mm
Loss of length	37.6 mm
Anode hole	
Diameter of hole	1.0 mm
Length of hole before arc	22.8 mm
Length of hole after arc	0 mm
Loss of hole length	22.8 mm
Independent variable	
Diameter of palladium wire	0.30 mm
Length of palladium wire before arc	21.8 mm
Length of palladium wire after arc	0 mm completely consumed
Weight of palladium wire	0.0184 g
Total weight of Pd and C	0.3144 g
Weight ratio of Pd/C	0.0622
Dependent variable: weight measurement	
Weight of CNHs/Pd floating on water surface	0.0138 g
Weight of product inside cathode hole	0.2278 g

Table B.8 Data sheet on SWCNHs/Pd synthesis with using Pd wire of 0.3 mm

Data Sheet for Batch No.15 (6 May, 09)	
Constant variable	
Arc current	80 A
Arc time	15 sec
N ₂ gas flow rate	5 L/min
Anode ascending velocity	1.5 mm/s
Cathode	
Weight before arc	6.5522 g
Weight after arc	6.5565 g
Length before arc	49.9 mm
Length after arc	49.9 mm
Anode	
Weight before arc	0.8581 g
Weight after arc	0.5676 g
Consumed weight	0.2905 g
Length before arc	73.9 mm
Length after arc	49.6 mm
Loss of length	24.3 mm
Anode hole	
Diameter of hole	1.0 mm
Length of hole before arc	24.0 mm
Length of hole after arc	0 mm
Loss of hole length	24.0 mm
Independent variable	
Diameter of palladium wire	0.30 mm
Length of palladium wire before arc	23.0 mm
Length of palladium wire after arc	0 mm completely consumed
Weight of palladium wire	0.0195 g
Total weight of Pd and C	0.3100 g
Weight ratio of Pd/C	0.0671
Dependent variable: weight measurement	
Weight of CNHs/Pd floating on water surface	0.0125 g
Weight of product inside cathode hole	0.2231 g

Table B.9 Data sheet on SWCNHs/Pd synthesis with using Pd wire of 0.3 mm

Data Sheet for Batch No.16 (6 May, 09)	
Constant variable	
Arc current	80 A
Arc time	15 sec
N ₂ gas flow rate	5 L/min
Anode ascending velocity	1.5 mm/s
Cathode	
Weight before arc	6.7520 g
Weight after arc	6.7562 g
Length before arc	49.1 mm
Length after arc	49.1 mm
Anode	
Weight before arc	0.8233 g
Weight after arc	0.5217 g
Consumed weight	0.3016 g
Length before arc	74.7 mm
Length after arc	50.4 mm
Loss of length	24.3 mm
Anode hole	
Diameter of hole	1.0 mm
Length of hole before arc	25.5 mm
Length of hole after arc	1.6 mm
Loss of hole length	23.9 mm
Independent variable	
Diameter of palladium wire	0.30 mm
Length of palladium wire before arc	24.5 mm
Length of palladium wire after arc	0 mm completely consumed
Weight of palladium wire	0.0208 g
Total weight of Pd and C	0.3224 g
Weight ratio of Pd/C	0.0690
Dependent variable: weight measurement	
Weight of CNHs/Pd floating on water surface	0.0175 g
Weight of product inside cathode hole	0.2314 g

Table B.10 Data sheet on SWCNHs/Pd synthesis with using Pd wire of 0.5 mm

Data Sheet for Batch No.7 (28 April, 09)	
Constant variable	
Arc current	80 A
Arc time	15 sec
N ₂ gas flow rate	5 L/min
Anode ascending velocity	1.5 mm/s
Cathode	
Weight before arc	6.7473 g
Weight after arc	6.6160 g
Length before arc	49.9 mm
Length after arc	49.9 mm
Anode	
Weight before arc	0.8676 g
Weight after arc	0.5389 g
Consumed weight	0.3287 g
Length before arc	74.0 mm
Length after arc	49.1 mm
Loss of length	24.9 mm
Anode hole	
Diameter of hole	1.0 mm
Length of hole before arc	23.5 mm
Length of hole after arc	0 mm
Loss of hole length	23.5 mm
Independent variable	
Diameter of palladium wire	0.50 mm
Length of palladium wire before arc	23.1 mm
Length of palladium wire after arc	0 mm completely consumed
Weight of palladium wire	0.0537 g
Total weight of Pd and C	0.3824 g
Weight ratio of Pd/C	0.1634
Dependent variable: weight measurement	
Weight of CNHs/Pd floating on water surface	0.0148 g
Weight of product inside cathode hole	0.2384 g

Table B.11 Data sheet on SWCNHs/Pd synthesis with using Pd wire of 0.5 mm

Data Sheet for Batch No.17 (6 May, 09)	
Constant variable	
Arc current	80 A
Arc time	15 sec
N ₂ gas flow rate	5 L/min
Anode ascending velocity	1.5 mm/s
Cathode	
Weight before arc	6.5544 g
Weight after arc	6.5646 g
Length before arc	49.9 mm
Length after arc	49.9 mm
Anode	
Weight before arc	0.8442 g
Weight after arc	0.5548 g
Consumed weight	0.2894 g
Length before arc	73.8 mm
Length after arc	49.7 mm
Loss of length	24.1 mm
Anode hole	
Diameter of hole	1.0 mm
Length of hole before arc	23.9 mm
Length of hole after arc	0 mm
Loss of hole length	23.9 mm
Independent variable	
Diameter of palladium wire	0.50 mm
Length of palladium wire before arc	22.9 mm
Length of palladium wire after arc	0 mm completely consumed
Weight of palladium wire	0.0531 g
Total weight of Pd and C	0.3425 g
Weight ratio of Pd/C	0.1835
Dependent variable: weight measurement	
Weight of CNHs/Pd floating on water surface	0.0139 g
Weight of product inside cathode hole	0.2450 g

Table B.12 Data sheet on SWCNHs/Pd synthesis with using Pd wire of 0.5 mm

Data Sheet for Batch No.19 (6 May, 09)	
Constant variable	
Arc current	80 A
Arc time	15 sec
N ₂ gas flow rate	5 L/min
Anode ascending velocity	1.5 mm/s
Cathode	
Weight before arc	6.5470 g
Weight after arc	6.5374 g
Length before arc	49.9 mm
Length after arc	49.9 mm
Anode	
Weight before arc	0.8393 g
Weight after arc	0.5298 g
Consumed weight	0.3095 g
Length before arc	74.3 mm
Length after arc	49.3 mm
Loss of length	25.0 mm
Anode hole	
Diameter of hole	1.0 mm
Length of hole before arc	23.1 mm
Length of hole after arc	0 mm
Loss of hole length	23.1 mm
Independent variable	
Diameter of palladium wire	0.50 mm
Length of palladium wire before arc	22.1 mm
Length of palladium wire after arc	0 mm completely consumed
Weight of palladium wire	0.0528 g
Total weight of Pd and C	0.3623 g
Weight ratio of Pd/C	0.1706
Dependent variable: weight measurement	
Weight of CNHs/Pd floating on water surface	0.0123 g
Weight of product inside cathode hole	0.2561 g

Table B.13 Data sheet on SWCNHs/Pd synthesis with using Pd wire of 0.5 mm

Data Sheet for Batch No.22 (20 May, 09)	
Constant variable	
Arc current	60 A
Arc time	15 sec
N ₂ gas flow rate	5 L/min
Anode ascending velocity	1.5 mm/s
Cathode	
Weight before arc	6.5335 g
Weight after arc	6.5313 g
Length before arc	49.9 mm
Length after arc	49.9 mm
Anode	
Weight before arc	0.8843 g
Weight after arc	0.7234 g
Consumed weight	0.1609 g
Length before arc	74.6 mm
Length after arc	60.0 mm
Loss of length	24.6 mm
Anode hole	
Diameter of hole	1.0 mm
Length of hole before arc	23.9 mm
Length of hole after arc	6.4 mm
Loss of hole length	17.5 mm
Independent variable	
Diameter of palladium wire	0.50 mm
Length of palladium wire before arc	22.9 mm
Length of palladium wire after arc	0 mm completely consumed
Weight of palladium wire	0.0534 g
Total weight of Pd and C	0.2143 g
Weight ratio of Pd/C	0.3319
Dependent variable: weight measurement	
Weight of CNHs/Pd floating on water surface	0.0072 g
Weight of product inside cathode hole	0.1605 g

Table B.14 Data sheet on SWCNHs/Pd synthesis with using Pd wire of 0.5 mm

Data Sheet for Batch No.23 (20 May, 09)	
Constant variable	
Arc current	80 A
Arc time	15 sec
N ₂ gas flow rate	5 L/min
Anode ascending velocity	1.5 mm/s
Cathode	
Weight before arc	6.7306 g
Weight after arc	6.7474 g
Length before arc	49.1 mm
Length after arc	49.1 mm
Anode	
Weight before arc	0.8948 g
Weight after arc	0.5995 g
Consumed weight	0.2953 g
Length before arc	75.7 mm
Length after arc	51.3 mm
Loss of length	24.4 mm
Anode hole	
Diameter of hole	1.0 mm
Length of hole before arc	23.3 mm
Length of hole after arc	0 mm
Loss of hole length	23.3 mm
Independent variable	
Diameter of palladium wire	0.50 mm
Length of palladium wire before arc	22.3 mm
Length of palladium wire after arc	0 mm completely consumed
Weight of palladium wire	0.0514 g
Total weight of Pd and C	0.3467 g
Weight ratio of Pd/C	0.1741
Dependent variable: weight measurement	
Weight of CNHs/Pd floating on water surface	0.0148 g
Weight of product inside cathode hole	0.2684 g

Table B.15 Data sheet on SWCNHs/Pd synthesis with using Pd wire of 0.8 mm

Data Sheet for Batch No.8 (28 April, 09)	
Constant variable	
Arc current	80 A
Arc time	15 sec
N ₂ gas flow rate	5 L/min
Anode ascending velocity	1.5 mm/s
Cathode	
Weight before arc	6.8340 g
Weight after arc	6.8814 g
Length before arc	49.1 mm
Length after arc	49.1 mm
Anode	
Weight before arc	0.8695 g
Weight after arc	0.5740 g
Consumed weight	0.2955 g
Length before arc	74.6 mm
Length after arc	49.9 mm
Loss of length	24.7 mm
Anode hole	
Diameter of hole	1.0 mm
Length of hole before arc	24.3 mm
Length of hole after arc	0 mm
Loss of hole length	24.3 mm
Independent variable	
Diameter of palladium wire	0.80 mm
Length of palladium wire before arc	23.3 mm
Length of palladium wire after arc	0 mm completely consumed
Weight of palladium wire	0.1380 g
Total weight of Pd and C	0.4335 g
Weight ratio of Pd/C	0.4670
Dependent variable: weight measurement	
Weight of CNHs/Pd floating on water surface	0.0220 g
Weight of product inside cathode hole	0.3259 g

Table B.16 Data sheet on SWCNHs/Pd synthesis with using Pd wire of 0.8 mm

Data Sheet for Batch No.21 (6 May, 09)	
Constant variable	
Arc current	80 A
Arc time	15 sec
N ₂ gas flow rate	5 L/min
Anode ascending velocity	1.5 mm/s
Cathode	
Weight before arc	6.5372 g
Weight after arc	6.5331 g
Length before arc	49.9 mm
Length after arc	49.9 mm
Anode	
Weight before arc	0.8744 g
Weight after arc	0.5521 g
Consumed weight	0.3223 g
Length before arc	74.0 mm
Length after arc	49.0 mm
Loss of length	25.0 mm
Anode hole	
Diameter of hole	1.0 mm
Length of hole before arc	23.3 mm
Length of hole after arc	0 mm
Loss of hole length	23.3 mm
Independent variable	
Diameter of palladium wire	0.80 mm
Length of palladium wire before arc	21.4 mm
Length of palladium wire after arc	0 mm completely consumed
Weight of palladium wire	0.1238 g
Total weight of Pd and C	0.4461 g
Weight ratio of Pd/C	0.03841
Dependent variable: weight measurement	
Weight of CNHs/Pd floating on water surface	0.0181 g
Weight of product inside cathode hole	0.3234 g

Table B.17 Data sheet on SWCNHs/Pd synthesis with using Pd wire of 0.8 mm

Data Sheet for Batch No. 24 (20 May, 09)	
Constant variable	
Arc current	80 A
Arc time	15 sec
N ₂ gas flow rate	5 L/min
Anode ascending velocity	1.5 mm/s
Cathode	
Weight before arc	6.5290 g
Weight after arc	6.5549 g
Length before arc	49.9 mm
Length after arc	49.9 mm
Anode	
Weight before arc	0.8717 g
Weight after arc	0.5447 g
Consumed weight	0.3270 g
Length before arc	74.8 mm
Length after arc	49.3 mm
Loss of length	25.5 mm
Anode hole	
Diameter of hole	1.0 mm
Length of hole before arc	23.3 mm
Length of hole after arc	0 mm
Loss of hole length	23.3 mm
Independent variable	
Diameter of palladium wire	0.80 mm
Length of palladium wire before arc	22.3 mm
Length of palladium wire after arc	0 mm completely consumed
Weight of palladium wire	0.1333 g
Total weight of Pd and C	0.4603 g
Weight ratio of Pd/C	0.4076
Dependent variable: weight measurement	
Weight of CNHs/Pd floating on water surface	0.0246 g
Weight of product inside cathode hole	0.3720 g

APPENDIX C

CALCULATION FOR ARC TEMPERATURE

As mention in section 3.1.5, the spectra of arc plasma radiation inside cathode hole were measured. The spectrums are shown in Fig. AC1, one spectrum stand for one time that was collected radiation intensity in all wavelengths.

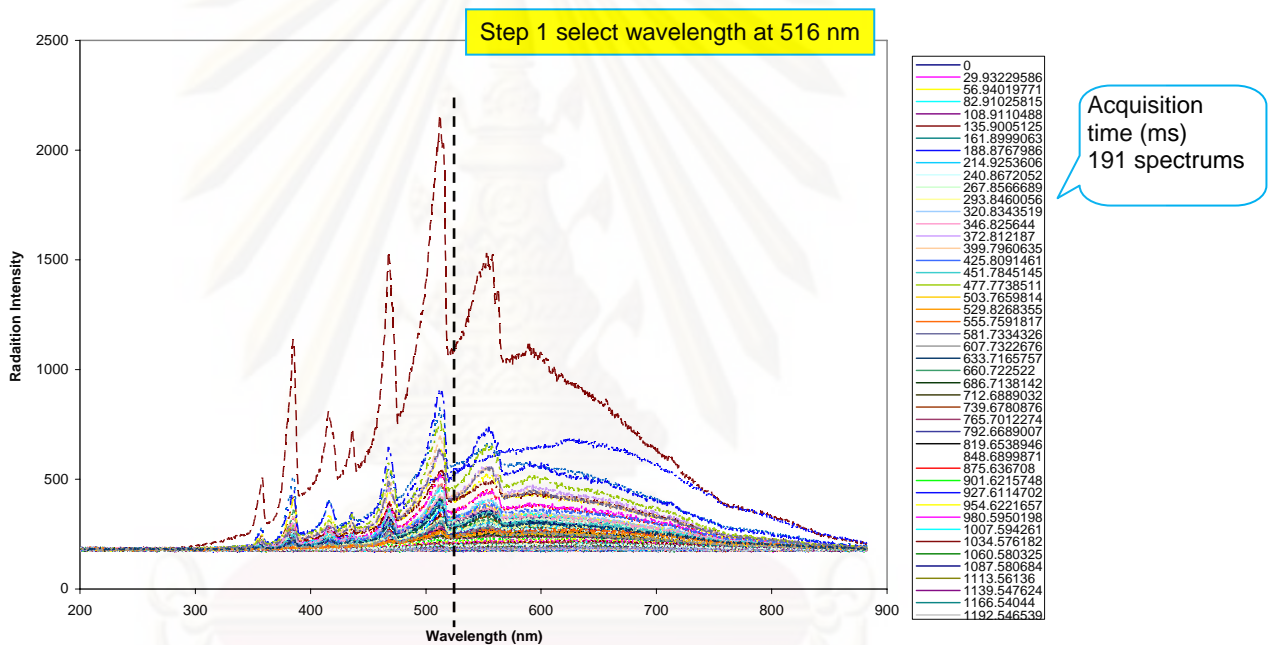


Figure AC1 Optical spectrum of arc plasma inside cathode hole

The way to manipulate spectrums data for estimating the temperature of arc plasma is described step by step as following.

Step 1 Reference from the study on arc plasma of Muthakarn et al [40], they can be recognized that there are peaks associated with C_2 radical at 516 nm, H_α at 660 nm and H_γ at 433 nm (highest energy emitted from excited state). Because we focus on

the range which SWCNHs are generated, thus we selected data at wavelength of 516 nm. From the recording spectra, the selected spectra are 515.59, 515.94 and 516.29 nm.

Step 2 Make a plot of intensity as a function of time for selected wavelength (Fig. AC 2) and select the effective time that have highest intensity (high temperature) and SWCNHs are generated. From this result, we select the interval time between 4262.6683 ms to 5000 ms and selected 10 values of time with same interval in this effective time range

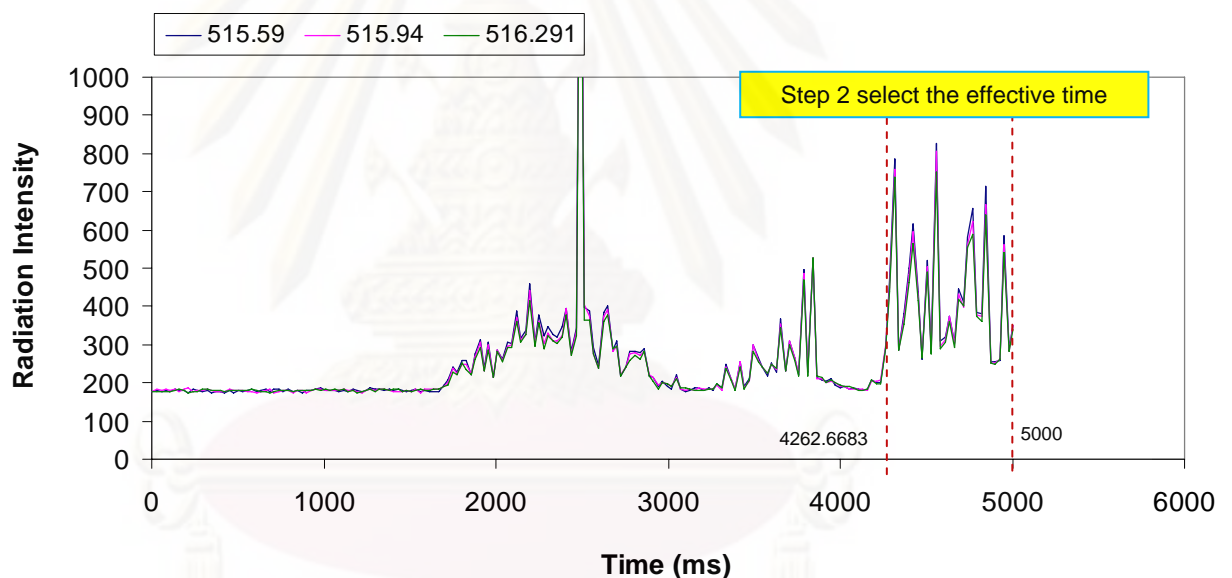


Figure AC2 Selected optical spectra of arc plasma as a function of time

Step 3 Re-plot the spectrums of 10 values of selected effective time and find the λ_{\max} from each spectrum. The spectrums can be classified according to the characteristic of spectra as shown in Fig. AC3.

Group 1: the smooth curve spectrum and sharp peak are clearly separated.

Group 2: the smooth curve spectrum and sharp peak are not clearly separated.

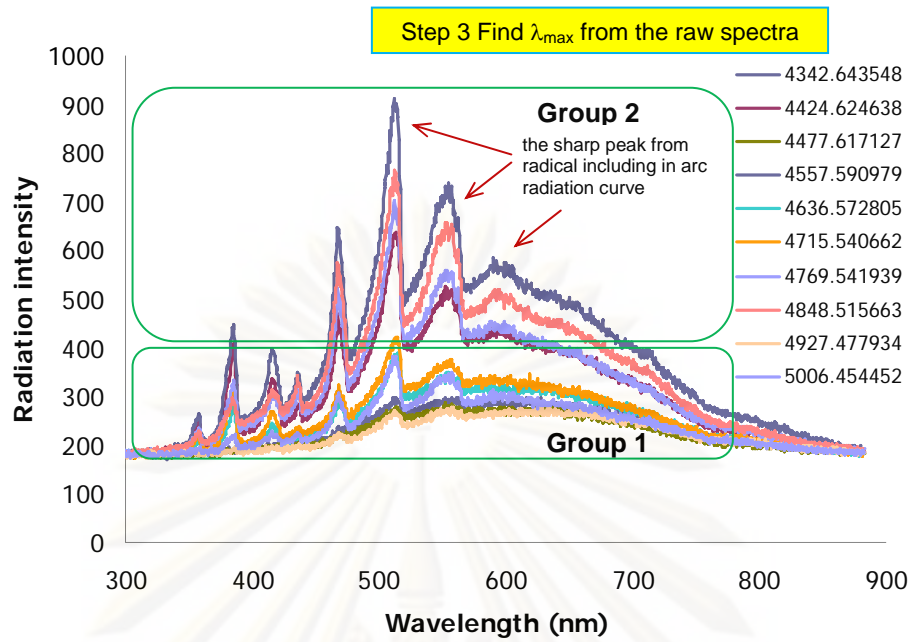


Figure AC3 Two group of optical spectra of arc plasma

Group 1 Find λ_{max} directly from the raw spectrum and determine the temperature from *Wien's displacement law* [Equation AC1]. The results are shown in the table below.

$$\lambda_{max} T = 0.2884 \text{ cm K} \tag{AC1}$$

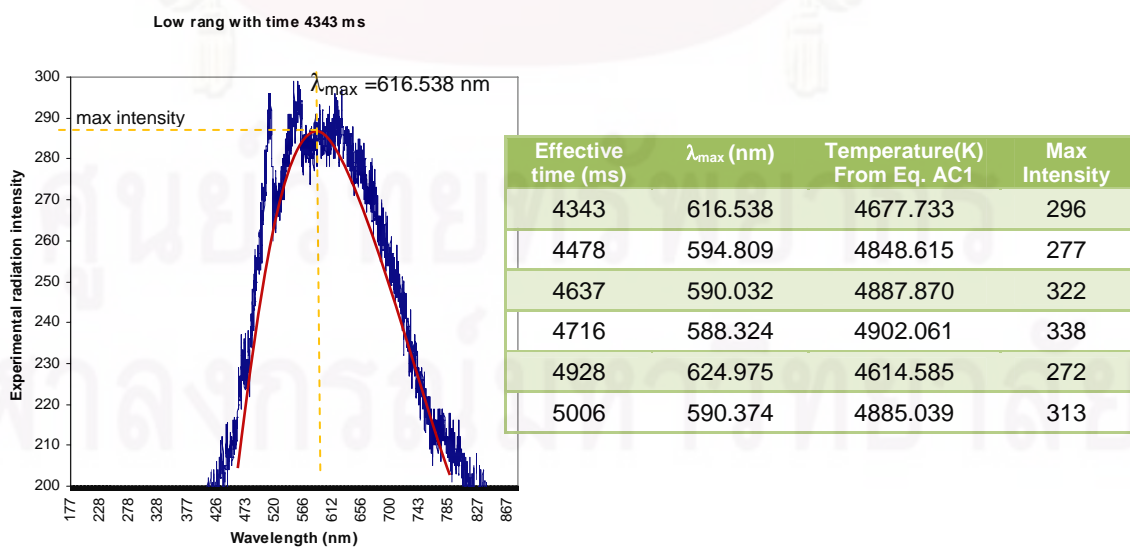
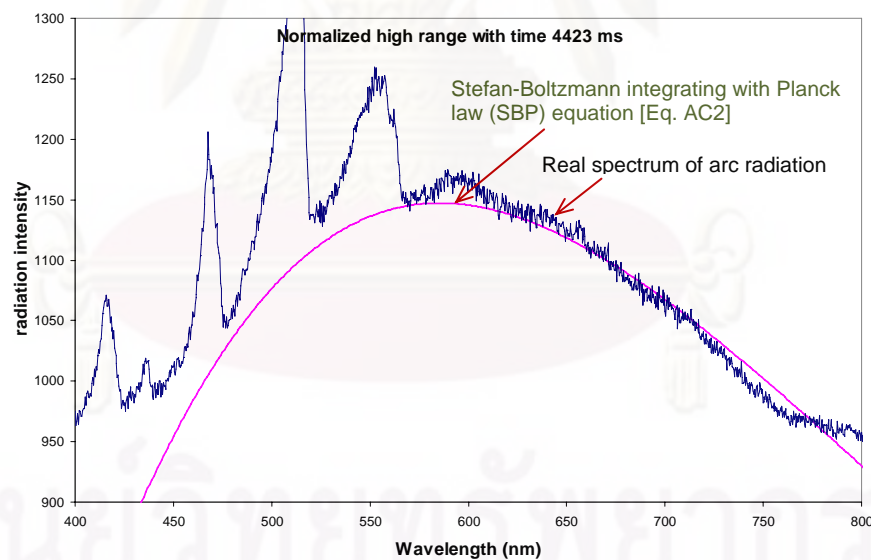


Figure AC4 Example of finding λ_{max} from spectrum and theirs results

Group 2 It can find λ_{\max} by applying with *Stefan-Boltzmann law* integrating with *Planck distribution law*; SBP [Equation AC2] for black body radiation for fitting with the spectrum to estimate the temperature. The way for adjust curve from Eq. AC2 is trial and error with changing the temperature and multiplying the factor for adjust the curve.

$$q_{\lambda} = \frac{2\pi c^2 h}{\lambda^5} \frac{1}{e^{ch/\lambda kT} - 1} \quad (\text{AC2})$$

where q_{λ} , T , λ , λ_{\max} , c , h , k are energy flux of light at a wavelength, temperature, wavelength, wavelength at a maximum radiation, speed of light, Planck's constant and Boltzman's constant, respectively. The result of estimation is shown in Fig. AC5.



Effective time (ms)	λ_{\max} (nm)	Temperature(K) From Eq. AC1	Temperature(K) From Eq. AC2	Max Intensity
4423	585	4929.915	4950	416
4558	577	4998.267	5020	531
4770	581	4963.855	4990	431
4848	580	4972.414	5000	483

Figure AC5 Applying Planck equation for estimating temperature from spectrum and theirs results

Table AC1 Temperature of arc plasma which was estimated form Eq. AC1 -AC2.

Spectra	λ_{max} (nm)	Temperature(K) From Eq. AC1	Temperature(K) From Eq. AC2	Max Intensity
Highest ↓ Lowest	577	4998.267	5020	531
	580	4972.414	5000	483
	581	4963.855	4990	431
	585	4929.915	4950	416
	588.324	4902.061		338
	590.032	4887.870		322
	590.374	4885.039		313
	594.809	4848.615		277
	616.538	4677.733		296
	624.975	4614.585		272

Group 2 estimate from normalized curve

Group 1 estimate directly from raw radiation spectrum

Estimate the arc temperature from the spectra when arc in water with N₂ gas injection at room temperature, the results of calculation are shown in Fig AC6.

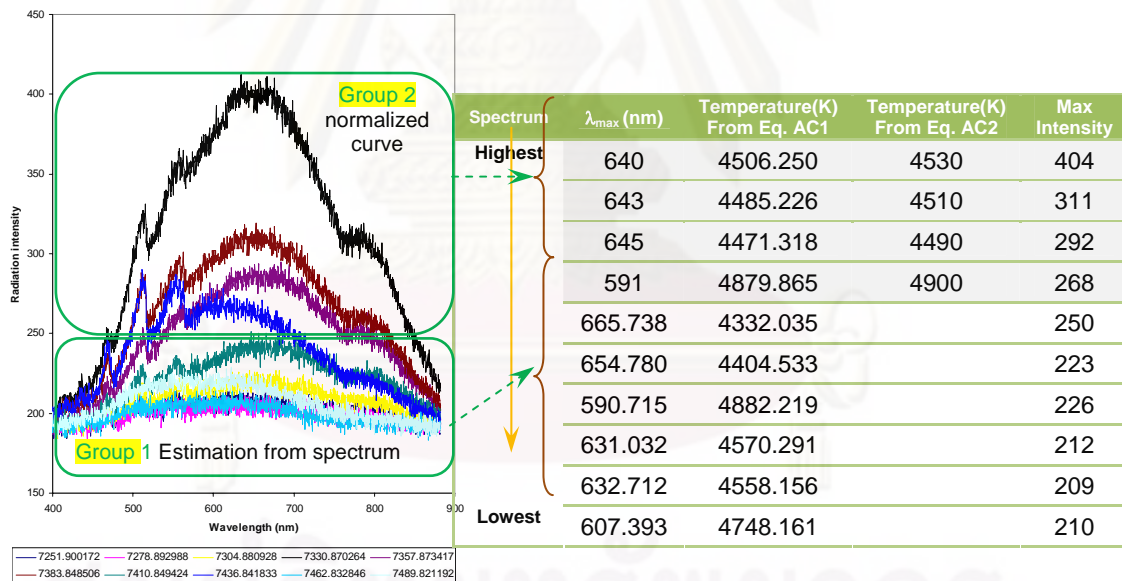


Figure AC6 Estimation of arc temperature when arc in water with N₂ injection at room temperature from the optical spectra.

Group 2 Show the spectra which fitting with SB-Planck law from highest to lowest spectrum

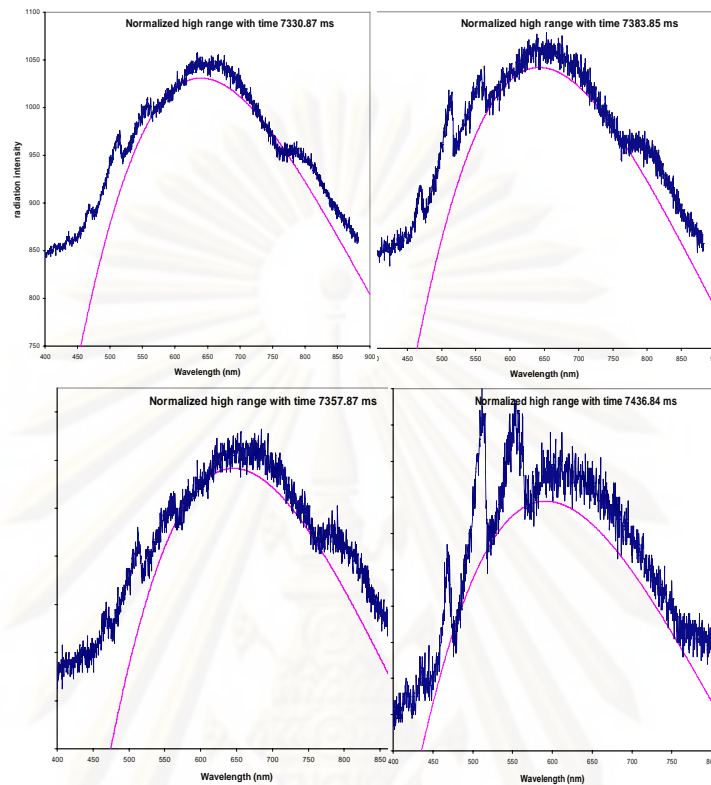


Figure AC7 Applying Planck equation for estimating temperature from spectra (arc in water with N₂ injection at room temp.)

Estimate the arc temperature from the spectra when arc in water with N₂ gas injection at high temperature (~ 80°C), the results are shown in Fig AC8.

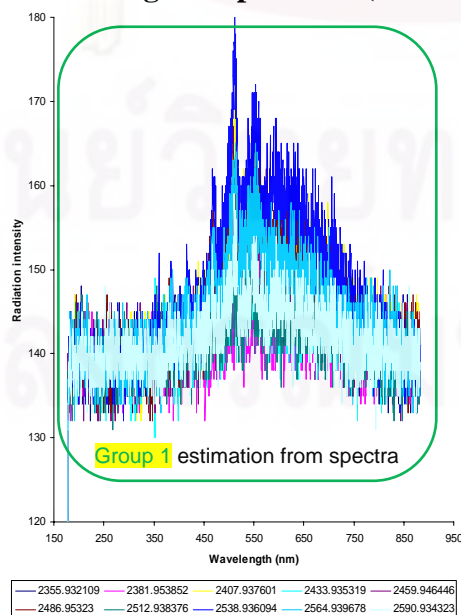


Figure AC8 Optical spectra of arc plasma from arc in water with N₂ gas injection at high temperature.

Table AC2 Temperature of arc plasma which was estimated from Eq. AC1 when arc in water with N₂ injection at **high temperature**

Sampling Time (ms)	λ_{\max} (nm)	Temperature(K) From Eq. AC1	Max Intensity
2355.93	553.926	5206.472	153
2381.95	554.272	5203.222	147
2407.93	556.002	5187.032	158
2433.93	552.541	5219.522	150
2459.95	551.848	5226.077	150
2486.95	554.618	5199.975	158
2512.94	554.964	5196.733	149
2538.94	552.541	5219.522	161
2564.94	553.926	5206.472	154
2590.93	556.348	5183.806	148

ศูนย์วิทยทรัพยากร
จุฬาลงกรณ์มหาวิทยาลัย

APPENDIX D

LIST OF PUBLICATIONS

Journal publication

Poonjarernsilp, C., Sano, N., Tamon, H., and Charinpanitkul, T. A model of reaction field in gas-injected arc-in-water method to synthesize single-walled carbon nanohorns: Influence of water temperature. Journal of Applied Physics, 106 (2009): 104315-1–104315-7.

International proceeding (Oral Presentation)

1. Poonjarernsilp, C., Sano, N., Charinpanitkul, T., and Tamon, H. One step synthesis of Pd/carbon nanocomposites by arc in water with N₂ gas injection. 6th Asian Aerosol Conference, p. 79, November, 2009, Bangkok, THAILAND.

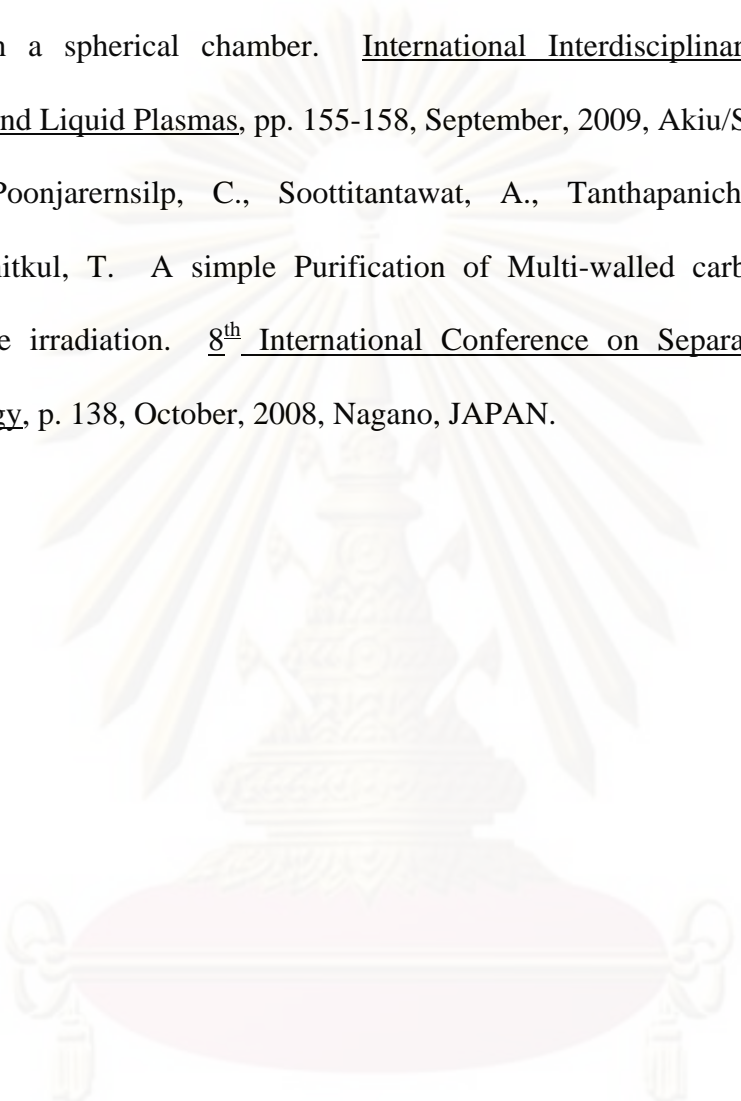
2. Poonjarernsilp, C., Sano, N., Tamon, H. Charinpanitkul, T., Soottitantawat, A., and Tanthapanichakoon, W. Effect of water temperature on synthesis of single-walled carbon nanohorn by arc discharge in water with nitrogen gas injection. 74th Chemical Engineering Conference Annual Meeting (2009), Yokohama, JAPAN.

3. Poonjarernsilp, C., Soottitantawat, A., Charinpanitkul, T., Sano, N., and Tamon, H. Frabrication of carbon nanoparticles by arc discharge in reduced pressure of air within a spherical reactor. Chemical Engineering Conference Kansai Meeting (2008), p.17, Himeji, JAPAN.

International proceeding (Poster Presentation)

1. Poonjarernsilp, C., Charinpanitkul, T., Soottitantawat, A., Sano, N., and Tamon, H. Synthesis of carbon nanoparticles by arc discharge under reduced pressure air within a spherical chamber. International Interdisciplinary-Symposium on Gaseous and Liquid Plasmas, pp. 155-158, September, 2009, Akiu/Sendai, JAPAN.

2. Poonjarernsilp, C., Soottitantawat, A., Tanthapanichakoon, W., and Charinpanitkul, T. A simple Purification of Multi-walled carbon nanotubes by microwave irradiation. 8th International Conference on Separation Science and Technology, p. 138, October, 2008, Nagano, JAPAN.



ศูนย์วิทยทรัพยากร
จุฬาลงกรณ์มหาวิทยาลัย

VITAE

Mrs. Chantamane Poonjarernsilp (Birth name: Chantamane Wangsajantanon) was born on October 1st, 1976 in Bangkok. She attended Wat Plubprachai for primary school and Satri Angthong for high school. In 1996, she received the college diploma in chemical technology (Petrochemical industry) and graduated Bachelor of Science (Industrial Chemistry) at Rajamangala Institute of Technology, Bangkok Technical campus in 1998, where she was on the honor roll for two years and challenged the scholarship for becoming a lecturer at Bangkok Technical campus (became to be Rajamangala University of Technology Krungthep in 2005). Following graduation, she has become a lecturer at Bangkok Technical campus since 1999. She was inspired to develop her career by studying in chemical engineering field. In 2004, she graduated in Master of Engineering (Chemical Engineering) at Chulalongkorn University. As part of her requirements for graduation, she wrote thesis entitled, "Development of an economical 20-liter dust explosibility standard tester". After that she continued to study in doctoral program in center of excellence in particle technology (CEPT). During this, she received the scholarship from Commission on Higher Education (CHE) of Thailand (strategic scholarships fellowships frontier research networks). By this financial support, she also did the research at Kyoto University for ten months with Associated Professor Noriaki Sano. She graduated doctoral degree of engineering in 2009 with doctoral thesis entitled "Synthesis of carbon nanohorns hybridized with Pd nanoparticles by gas-injected arc discharge technique". Until now, she is the lecturer of Department of Chemical Engineering, Faculty of Engineering, Rajamangala University of Technology Krungthep.